# Radar-Based Classification of Unmanned Aerial Vehicles (UAVs) Carrying Payloads

Thesis by:
Harinee Visvanathan Sethuraman

TUDelft

# Radar-Based Classification of Unmanned Aerial Vehicles (UAVs) Carrying Payloads


Thesis by:
Harinee Visvanathan Sethuraman


to obtain the degree of Master of Science in Electrical Engineering
at the Delft University of Technology,
to be defended publicly on Tuesday August 24, 2021 at 13:00 hrs.



| | | |
|---|---|---|
| Student number: | 5041392 | |
| Thesis committee: | Prof. Dr. Alexander Yarovoy, | TU Delft, Professor, Chairman, Research Group: MS3 |
| | Dr. Francesco Fioranelli, | TU Delft, Assistant Professor, Research Group: MS3 |
| | Dr. Raj Thilak Rajan, | TU Delft, Assistant Professor, Research Group: CAS |




An electronic version of this thesis is available at `http://repository.tudelft.nl/`.


TU Delft

# Preface

*“Never give up on a dream just because of the time it will take to accomplish it. The time will pass anyway.” –Earl Nightingale*

I always loved to associate myself with a field responsible for yesterday’s, today’s and tomorrow’s technological advancements, which ultimately fostered a dream in me to pursue my Masters in Electrical Engineering. The last two years have driven me beyond my comfort zone in ways I never imagined, and I am thankful for it. I’ve had my fair share of sleepless nights, but glancing back and realising how much I learnt throughout these trying times is really gratifying.

My thesis journey on ’Radar-Based Classification of Unmanned Aerial Vehicles (UAVs) Carrying Payloads’ was conducted in the Microwave Sensing, Signals and Systems (MS3) research group at TU Delft. During the course of the thesis, I received tremendous support and encouragement from many, and I would like to take this opportunity to express my gratitude to these amazing people.

First and foremost, I would like to thank **Dr. Francesco Fioranelli**, my primary thesis supervisor who introduced me to this wonderful thesis topic. His genuine commitment and guidance from the beginning enabled me to gain knowledge of the concepts. My extended discussions with him, and his valuable suggestions by engaging me in new ideas contributed greatly to streamline the thesis. My profound gratitude to **Prof. Dr. Alexander Yarovoy** for giving me the opportunity to be a part of this dynamic research group and I am fortunate and grateful to have had the chance to work under his guidance. I thank him for his scholarly insights that help all his students towards academic excellence. I would like to extend my thanks and appreciation to **Dr. Raj Thilak Rajan** for his kind gesture in being a part of the thesis committee.

I am endlessly indebted to my family for their unfathomable support, unwavering care and motivation throughout my studies. Thank you Appa, Amma and my sister Pavithra for your unconditional love and for always being there for me in all my pursuits. A big thank you to all my friends in Netherlands and India for the constant encouragement and delightful memories.

Last but not the least, I thank TU Delft for providing me with a brilliant platform for my Masters and I will be very proud to be Alumni of this great academic community.

*Harinee Visvanathan Sethuraman*
*Delft, August 2021*

# Abstract

Unmanned Aerial Vehicles (UAVs), commonly referred to as drones have gained increasing popularity with current technological breakthroughs. Recent reports indicate the number of registered drones in the United States have crossed 850,000 and is expected to increase multi-fold over the coming years. The widespread applications of drones include agriculture, transportation, mining, media, entertainment, etc. While drones are used for many benevolent purposes, there are also multiple real-life incidents, where drones have caused serious mishaps. Radars with high resolution are increasingly used for drone detection and classification, thanks to their long-range, all-weather monitoring capabilities. Several techniques for binary classification of drone vs no drone, drone vs birds, and different models of drones, have been proposed based on the relevant features extracted from the micro-Doppler signatures or from tracks' information. Recently, research focusing on the problem of classifying drone(s) carrying payloads has garnered considerable attention.

In this thesis, the ability of a fully polarimetric radar and a single polarimetric radar to discriminate between payloads carried by UAVs is demonstrated. A novel approach has been employed in the feature extraction algorithm, where features from individual and combined polarimetric channels are extracted for classification. Decision and ensemble fusions on the respective extracted features proved to enhance the classification performance. The robustness of the algorithm is validated on two experimental radar datasets acquired in the scenarios where the UAVs carrying payloads of different weights are hovering, flying back and forth, and flying along rectangular waypoints. Initial results for the fusion techniques provide approximately 95%-99% classification accuracy for the polarimetric and statistical features.

*Keywords — polarimetry, radar, UAVs, payloads, feature extraction, classification.*

# Contents

# List of Figures

# List of Tables

# Nomenclature

| | |
|---|---|
| BW | Bandwidth |
| CFAR | Constant False Alarm Rate |
| CM | Confusion Matrix |
| CNN | Convolutional Neural Network |
| CPI | Coherent Processing Interval |
| CV | Cross-Validation |
| CVD | Cadence Velocity Diagram |
| CW | Continuous Wave |
| DFT | Discrete Fourier Transform |
| DJI | Da-Jing Innovations |
| DT | Decision Tree |
| EM | Electromagnetic |
| FAA | Federal Aviation Administration |
| FMCW | Frequency Modulated Continuous Wave |
| FN | False Negative |
| FP | False Positive |
| GAN | Generative Adversarial Network |
| HERM | Helicopter Rotational Motion |
| HH | Horizontal-Horizontal |
| HV | Horizontal-Vertical |
| IDFT | Inverse Discrete Fourier Transform |
| JEM | Jet Engine Modulation |
| LDA | Linear Discriminant Analysis |
| LDA | Quadratic Discriminant Analysis |
| LOS | Line of Sight |

| | |
|---|---|
| NB | Naive Bayes |
| PCA | Principal Component Analysis |
| PDF | Probability Density Function |
| PRF | Pulse Repetition Frequency |
| RBF | Radial Basis Function |
| RCS | Radar Cross Section |
| RTI | Range Time Intensity |
| SBE | Sequential Backward Elimination |
| SD | Standard Deviation |
| SFS | Sequential Forward Selection |
| SK | Spectral Kurtosis |
| SNR | Signal to Noise ratio |
| STFT | Short-Time Fourier Transform |
| SVD | Singular Value Decomposition |
| SVM | Support Vector Machine |
| TN | True Negative |
| TP | True Positive |
| UAV | Unmanned Aerial Vehicle |
| UCL | University College London |
| USRP | Universal Software Radio Peripheral |
| VH | Vertical-Horizontal |
| VV | Vertical-Vertical |

# Chapter 1

# Introduction and Overview

*In this chapter, the background and motivation to take up the research on the thesis 'Radar-Based Classification of Unmanned Aerial Vehicles (UAVs) Carrying Payloads' is discussed in detail. The salient aspects of research questions, contributions and novelties are also covered, with a brief insight into the following chapters.*

## 1.1 Background and Motivation

With recent advancements in technology, the number of Unmanned Aerial Vehicles (UAVs), commonly referred to as drones, have detonated in ubiquity and is accessible to everyone. The UAVs have grown increasingly important in the operations of many business and government entities, penetrating through the sectors where some industries were inert or trailing behind. Drones, either commanded by a remote or via a smartphone app, have the ability to reach even the most inaccessible locations with little to no people and with the least amount of effort, time, and energy. This is one of the primary reasons for their widespread adoption, particularly in the four sectors of military, commercial, personal, and future technologies. The records from Federal Aviation Administration (FAA) indicate the number of registered drones alone to be approximately 870 thousand in the United States of America (USA), as of August 3, 2021, presented in Table 1.1. The UAVs, which were initially developed for military use, have seen swift progress and have made their way into consumer appliances. While military drones are still popular, their use has moved far beyond tactical purposes.

Drones, over the recent years, are used in multiple scenarios, ranging from defence purposes to commercial use, like photography, delivery of goods and medicines, mining etc. The initial commercial application of UAVs can be dated back to the early 1980s for the purpose of spraying pesticides over rice fields, where remotely piloted helicopters rendered as a promising route of augmenting manned helicopters. In the domain of transportation, drones have become an integral component in e-commerce and many industries like Amazon and Domino's have launched the testing phase in the logistics of their goods. An enhanced customer satisfaction would be established by the ease of shipment of goods to the client's doorstep and drones would ensure speedy service to the specific pre-configured location without involving much human intervention. The good or cargo carried by drone is termed as 'payload', which is the weight borne by the UAV exclusive of what is required for its operation [1].

The categories of drone utilization can be broadly segregated into genuine and malicious activities, as shown in Figure 1.1. While drones are used in many benevolent applications, there are also multiple real-life incidents, where drones have caused serious mishaps, ranging from posing as a public nuisance during official meetings, football matches, to interfering with aircrafts and helicopters, to dropping grenades and explosives, resulting in catastrophic events [2]. This brings to the constant fear of drones (carrying illegal components/ goods). The outstanding propensity of a large number of vulnerabilities by exploiting the easily accessible resources is a major concern and even by enforcing laws, the authorities have a hard time combating with the illicit use of drones.

| Registered Drones | | | Certified Remote Pilots |
|---|---|---|---|
| Commercia Use | Recreational Use | Registered on paper | |
| 350,608 | 515,887 | 3,499 | 239,562 |
| Total : 869,994 | | | |

Table 1.1: Number of Unmanned Aerial Vehicles registered in the United States, as of August 3, 2021 [3]

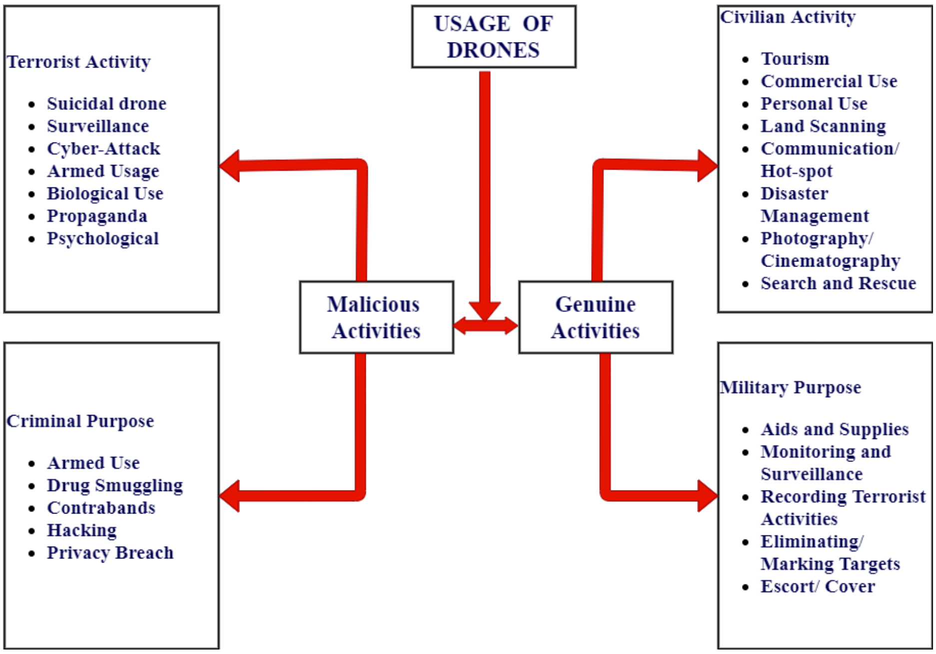


Figure 1.1: Usage of Unmanned Aerial Vehicles (UAVs) for multiple purposes, inspired from [4]

The first concern that arises is selecting an optimum sensor that can monitor the activities of drones throughout 24x7. High-resolution radars are specifically designed for drone detection, with their ability to operate in all weather circumstances and the potential to measure range and velocity simultaneously, radars are used as ideal sensors for the detection of drones in contrast to other sensors, such as LIDAR [5].

One of the issues to be tackled is the dependence on Radar Cross Section (RCS), since the structure of the drone can be too small to be detected by the radar. Extensive studies have successfully provided a more reliable parameter that negates the need for RCS. These attributes delve into the individual components of the drone, such as the rotor blades, fuselage, etc., which can eventually be reflected on the micro-Doppler signature to closely monitor the drone activities. This can be used as a basis to detect if the drone is present or not. The next concern after the identification of drones is distinguishing them from other similar targets. There are multiple targets recognized by the radar, such as birds or other drones. Based on the driving systems, UAVs can be classified as multi-rotors, hybrid/ fixed-wing and tilt-wing drones [1]. The micro-Doppler signatures aid in segregating drones from birds using the rotation patterns and velocity of the rotors and wings. For the scenario of differentiating between drones, the number of blades and velocity play a major role. The micro-Doppler signatures vary distinctly for even and odd numbers of blades in drones, and this can be used as one of the attributes to classify the drone models. Thus, various feature extraction and machine learning algorithms are developed to achieve an ideal classification performance.

Moving on to the next concern is the scenario when the drone is carrying a payload. As stated already, the structure of the drone is small, and it would be a challenging task to detect the payload. Multiple techniques have been considered for the detection and classification of drones using radars, however, the current research that is going on in the field of classification of drones is to identify whether the drone is carrying payloads and develop algorithms to detect and classify them [6]. The hurdle is to provide suitable feature extraction methodologies to generate significant features, which can be used by classifiers for obtaining optimized performance. Thus, this thesis provides unique feature extraction algorithms and fusion techniques (after classification) to distinctly classify the weights of classes of payloads that are carried by different models of drones.

## 1.2 Research Goals, Novelties and Contributions

The myriad of incidents and possible threats by drones carrying payloads causing catastrophes raise serious apprehensions about the dire need to monitor them. There have been studies towards the detection of drones, with an emphasis on the integral empirical and physical characteristics of drones [7]. Following this, [8]-[9] delve into the micro-Doppler aspects and methods for optimally identifying drones from birds or different types of drones. However, the niche area revolves around the domain of modelling and classification of the signatures of drones that are carrying payloads and the effective techniques to achieve good classification performance. The number of research in this field is relatively less and only a handful of open literature is available, this paves a way to develop algorithms for optimum classification of drones with payloads [10], [11], [12]. A detailed analysis of the different methodologies will be explained in Chapter 2.

In this thesis, the main objectives that will be covered with an effort to fill some of the research gaps are listed as follows.

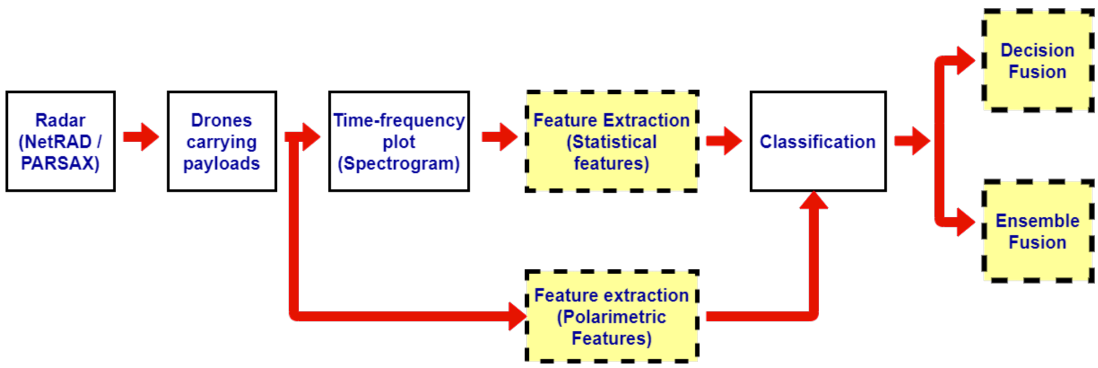


Figure 1.2: Flow chart of Research methodology, with main contribution blocks highlighted in yellow

- The problem of classification of Unmanned Aerial Vehicles (UAVs) that are carrying payloads is approached by generating polarimetric features from Range-Time plots and statistical features from micro-Doppler signatures. These features are given as input to the supervised machine learning classifiers.
- Algorithms using decision fusion for the statistical features and ensemble fusion for the polarimetric features, and their effects on the classification performances are investigated.
- Initial results are validated based on the two sets of experimental data collected using (a) a single polarimetric NetRAD radar; (b) a fully polarimetric PARSAX radar, for different models and tra-

jectories of drones, and the various payload weights. This also helps to infer if the algorithms are robust and agnostic to the type of radars, the model of drones, and the weights of payloads.

The block diagram in Figure 1.2 illustrates the research pipeline. The major contributions involve the extraction of two sets of features, namely, the statistical and polarimetric features as input to the classifiers. The novel approach on enhancing the classification performance is also exhibited through the decision and ensemble fusion techniques. These unique key strategies are indicated in the yellow blocks in Figure 1.2

Furthermore, the conference paper, titled ***'Classification of Unmanned Aerial Vehicles (UAVs) Carrying Payloads with Polarimetric Radar'*** with results arising from this thesis work has been submitted to the European Microwave Week 2021, Excel London Exhibition and Conference Centre, UK, that is to be held in February 2022.

## 1.3 Literature review in brief

The analysis of works of literature relevant to the research can be divided into the following types:

- *Type 1:* Investigation about the parameters for detection of drones with the help of radar and the significant parameters identifiable in drones (Jet Engine Modulation (JEM), Helicopter Rotational Motion (HERM) lines). The preliminary binary classification of drone vs no drone is reviewed.
- *Type 2:* An expansion to Type 1 deals with a combination of binary and multiclass classification problems. The targets are birds and different types of drones. The analysis involves generating the optimum parameters for classification from the micro-Doppler signatures.
- *Type 3:* This category deals with the prime focus of the thesis, which is the classification of payloads. Various studies have been reviewed which use spectrogram, cepstrogram, etc. for monitoring the activities of drones carrying payloads.

A detailed explanation of the mentioned categories is delineated in Chapter 2.

## 1.4 Structure of the Thesis

The thesis report is organized in the following way:

- **Chapter 1:** Introduction about the main objective for carrying out this research, the goals of the thesis, the novel contributions and the organization of the thesis are covered.
- **Chapter 2:** The evolution of the state of the art detection and classification of algorithms for drones, birds, and drones carrying payloads from various works of literature are reviewed.
- **Chapter 3:** Mathematical modelling about the Radar Cross Section (RCS) of drones and payloads by the method of approximation are calculated. Analyses on the activities of drones for different scenarios are assessed from their micro-Doppler signatures.
- **Chapter 4:** The experimental setups for the two sets of data from NetRAD and PARSAX, the data pre-processing and its Range Time Intensity plots (RTI) are illustrated.
- **Chapter 5:** The research methodology and techniques are presented, including Short Time Fourier Transform (STFT), feature extraction, classification and fusion. Extraction of significant statistical features from the spectrogram is performed via Singular Value Decomposition (SVD), Centroid and Bandwidth. The polarimetric features for the data from PARSAX radar are explored. The classification algorithms and different types of fusion techniques are evaluated.

- **Chapter 6:** The results and observations from the fusion techniques and parametric analyses are examined. The different parameters that are considered are variations in (a) dwell time, (b) spectrogram window duration, and (c) additional noise to vary Signal to Noise Ratio (SNR).
- **Chapter 7:** Major conclusions from the thesis, limitations and the open questions for future work are discussed.

## 1.5 Conclusion

In this chapter, the following aspects of the thesis have been highlighted:

- The main motivation and background of the thesis are covered. It is evident from the realistic disastrous incidents why drones are a serious threat, and the need to monitor them.
- The research objectives and the major contributions and novelties, including the conference paper are discussed.
- A brief review of the categories of literature on which the thesis is extended is mentioned, along with an overview of the upcoming chapters.

# Chapter 2

# Literature Review

*In this chapter, an overview of the lists of literature are reviewed. Radars with high resolution are increasingly used for drone detection and classification, thanks to their long-range, all-weather monitoring capabilities. Several techniques for binary classification of drone vs no drone, drone vs birds, and different models of drones have been proposed based on relevant features extracted from the micro-Doppler signatures or from tracks' information [5].*

*The collection of the literature papers are broadly categorized into three categories as stated previously in Chapter 1, based on algorithms used and the type of classification.*

- *Type 1: Investigation about the parameters for detection of drones with the help of radar, and the significant parameters in the drones (Jet Engine Modulation (JEM), Helicopter Rotational Motion (HERM) lines). The preliminary binary classification of drone vs no drone is also reviewed.*
- *Type 2: An extension to the Type 1 deals with a combination of binary and multiclass classification problems. The targets are birds and different types of drones. The analysis involves generating the optimum parameters for classification from the micro-Doppler signatures.*
- *Type 3: This category deals with the prime focus of the thesis, which is the classification of payloads. Although the fact that the literature papers in this area are relatively limited, various studies have been examined which use spectrogram, cepstrogram, etc. for monitoring the activities of drones carrying payloads.*

## 2.1 Type 1: Drone Detection parameters and Binary classification

The main motivation for drone detection is exemplified in the paper [13], which reviews the prevailing literary works on the key suitable techniques proposed in the various stages of the identification process, i.e., detection of potential drone activities, evaluation of targets and classification of drones. The major focal point is given to detection using radar sensors and optimum methods for detection of the presence of drones and its classification (called binary classification, where the classes are drone and no drone). The study states that the most viable method is to achieve a reliable performance of the surveilled region and to take control of the benefits of various innovations whilst dealing with their particular drawbacks via modern monitoring systems consisting of a channel of spatially dispersed sensors.

As much as radar is preferred for the detection of drones, machine learning is used prevalently for the classification of targets. The article [14] addresses an extensive overview of the existing drone detection research and classification employing multiple strategies of machine learning. The innovations broached involves radar, Radio-Frequency (RF), visual and acoustic sensing systems. A significant aspect of drones that can be used for the intention of detection and mapping is the RF signal. That being said, when the drone operates in a moderately or completely automatic environment, RF-based technologies stall. The broad sense evidence highlights that the classification of drones predicated on machine learning seems challenging with several other successful direct contributions.

The initial research of drone detection started with the binary scenario to determine if the drone is present or not. The main objective of [7] is employing a (32 x 8) element L-band receiver array for detection of micro-drones, specifically hexacopters. The Holographic Radar (HR) is used for the creation of a two-dimensional multi-beam. The feature extraction is based on features related to flight profile, such as maximum height, acceleration, track, jerk, in order to discriminate the presence of hexacopters that have been derived from a holographic L-band radar data. These features have been identified over a series of trial and error methods. Finally, a decision tree was is to evaluate the performance metrics and the probability of detection of 88% is achieved.

With the evolution of research in the domain of drone detection, extensive studies have been carried out to represent drone visualization on time-frequency domain plots. The paper [15], deals with the cepstrum mechanism, which is seen to ascertain the rotation rate, as an alternate method is required for detection and classification of drones when the PRF (Pulse Repetition Frequency) is inadequate, with the fact that the targets can be discriminated based on the periodicity. In this study, a new algorithm of log harmonic summation is proposed which makes use of a long interval of STFT (Short-Time Fourier Transform) window to estimate the rotation rate of the rotor by determining the Helicopter Rotation Modulation (HERM) lines' frequency. It is analyzed that even with a feeble micro-Doppler signature, the above-mentioned technique still holds good and the reliability of the model based on the predictions is also found to be closely equivalent to the ground truth.

Similarly, in [16], the study provided a spectral evaluation of Doppler that is employed to the helicopters and quadcopters. The primary objective is to comprehend the transformation of input of radar and shape of target between micro-Doppler and (Jet Engine Modulation) JEM/HERM regimes while imposing the Doppler processing. The importance of rapidly changing signature variations and duration of STFT is demonstrated as the outcome of the research. It is also concluded that the target identification proficiency can be optimized by taking the above parameters into consideration during evaluation.

## 2.2 Type 2: Classification of Drones versus other targets

Following drone detection using radar, the review is extended to the detection of drones VS birds, as well as detection of multiple types of drones. Moreover, the different algorithms using the micro-Doppler signatures are covered.

In the classification of drones and birds, [8] articulates the challenges in distinguishing birds from UAVs, where a sophisticated long-range defence radar is employed. The core principle of this research is to assess the polarimetric characteristics since they convey meaningful data about small objects. As an extension to this study, the polarimetric features are used as a baseline for the classification of payloads in this thesis research, which is discussed in Chapter 5.

From the paper [17], it is presented about the possibility to retrieve essential features via spectrograms and cepstrograms for the LSS ('Low (altitude), Small (RCS) and Slow (speed)') characteristics to be detected conceptually and instinctively for rotating and moving targets. For this purpose, a CW (Continuous Wave) radar is used. The originally broad literature is narrowed down to discuss features from birds and micro-drones for classification. It is concluded that the long integration and short integration of the spectrogram indicated the spectral width, body velocity; and blade flashes, individual rotor signals respectively. On the other hand, the rotors and periodicity can be observed from the cepstrogram.

For the classification of the scenario of multiple drones, the study [18] presents a multi drone thin-wire electromagnetic framework which proficiently emits drone micro-Doppler patterns as an interface of radar constraints as well as rotor characteristics. It is seen that in long Doppler coherent processing interval (CPI) parameters, this research discusses radar recognition of multi-propeller drones through micro-Doppler linear spectral profiles. It fixates on exploring the relationship on the micro-Doppler spectrogram of the structural architecture and rotation factors, for which it considers blade such as blade number, blade layout, drone model configuration and rotor orientation. Effective attributes for drone identification have been formulated relying on the modelled frequency peak amplitudes as well as positions in the micro-Doppler linear range. For this with the computational quadcopter and hexa-copter information, their performance is verified employing effective classifier Support Vector Machine (SVM). The classification performance for the binary class problem is obtained as 99% and 93% for the scenarios of hovering and manoeuvring at an altitude.

The literature [9] throws light on the background of cognitive radar, where the study explores the capacity of deep learning algorithms for classifying micro-drones employing micro-Doppler spectrograms. A comparison of the performance of Soft-max and GANomaly, which are the two deep learning algorithms are evaluated for unknown targets. If a micro-Doppler spectrogram from a target class that is not depicted in the training set is analyzed by a cognitive radar, an abnormal detection algorithm would provide cognitive radar configuration with a prompt to gather spectrograms of micro-Dopplers from such an unknown target. It is concluded that, in addition to enhancing the innovation, detailed knowledge of the principle underlying deep neural networks, possibly facilitated by the association with compressive sensing and sparse signal portrayals, would accelerate the perception of many sophisticated applications.

## 2.3 Type 3: Classification of Drones Carrying Payloads

The most important objective in the domain of drone detection is the case where the drone is carrying a payload. From [1], it is transparent that it is a burning problem to identify if the drones are carrying payloads and then classify them. Thus, relating it to the literature [10], it states that the micro-Doppler pattern provides optimum information regarding the drone if it is carrying a payload or not. The experimental study that is carried out in the X-band clarifies that RCS might not be an optimum parameter, however, it plays an important role in revealing if the payload is dropped by the drone. This information is also backed up by the tip velocity and rotor motion.

In the paper [11], with the intent of UAV payload classification, a novel micro-Doppler feature extraction technique largely dependent on the utilization of 'spectral kurtosis' (SK) is proposed, where the measurement is captured using NetRAD. The notion of implementing and using this fourth-order statistical method for the classification of signals generated from objects distinguished by rotating segments as drones stems from the underlying attributes and applications of spectral kurtosis in the surveillance of vibrating and rotating machines. The spectral kurtosis is determined on both the narrowband and wideband spectrograms accumulated and is then fed to a k-nearest neighbour classifier, before which Principal Component Analysis (PCA) is performed for reduction of dimensionality. The classification accuracy of 82%-97% is attained.

The same dataset is used in [19], where the authors have investigated the methods to track and distinguish the scenarios of the micro-drones flying and hovering with payloads of various weights. For this purpose, multistatic pulsed radar NetRAD is made use of. The salient statistical features derived by feature extraction involved the application of Singular Value Decomposition (SVD), Centroid and Bandwidth of the micro-Doppler signature. Classification accuracy of 95% and 97% is obtained for the features extracted via Centroid and SVD respectively using three suitable classifiers a) Discriminant analysis, b) Naïve Bayes classifier, c) Random Forest theory.

Expanding the investigation to multiple time-frequency domains, [6], also used the same NetRAD dataset for the classification of drones carrying payloads. The multistatic pulsed radar NetRAD is used to carry out the experiment and the operational situations that have been investigated are that of the flying of drone and of the hovering of drone. The data collected are classified based on deep learning algorithms and multiple Doppler signatures, that is, CVD (Cadence Velocity Diagram), cepstrogram and spectrogram, which are the representation in the multi-time frequency domain were considered. In order to detect if the drone is hovering or flying, the obtained data is subjected to Hilbert transform, matched filtering and the spectrogram is obtained when STFT (Short-Time Fourier Transform) is imposed over the range cells. Similarly, STFT and later applying IDFT (Inverse Discrete Fourier Transform) taking into account a suitable time window generated cepstrogram. Lastly, Cadence Velocity Diagram also is created by performing DFT (Discrete Fourier Transform) over the Doppler frequency. Then for the part of feature extraction and classification, a convolutional neural network (CNN) is adopted to identify the key characteristics of the drone with/ without payload. From the analysis of the results, higher total accuracy of 96.6% is obtained for the scenario of drone flying, as compared to the total accuracy of 95.1% in the case of drone hovering.

Similar research on drone detection and classification using a different dataset, wherein [20], FMCW (Frequency Modulated Continuous Wave) Radar is used, and the Parrot Bebop 2 quadcopter carried AA batteries of 23g on each of its arms, thus carrying an overall of 92g, keeping in mind the aerodynamics of the drone. Similarly, as seen in the above papers, the spectrogram of the quadcopter is attained by applying Short Time Fourier Transform (STFT). From the 12 features that were retrieved based on the spectrograms, 3 classifiers, namely, Support Vector Machine (SVM) with Radial Basis Function (RBF) and Quadratic kernel, and a Diagonal-Quadratic Bayesian classifier were applied for different dwell times. It is analyzed that the optimum accuracy (even for a shorter dwell time) is achieved in the case of SVM. An overall classification accuracy yielded 80% to 90%.

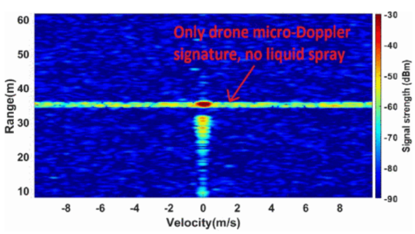


(a) Range Doppler plots without liquid spray

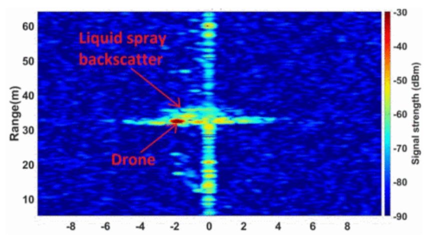


(b) Range Doppler plots bore is seen at the drone

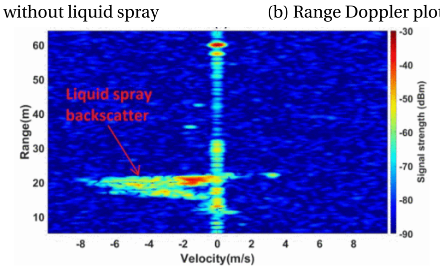


(c) Range Doppler plots when bore is observed at the spray below the drone

Figure 2.1: Range-Doppler plots for the experimental results from a drone used in spraying of crops in [12]

An interesting research in [12] assessed upon these conspicuous radar signatures of liquid spraying drones, equivalent, for instance, to a drone carrying weaponry as seen in Figure 2.1. For the premise of liquid droplet radar backscatter simulation and for observational data surveillance, a widely accessible crop-spraying drone likewise is utilized. Rayleigh approximation is used to model the parameters of the droplet based on Radar Cross Section (RCS) and Signal to Noise Ratio (SNR). As the model predicted, the justification for selecting high-frequency radar systems is that these tiny fluid particles are intended to be very invisible to lower-frequency radar signals. The findings reinforce the existing proposition that the short wavelength of the millimetre-wave radar is feasible for the identification of fluid material dispensed from a drone which could be used as an interface of range and radar constraints to estimate tracking via a classic Rayleigh scattering prototype. It is analyzed that 94 GHz radar is able to detect the spray at approximately 150 metres. The characteristic from the microscopic spherical droplets is anticipated to be relatively tolerant to polarization, while in HH polarization the micro-Doppler from drone rotors happens to be significantly greater. Also, it is seen that lower frequency radars have higher ranges of detection and classification, although the relatively microscopic RCS spray might not be observed.

## 2.4 Conclusion

In this chapter, the state of the art techniques for radar-based detection and classification of UAVs from the recent literature papers have been discussed. A summary of the methodologies is tabulated in Table 2.1.

- The research methodologies are validated on real experimental data from NetRAD and PARSAX radars in Chapters 4 and 5, in order to create robust algorithms suitable in realistic situations.
- The first colour in the Table 2.1 represents Type 1 which describes the parameters required to detect if the drone is present or not.
- Following this, the second colour indicates Type 2, which involves distinguishing drones from birds and differentiating between drone models.
- Finally, the third colour denotes Type 3, the prime focus of this thesis, which deals with drones that are carrying payloads.
- The main literature gap is the dearth of research in Type 3. Many studies have concentrated on the detection of the presence of drones and devised classification algorithms for differentiating drones from birds and other targets. These researches focus on the micro-Doppler aspects and the physical attributes of drone (Type 1 and Type 2).
- There are currently only a few investigations (at least in open literature) in the category of drones carrying payloads. This thesis aims to develop techniques to generate features from the micro-Doppler signatures of drones with payloads, such that they result in ideal discrimination among the weights of the payloads. The results are optimized by novel fusion algorithms.

| Paper | Radar | Scenario | Features | Classifier | Accuracy |
|---|---|---|---|---|---|
| [7] | Holographic Radar (L-Band) | Hexacopter Drone VS No Drone | Maximum Height, Acceleration, jolt | Decision Tree | Detection of 88% |
| [21] | GAMMA-2 passive radar system | Parrot AR drone and Amos X4 drone | Doppler signature | NA | NA |
| [22] | USRP1 passive radar system | Vario XLC Compact helicopter and Align M480L quadcopter | Micro-Doppler signature | NA | NA |
| [8] | BirdRad | Birds VS Drones (DJI Phantom 2, 3D Solo) | 9 Polarimetric Feaures | Nearest Neighbour | 100% |
| [17] | CW Radar | Drone VS Drone (RC Helicopter, RC Quadcopter) | Cepstrogram, Spectrogram (symmetry, periodicity), Spectrum width | NA | NA |
| [18] | PARSAX FMCW Radar | Drone VS Drone (DJI Drones) | Spectrogram (blade parameters | Support Vector Machine (SVM) | 99% for hovering and 93% for maneuvering |
| [9] | CW Radar | Multiple drones (Robbe Air Trainer 140, Sky Walker) | Denoising Spectrogram using adversarial auto-encoder | Multiple Deep Neural Networks | 90%-97% |
| [12] | CW Radar and FMCW Radar | DJI S900, Joyance JT5L-404, heavy/dynamic payload | Doppler spread weight, strength, HERM line spacing, fluctuation | Neural Network | 72% (2-class and 5-class problems) |
| [10] | CW Radar and FMCW Radar | Drones carrying 3D hand and mortar grenades | Micro-Doppler signature | NA | NA |
| [11] | NetRAD | DJI Phantom Vision 2+, carrying 0g to 500g payload | Spectral Kurtosis and PCA (for dimensionality reduction) | K-Nearest Neighbour | 82%-97% |
| [6] | NetRAD | DJI Phantom Vision 2+, carrying g to 500g payload | CVD (Cadence Velocity Diagram), cepstrogram and spectrogram | Convolutional Neural Network | 95% for hovering and 96% for flying |

Table 2.1: Comparison of Feature extraction and Classification techniques as seen in the literature studies

# Chapter 3

# Mathematical Modelling

*In this chapter, the mathematical modelling of the Radar Cross Section (RCS) is performed. The objective is to weigh the significance of RCS as a parameter for the detection and classification of drones and the payloads attached to them. The simplest model of a drone and its payload are considered and the RCS is calculated based on the method of approximation. The calculations are based on the assumption that the geometry of the drone and payload are spherical and the composition of the material is a metal (e.g. Aluminium). The realistic drone models and their payload dimensions (for a spherical geometry) are taken for specific types of drones from the DJI website. The RCS of drones and payloads are evaluated for further analysis, concluding that RCS may not be the best discriminative feature to identify drones carrying payloads.*

*Finally, the effect of payload on drone and its micro-Doppler information is depicted using a spectrogram. The scenarios from literature studies [10] and [23] are considered for comprehension. The variations in the drone activities are observed evidently via the time-frequency plots.*

## 3.1 RCS of simple models of payloads

The Radar Cross Section (RCS) of a drone that is carrying a payload is modelled to analyze their characteristics in the normal scenario, where the drone is static. Later, the specific scenarios where the drone carrying a payload is flying/hovering are discussed in the further chapters, and a comparison of the variations based on the different scenarios is delineated.

By analyzing the RCS, it is possible to comprehend a rough estimate if the size of the payload causes a change in the power, and approximately how big the payload should be to be detected by the radar. The general formula for the RCS is defined as [24]:

$$\sigma = \lim_{R\to\infty} 4\pi R^2 \left| \frac{E^{scat}}{E^{inc}} \right|^2 \tag{3.1}$$

where $E^{scat}$ and $E^{inc}$ denote the scattered and incident electric fields at the target.

A relation can be drawn from the Radar Range Equation (RRE), which correlates the Signal to Noise Ratio (SNR) and the Radar Cross Section (RCS). Since the performance of the radar can be determined using the SNR, it is expressed as:

$$SNR = \frac{P_t G_t G_r \lambda^2 \sigma}{(4\pi)^3 R^4 k T_o F B} \quad ; where \tag{3.2}$$

$P_t$: Peak transmitted power (W)

$G_t$: Transmit antenna gain
$G_r$: Receiver antenna gain
$\lambda$: Wavelength of the carrier (m)
$\sigma$: Target's mean Radar Cross Section ($m^2$)
$R$: Radar to target range (m)
$k$: Boltzmann's constant (1.38 X $10^{-23} J/K$)
$T_o$: Effective noise temperature at receiver
$F$: Noise figure
$B$: Bandwidth at receiver

From the equation 3.2, as RCS is dependent on the shape (and the material) of the target, the SNR equation is transformed into equation for RCS $\sigma$ as:

$$\sigma = \frac{SNR(4\pi)^3 R^4 k T_o F B}{P_t G_t G_r \lambda^2} \tag{3.3}$$

In reality, the payloads that are carried by the drones are of variety of shapes. The shapes that are considered here for the payloads are flat plate, sphere, triangular trihedral, rectangular trihedral, and dihedral. The RCS of these basic shapes with dimensions 'a' and 'b' are as given in 3.1

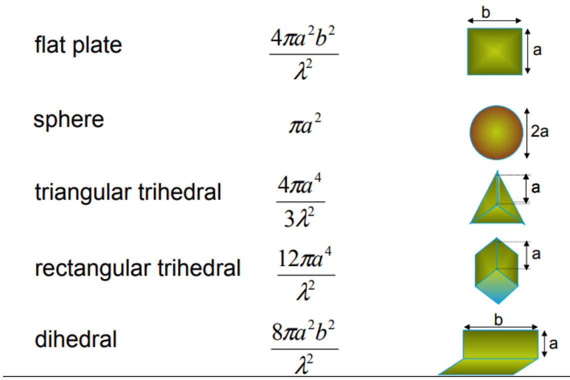


Figure 3.1: Radar Cross section of common shapes at high frequency [24]

For the common shapes and for the scenario where the targets are static, the azimuth and elevation angles are disregarded here, and the Radar Cross Sections of these basic shapes at high frequencies are formulated as follows.

- The SNR of a flat plate is:

$$SNR_{flatplate} = \frac{P_t G_t G_r \lambda^2 a^2 b^2}{(4\pi)^3 R^4 k T_o F B} = \frac{P_t G_t G_r a^2 b^2}{16\pi^2 R^4 k T_o F B} \tag{3.4}$$

- The SNR of a sphere is:

$$SNR_{sphere} = \frac{P_t G_t G_r \lambda^2 a^2 \pi}{(4\pi)^3 R^4 k T_o F B} = \frac{P_t G_t G_r \lambda^2 a^2}{64\pi^2 R^4 k T_o F B} \tag{3.5}$$

- The SNR of a triangular trihedral is:

$$SNR_{triangulartrihedral} = \frac{P_t G_t G_r \lambda^2 4\pi a^4}{(4\pi)^3 R^4 k T_o F B (3\lambda)^2} = \frac{P_t G_t G_r a^4}{48\pi^2 R^4 k T_o F B} \tag{3.6}$$

- The SNR of a rectangular trihedral is:

$$SNR_{rectangulartrihedral} = \frac{P_t G_t G_r \lambda^2 12\pi a^4}{(4\pi)^3 R^4 k T_o F B (\lambda)^2} = \frac{3 P_t G_t G_r a^4}{16\pi^2 R^4 k T_o F B} \tag{3.7}$$

- The SNR of a dihedral is:

$$SNR_{dihedral} = \frac{P_t G_t G_r \lambda^2 8\pi a^2 b^2}{(4\pi)^3 R^4 k T_o F B (\lambda)^2} = \frac{P_t G_t G_r a^2 b^2}{8\pi^2 R^4 k T_o F B} \tag{3.8}$$

For simplicity, the dimensions 'a' and 'b' are approximated to be same and the equations 3.4, 3.5, 3.6, 3.7, 3.8 are evaluated to an approximated SNR as in Table 3.1

| **Shape of payload** | **SNR** | **Approximated SNR** |
|---|---|---|
| Flat plate | $\frac{P_t G_t G_r a^2 b^2}{16\pi^2 R^4 k T_o F B}$ | $\frac{P_t G_t G_r a^4}{16\pi^2 R^4 k T_o F B}$ |
| Sphere | $\frac{P_t G_t G_r \lambda^2 a^2}{64\pi^2 R^4 k T_o F B}$ | $\frac{P_t G_t G_r \lambda^2 a^2}{64\pi^2 R^4 k T_o F B}$ |
| Triangular Trihedral | $\frac{P_t G_t G_r a^4}{48\pi^2 R^4 k T_o F B}$ | $\frac{P_t G_t G_r a^4}{48\pi^2 R^4 k T_o F B}$ |
| Rectangular Trihedral | $\frac{3 P_t G_t G_r a^4}{16\pi^2 R^4 k T_o F B}$ | $\frac{3 P_t G_t G_r a^4}{16\pi^2 R^4 k T_o F B}$ |
| Dihedral | $\frac{P_t G_t G_r a^2 b^2}{8\pi^2 R^4 k T_o F B}$ | $\frac{P_t G_t G_r a^4}{8\pi^2 R^4 k T_o F B}$ |

Table 3.1: SNR of payload shapes calculated from Radar equation

In the following sections, the shape of the payload and drone are approximated to be in the form of a sphere for the calculation of RCS for the different DJI drone models. The difference between combined RCS of drone and payload and RCS of drone alone helps in evaluating the feasibility of considering RCS as a parameter.

## 3.2 RCS of payloads on DJI drone models

In a perfectly conducting sphere, the cross-polarization of back-scattered waves are ideally equal to 0, as the waves dispersed from a perfectly conducting sphere are symmetrical, and hence are co-polarized with the incident waves [25], [26]. Figure 3.2 depicts the regions, namely, 'Rayleigh', 'Mie', and 'Optical' regions obtained from the back-scattered RCS of a perfectly conducting sphere.

- Firstly, the Mie region is also called the resonance region, due to its oscillating nature and the expression for Radar Cross Section (RCS) for a perfectly conducting sphere in the Mie region is in the form of a Bessel function and is expressed as:

$$\frac{\sigma}{\pi a^2} = \frac{j}{ka} \sum_{n=1}^{\infty} (-1)^n (2n+1) \left[ \left( \frac{ka J_{n-1}(ka) - n J_n(ka)}{ka H^1_{n-1}(ka) - n H^1_n(ka)} \right) - \frac{j_n(ka)}{H^1_n(ka)} \right] \tag{3.9}$$

  where the radius of the sphere is 'a', wavelength is '$\lambda$', $J_n$ is the Bessel function for a sphere of kind 1 and order 'n', $H^1_n$ is the Hankel function of order 'n', and 'k' is equivalent to $2\pi/\lambda$.

- Secondly, in the Rayleigh region, the circumference of the sphere as a function of its wavelength is much less than 1. The RCS of a sphere in this region is given by $\sigma$ that is approximately equal to $9\pi a^2$; where the radius of the sphere 'a' is much smaller than the wavelength '$\lambda$'.

- Finally, the optical region (which is taken into account when computing the RCS of the sphere in this report) is substantially larger in comparison to its wavelength. As a result, the RCS of the sphere in this region is represented as $\sigma = \pi a^2$; where the radius of the sphere 'a' is much greater than the wavelength '$\lambda$'.

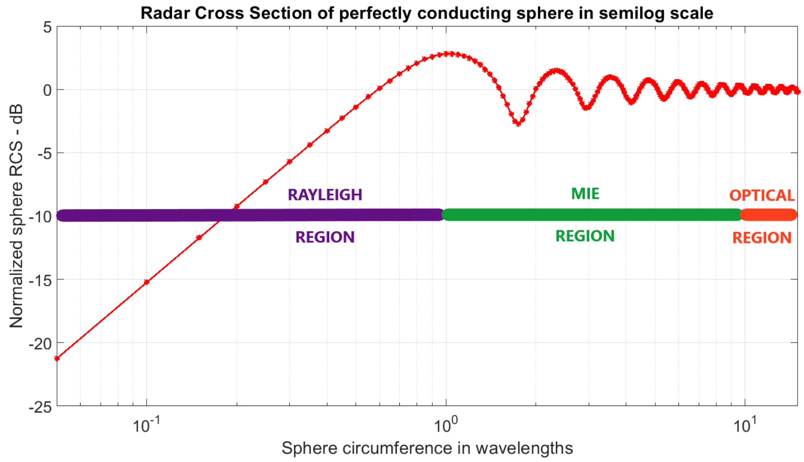


Figure 3.2: Radar Cross Section of perfectly conducting Sphere in different regions: Rayleigh, Mie and Optical [25]

The Radar Cross Sections of various shapes of payloads can be seen in 3.1, and their relation with SNR is summarized in Table 3.1 along with their approximated value of SNR. Further moving on in this domain, a simple payload in the shape of a sphere is considered. Investigation on variations in RCS of drone and payload are made, by assuming realistic values as radius for the sphere. Figure 3.3 depicts the generalized plot for radar cross section of a sphere as a function of frequency. The main objective of starting to calculate the RCS of the sphere is that there is no aspect angle in this scenario as it is symmetrical when viewed in all directions. Thus, there is no dependence on the aspect angle in the case of a sphere, whereas, for other shapes, the aspect angle plays one of the major roles as it depends in which direction the radar sees the payload. Initially, the feasibility of the detection of drone along with its payload in the form of a sphere is evaluated and examined, and later the same analogy can be extended in estimating the RCS of other payload shapes, by also considering its aspect angle.

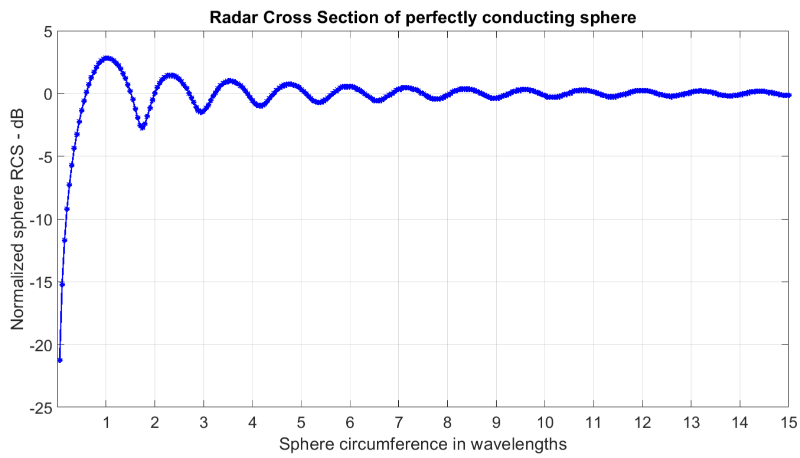


Figure 3.3: Radar Cross Section of a perfectly conducting Sphere as a function of wavelength [25]

The Table 3.2 provides information on the spectrum of bands in which a radar can operate [27]. This information can be used to plot the radar cross sections of spherical payloads and drones and use them as a parameter to verify if they are in the comparable range of their cumulative weights. The difference in RCS (in dBsm) obtained between the RCS of spherical payloads and drones VS the RCS of drone alone will provide an idea if the RCS can be used as a viable constraint for the detection of drones carrying payloads.

| Radar Band | Wavelength | Frequency |
|---|---|---|
| L- Band | 15cm to 30 cm | 1 to 2 GHz |
| S- Band | 7.5 cm to 15 cm | 2 to 4 GHz |
| C- Band | 3.75 cm to 7.5 cm | 4 to 8 GHz |
| X- Band | 25 cm to 37.5 cm | 8 to 12 GHz |
| Ku- Band | 16.7 mm to 25 mm | 12 to 18 GHz |
| K- Band | 11.3 mm to 16.7 mm | 18 to 26.5 GHz |
| Ka- Band | 5.0 mm to 11.3 mm | 26.5 to 40 GHz |
| Q- Band | 6.0 mm to 9.0 mm | 33 to 50 GHz |
| U- Band | 5.0 mm to 7.5 mm | 40 to 60 GHz |
| V- Band | 4.0 mm to 6.0 mm | 50 to 75 GHz |
| W- Band | 2.7 mm to 4.0 mm | 75 to 110 GHz |
| F- Band | 2.1 mm to 3.3 mm | 90 to 110 GHz |
| D- Band | 1.8 mm to 2.7 mm | 110 to 170 GHz |

Table 3.2: Radar Band Designation by IEEE, taken from [27]

From the Da-Jing Innovations of Unmanned Aerial Vehicles (DJI) [19], the specifications of certain models of drones are taken for further evaluation. One of the main criteria for evaluation is the dimensions of the drone. As the specifications vary from one model of drone to another owing to its widespread domains of applications, the weight it can hold also keeps fluctuating among the models. As a result, the weight of the payload (on which the time of flight of the drone largely depends) that each of the selected drones is designated to carry is taken into account. The choice of selecting these models are based on the wide range of dimensions, ranging from 80 g by DJI Mavic Mini/ Mini 2 to up to 20 kg carried by DJI Agras T20, which is dependent also on their purpose of usage. Thus, evaluating such a vast variety of dimensions will aid in predicting if RCS is a suitable metric for the detection of drones carrying payloads.

One of the crucial concerns that arises is the shape of the payload. As mentioned earlier, spherical payloads are initially used. From the Table 3.3, the realistic mass of the payload can be deduced. However, having considered the payload to be in the form of a sphere, the radius is to be calculated initially before evaluating the RCS. Using the mathematical formula for density, mass and volume, the value for radius is computed. It is to be noted that for some of the values in the table, a range of weights is given for the payloads, and this depends on the mode of operation and the intent of drone usage. Therefore, all of the mentioned data are utilized in order to gain a better grasp while computing the radar cross section of the sphere.

| DJI Drone Model | Weight of payload it can carry [1] | Dimensions of Drone (LxWxH) | Diagonal distance of Drone |
|---|---|---|---|
| General DJI Drone | 460 g | NA | NA |
| DJI Mavic | 1000-1200 g (or) 300-400 g | 168 x 184 x 64 mm | 213 mm |
| DJI Mavic 2 | 1100 g | 322 x 242 x 84 mm | 354 mm |
| DJI Mavic Mini/ Mini 2 | 80 g | 245 x 289 x 55 mm | 213 mm |
| DJI Agras T20 | 15100-20000 g | 2509 x 2213 x 732 mm | 1883 mm |

Table 3.3: Weight of payload that can be carried by different models of DJI drones [27]

[1] The weights of the payloads have been rounded- off to nearest whole numbers while conversion from lbs to grams. For some drone models (Mavic and Agras T20), the maximum and minimum ranges of weights of payload are taken.

### 3.2.1 Radius and RCS calculation of metallic spherical payloads

The information about the weight of the payload each model of DJI drone is designated to carry is summarized in Table 3.3. However, there is not much knowledge about the shape of the payload or its dimensions. Therefore, in this section, the dimensions of the payload are assessed and further, their radar cross sections are evaluated.

To measure the dimensions of the payload, some major assumptions are made:

- The payload is considered to be in the shape of a sphere, and it would lie in the optical region, where the size of the sphere is much larger in comparison to its wavelength.
- The material with which the payload is composed is Aluminium (density is 2.7 g/ $cm^3$).
- One of the main ideas behind assuming a metallic sphere is that, in the case of a non-metallic sphere like plastic, the possibility of it being detected by the radar is too less due to its flimsy nature, and hence a metallic sphere which has a higher probability of being detected by the radar is taken into consideration.

Thus, to get realistic values of the radius of a sphere, the volume of the sphere is evaluated using the mathematical formula:

$$\begin{aligned}\text{Density} &= \frac{Mass}{Volume}\\ \text{Volume} &= \frac{Mass}{Density}\\ \text{Volume of sphere} &= \frac{4}{3}\pi r^3\\ \text{RCS of sphere at high frequency in the optical region} &= \pi * radius^2\end{aligned} \tag{3.10}$$

The elaborate calculations for the radius of metallic spherical payload that the different drone models carry and its RCS are deduced in detail in this subsection. The comprehensive estimate of the radius and respective radar cross section for the payload is deduced for a generalized DJI drone payload, and for a particular model DJI Mavic carrying 1000g payload. The evaluations of radius and RCS of the other drone models from Table 3.3 can be found in Appendix A.

- *Radius of payload for general DJI drone:*

$$\begin{aligned}\text{Mass} &= \text{Density * Volume}\\ Volume &= \frac{Mass}{Density}\\ \text{For a general DJI drone, weight of payload} &= 460g\\ \text{Density of Aluminium} &= 2.7g/cm^3\\ Volume &= \frac{460g}{2.7gcm^{-3}} = 170.37cm^3\\ \text{Volume of sphere} &= \frac{4}{3}\pi r^3 = 170.37cm^3\\ \text{Radius of payload} r_{DJIgeneral} &= 3.44cm\\ \text{RCS of sphere at high frequency in the optical region} &=\\ \pi * r_{DJIgeneral}^2 &= 3.14 * (3.44)^2 = 37.16cm^2\end{aligned} \tag{3.11}$$

- *Radius of payload for DJI Mavic with payload of 1000 g:*

$$\begin{aligned}
\text{Mass} &= \text{Density * Volume} \\
Volume &= \frac{Mass}{Density} \\
\text{For a DJI Mavic drone, weight of payload} &= 1000g \\
\text{Density of Aluminium} &= 2.7g/cm^3 \\
Volume &= \frac{1000g}{2.7gcm^{-3}} = 370.37cm^3 \\
\text{Volume of sphere} &= \frac{4}{3}\pi r^3 = 370.37cm^3 \\
\text{Radius of payload} r_{DJImavic1000} &= 4.46cm \\
\text{RCS of sphere at high frequency in the optical region} &= \\
\pi * r^2_{DJImavic1000} &= 3.14 * (4.46)^2 = 62.46cm^2
\end{aligned} \tag{3.12}$$

The results radius and radar cross sections of designated payloads of the various DJI models are reported concisely in Table 3.4.

| **DJI Drone Model** | **Weight of payload** | **Radius of sphere payload in cm** | **RCS of sphere in $cm^2$** | **RCS of sphere in dBsm** |
|---|---|---|---|---|
| General DJI | 460 g | 3.44 | 37.16 | -24.30 |
| DJI Mavic | 1000 g | 4.46 | 62.46 | -22.04 |
| DJI Mavic | 1200 g | 4.73 | 70.25 | -21.53 |
| DJI Mavic | 300 g | 2.98 | 27.88 | -25.55 |
| DJI Mavic | 400 g | 3.28 | 33.78 | -24.71 |
| DJI Mavic 2 | 1100 g | 4.60 | 66.44 | -21.78 |
| DJI Mavic Mini/ Mini 2 | 80 g | 1.92 | 11.58 | -29.36 |
| DJI Agras T20 | 15100 g | 11.01 | 380.63 | -14.19 |
| DJI Agras T20 | 20000 g | 12.09 | 458.97 | -13.38 |

Table 3.4: RCS of spherical payloads carried by DJI drones in optical region

It can be seen that the radar cross section fluctuates from -13 dBsm to -25 dBsm. Nonetheless, major conclusions can not be derived with the RCS of payloads alone, hence, in the following section, the RCS of the drone is evaluated in order to draw further analyses.

### 3.2.2 RCS of drone calculated by approximation of drone geometry

The radar cross sections of various drone models are investigated. Since the drone is a complex structure, it makes it complicated to calculate the RCS, since it depends on aspect angle, orientation of the drone and multiple other factors. However, here again for simplicity, the shape of the drone is assumed to be spherical, and the radar cross section is evaluated as follows:

- *RCS of a spherical shaped drone by approximating DJI Mavic and Mavic Mini/Mini 2 of diagonal distance 213 mm*

$$\begin{aligned}
\text{RCS of sphere at high frequency in the optical region} &= \\
\pi * \frac{diagonal}{2}^2 &= 3.14 * (0.1065)^2 = 0.036m^2 \\
\text{In log scale} &= -14.44dBsm
\end{aligned} \tag{3.13}$$

- *RCS of a spherical shaped drone by approximating DJI Mavic 2 of diagonal distance 354 mm*

$$\begin{aligned} &\text{RCS of sphere at high frequency in the optical region} = \\ &\pi * \frac{diagonal^2}{2} = 3.14 * (0.177)^2 = 0.098 m^2 \\ &\text{In log scale} = -10.09 dBsm \end{aligned} \tag{3.14}$$

- *RCS of a spherical shaped drone by approximating DJI Agras T20 of diagonal distance 1883 mm*

$$\begin{aligned} &\text{RCS of sphere at high frequency in the optical region} = \\ &\pi * \frac{diagonal^2}{2} = 3.14 * (0.9415)^2 = 2.78 m^2 \\ &\text{In log scale} = +4.44 dBsm \end{aligned} \tag{3.15}$$

The values obtained from the RCS of drone and that of payload, it is inferred that they both fall into a comparable spectrum of outcomes.

The important criteria to notice is if the difference in combined RCS of drone and payload and that of the drone alone lies in the comparable range. So, for that purpose, the RCS of payloads and drone (in linear scale) from the previous, calculations are summated and compared with the RCS of drone alone (after conversion to log scale) and the delta change is identified.

| **DJI Drone Model** | **Weight of payload** | **Combined RCS of Drone and Payload in dBsm** | **RCS of Drone in dBsm** | **Difference $\delta_{(drone+payload)-drone}$ in dBsm** |
|---|---|---|---|---|
| DJI Mavic | 1000 g | -11.43 | -14.44 | 3.01 |
| DJI Mavic | 1200 g | -11.31 | -14.44 | 3.13 |
| DJI Mavic | 300 g | -12.37 | -14.44 | 2.07 |
| DJI Mavic | 400 g | -12.15 | -14.44 | 2.29 |
| DJI Mavic 2 | 1100 g | -8.07 | -10.09 | 2.02 |
| DJI Mavic Mini/ Mini 2 | 80 g | -13.04 | -14.44 | 1.40 |
| DJI Agras T20 | 15100 g | +5.40 | +4.44 | 0.96 |
| DJI Agras T20 | 20000 g | +5.49 | +4.44 | 1.05 |

Table 3.5: Comparison of RCS of combined values of spherical payloads carried by spherical DJI drones VS RCS of spherical DJI drones in optical region

The Table 3.5 leads to question the assumption of considering RCS as one of the parameters for detection of drones carrying payloads. The answer is 'NO', since it is verified that *RCS of drone + RCS of Payload ≈ RCS of drone alone.*

Thereby, from modelling the Radar Cross Section (RCS) of the payloads and that of the drone, and also by taking into account realistic values into consideration (by approximations), it can be arrived at a conclusion that the Radar Cross Section cannot be considered as a reliable parameter for the detection of Unmanned Aerial Vehicles (UAVs), a.k.a, drones carrying payloads. Some observations can be made from Tables 3.4 and 3.5.

- The RCS values are for Aluminium spherical payloads for different values of radius. Except for the payloads in DJI Agras T20 series, every other payload of the DJI models falls in the range from -20 dBsm to -25 dBsm. One of the main reasons is attributed to the fact that Agras T20 is particularly designed for agricultural use for spraying of pesticides and chemicals in the fields, while, on the other hand, other DJI drones are used mainly for commercial purposes in the field of transportation and photography.

- An analysis could be made that at lower frequency ranges (in Rayleigh or Mie regions), it becomes difficult for the radar to uniquely distinguish between the different RCS of the payloads. Hence, one might get an incorrect data on the weight of the payload carried by the drone (if at all the RCS is being used as a parameter for consideration). This again proves that RCS might not be the correct hypothesis to be taken into account in the scenarios of detecting drones carrying payloads.
- From Table 3.5, the combined RCS of drone and payload, and that of the drone alone is almost similar and there is a minimal difference, so there is a probability that the radar will view the two objects as a single entity.

Therefore, from the mathematical modelling, and as well as from literature, Radar Cross Section is not the optimum factor for consideration, as it does not help in distinctly identifying drones alone and drones carrying payloads, since, in most of the scenarios, they are seen as drones alone. It is also to be noted that the instances that are used here for calculation are realistic values of dimensions (geometry approximated to spherical). However, this is only for a particular range of drones and their designated capacity to hold payloads. Hence, other parameters like tip velocity and rotor motion are considered to analyse if those criteria can be considered for analysis.

## 3.3 Micro-Doppler signatures of drones carrying payloads

From the works of literature and also by mathematical modelling, it is seen that there is a lacklustre correlation between the RCS of drone and the RCS of its payload. The payload and the drone considered in the mathematical modelling were mostly approximated, however, in realistic cases, the targets are more complex, and other parameters, such as the aspect angle are also considered. Thus, the RCS is not always reliable to discriminate the presence of payloads due to its fluctuations. Hence, the focus of this research is based on the investigation of the micro-Doppler signatures of the drones carrying payloads.

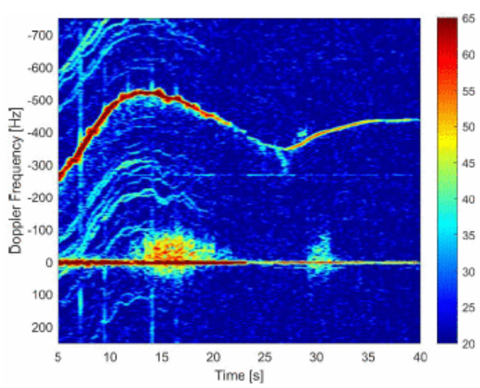


(a) Mortar grenade being dropped into water by drone

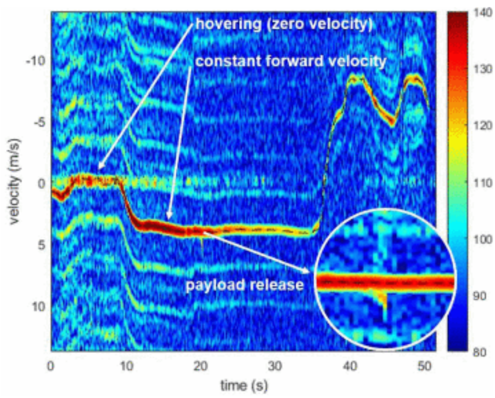


(b) Hand grenade being dropped by drone

Figure 3.4: Analysis of variation in micro-Doppler signatures due to the presence/absence of payloads [10]

The experimental research by [10] consisted of CW (Continuous Wave) and FMCW (Frequency Modulated Continuous Wave) radars and a camera for capturing. In both the cases in Figures 3.4 (a) and (b), the drone is carrying a payload, that is being dropped at some point in time. The micro-Doppler signatures of these scenarios reveal a lot of detailed information about the drone's activities.

The Figure 3.4 (a), depicts spectrogram from the FMCW radar. The drone is carrying a mortar grenade which is swinging from the drone's fuselage. Due to the tumbling effect of the mortar grenade, severe vibrations are experienced by the fuselage which is reflected on the spectrogram from 5s to 20s. Approximately 25s into the game, the drone drops the mortar grenade, which is seen as a dip in the spectrogram with a loss of intensity. The trajectory of the falling payload in mid-air is seen as a blue streak at 27s, and once it touches the surface of the water body at 30s-32s, the impact on the water is seen as a splash, that can also be observed from the spectrogram. The continued movement of the drone after releasing the payload is shown from 35s onwards.

In another similar scenario, the drone carrying a hand grenade is hovering for a few seconds, and at approximately 9s, the drone speeds up and makes an outbound movement and flies for 10s more, before releasing the hand grenade at 20s. Though the drop is not as visible in the spectrogram as in the previous case (due to differences in the weights of the payloads hand and mortar grenades), it is seen as a short spike in the enlarged Figure in 3.4 (b). Also, it can be observed from the spectrogram that there is no discernible difference in velocity during the dropping of payload, however, the further motion of the drone shows variation in velocity.

In the literature [23], two innovative components are covered based on (a) subjecting the drone to lift hefty payload weights and (b) resembling the rebound mechanism of a firearm that is affixed to the fuselage of the UAV.

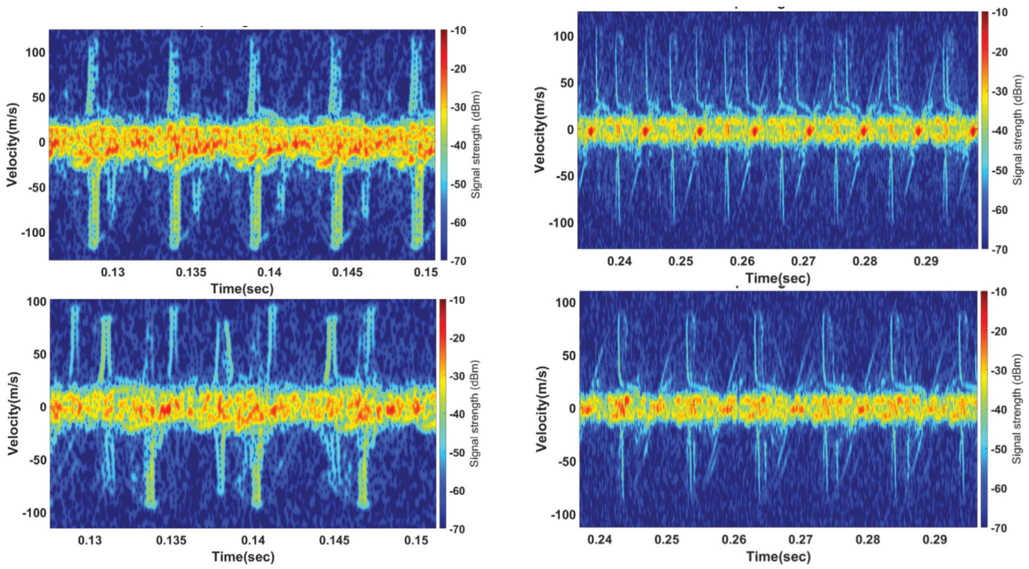


(a) Top: Blade velocity= 120 m/s, Payload= 2.5kg; Bottom: Blade velocity= 100 m/s, Payload= 0kg for drone S900

(b) Top: Blade velocity= 100 m/s, Payload= 5kg; Bottom: Blade velocity= 90 m/s, Payload= 0kg for drone Joyance

Figure 3.5: Variation in blade velocity for the presence and absence of payloads illustrated via Doppler spectrogram for drones (a) S900; (b) Joyance JT5L-404 [23]

In the first case where the drone is subjected to carry larger payloads, two scenarios are examined, where the payload is coupled to the main body, and in the next scenario, the payload is made to hang from the main body of the drone. The two drones employed are DJI S900 hexacopter which carried different payloads, and Joyance JT5L-404 drone with a 5 kg payload (similar in [12]). It is observed that the existence of the 5 kg payload created noticeable variations in the micro-Doppler signature. Moreover, a substantial dip in frequency is obtained when a heavier payload is discharged. It is visible from the spectrogram in Figure 3.5 that the tip velocity of the blades reduce once the payload is dropped from the drone. For the DJI S900 carrying 2.5kg payload, the velocity decreased by 20 m/s from 120 m/s, whereas for the JT5L-404, the blade velocity is reduced from 100 m/s to 90 m/s once the payload is released. The faster velocity in the case of a payload is attributed to the fact that the drone has to provide sufficient lift in order to carry the payload, which is also demonstrated in [10].

Secondly, for the case of payloads dangling from the drone's fuselage, the DJI S900 carried up to 2 kg and the payload is manipulated to sway for a considerable amount for a brief time, which is done by instructing abrupt start/stop operations to the drone. As a result of the drone's erratic acceleration, it led the payload to move in the reverse direction from the drone (related to drag by inertia), thus, the overall velocity vectors of the drone and the payload are in opposing positions. Drawing a judgement based on generic circumstances, it is mentioned that this behaviour of drones is less often observed in comparison to feasible scenarios.

Finally, the recoil effect from a dynamic payload is performed using a DJI Phantom 3, and the rebound effect is instigated manually. It is inferred that a sudden impulse (equivalent to the firing of a gun) created by the payload can be visualized in the high-resolution Doppler signature. The recoil (seen as a surge) and counter-recoil (to balance the effect) activities can be observed in the Doppler spectrogram for the fuselage when the impulse is created.

Thus, from these literature reviews, the findings contribute to a better knowledge of the radar signatures of drones carrying payloads and their behaviours. The spectrogram can be conceived as a foolproof and reliable method to visualize the micro-Doppler signatures of the drone and its payloads. So, in this thesis, the spectrogram is used to obtain preliminary results using two experimental datasets, which are discussed in Chapter 4.

## 3.4 Conclusion

In this chapter, the modelling of RCS of drones and payloads are evaluated. Then, the literature studies on micro-Doppler and Doppler signatures are discussed. The significant observations are summarized as follows:

- The findings in [10] and [23] illustrate a lot of information about the drones, the trajectories followed, the impact of payload on their movement and blade velocity.
- The radar cross sections of drones and their payloads are calculated by approximation of their geometries in the shape of a sphere. After evaluation, it is observed that the RCS of the drone and payload lie in the same range of values. Moreover, there is a negligible difference in their corresponding combined and individual RCSs.
- As seen in Table 3.5, the difference in the combined RCS of drone and payload and RCS of drone alone is of the range 1-3 dBsm. So, it is evident that this parameter cannot be used for drone detection and classification because such a margin would be too small compared with its fluctuations in a realistic scenario.
- It is to be noted that the simplistic calculation on RCS is performed to substantiate the theory from literature papers (e.g., from literature [5]) that RCS is not a reliable parameter for detection and classification of drones with payloads. A rigorous study of the RCS of drones and payloads would require precise EM simulations which go beyond the scope of this thesis, hence, this thesis is focused more on the analysis of experimental micro-Doppler signatures.
- It can be inferred from the few examples in the literature papers [10] and [23] in Section 3.3 that the micro-Doppler signature is a wiser parameter to be considered for analyzing the drone activities (with payloads) and their corresponding detection and classification.

# Chapter 4

# Experimental Setups and Datasets

*This chapter discusses the measurement setup and data collection from the two radars: NetRAD (University College London, UCL) and PARSAX (TU Delft). The NetRAD is a coherent pulse radar with horizontal polarization, consisting of 3 radar nodes 1, 2 and 3. The PARSAX is a fully polarimetric Frequency Modulated Continuous Wave (FMCW) radar with VV, VH, HV and VV polarimetric channels. The two radars record the activities of different types of drones carrying payloads of varying weights.*

*Firstly, the NetRAD obtains the activities of drone DJI Phantom Vision 2+ carrying payloads of 0g, 200g, 300g, 400g and 500g for the scenarios of hovering and flying. Secondly, the PARSAX radar is used for recording the next set of data. The measurements are procured using DJI M200 quadcopter (with payloads 0kg and 1kg) and DJI M600 hexacopter (with payloads 0kg and 2.35kg) for the scenarios where the drone is hovering, flying and moving waypoints along a rectangle. The corresponding data pre-processing techniques after data collection are addressed for the two types of radar. Although the two radars are different, such that NetRAD is pulsed radar and PARSAX is FMCW radar, the data processing starts from the initial structure of Range Time Intensity plot (RTI). From the RTI plots, the variation in the path followed by drones for the different scenarios, with and without payloads are examined.*

## 4.1 Data Collection: NetRAD, University College London

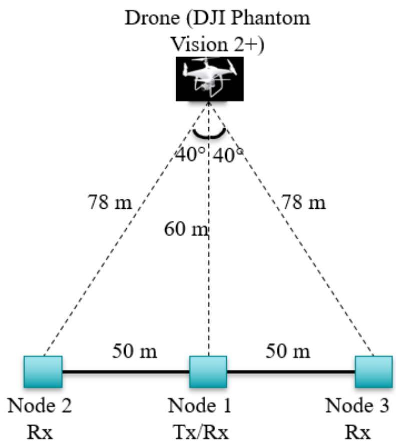


Figure 4.1: Experimental Setup of NetRAD Radar, inspired from [19]

The measurement setup, as shown in Figure 4.1 is collected by employing NetRAD radar, in a football ground at the University College London (UCL). The NetRAD, which is designed at UCL, is a multistatic, 2.4 GHz netted coherent pulse radar with three different but identical nodes in the S-Band. The criteria used to accumulate the measurements are a signal of bandwidth 45 MHz, a linear chirped-pulse of interval 0.6s, a recording duration of 30s, Pulse Repetition Frequency (PRF) of 5 kHz which ensures that the complete micro-Doppler signature of the drone/micro-drone is encompassed within the unambiguous Doppler region. For a more favourable characterization of the micro-Doppler signature of the micro-drones' rotor blades, the horizontal polarization is adopted. The other parameters taken into consideration are that the radar functioned at a modest power level, using a transmission power of +23 dBm, horizontally polarized antennas with a gain of 24 dBi and a beamwidth of ~ 10° x 10° [19].

The NetRAD monostatic transceiver Node 1 is separated from receiver-only bistatic Node 2 and Node 3 by an inter-nodal distance of ~ 50 metres. Two scenarios of flight motion of the micro-drone quadcopter DJI Phantom Vision 2+ are collected, namely hovering and flying. As for hovering, the micro-drone lingered at around 60 metres from the baseline, and the bistatic angle for each bistatic node was about 40°. In the second scenario, the precise trails of the quadcopter, which in this case was flying, approaching Node 1 from a distance of around 90-60 metres from the baseline are recorded.

During the experiment, the default camera is discarded in order to equip the micro-drone with various payloads. The payload comprised of a plastic tray affixed to the quadcopter's underside that included the metallic discs, each of 10 grams in weight. Measurements for the distinct payload weights from 200 grams to 500 grams, in steps of 100 grams are obtained using several similar discs, inclusive of the case where the micro-drone is installed with no payload. A maximum payload weight of 500 grams is taken based on the micro-drone's ability, since it is observed that with 500 grams, although the micro-drone is able to take-off, the flight is slow. It is to be noted that the dataset containing 100 grams payload is discarded due to inconsistencies in the data during recording. Each of the data is recorded for approximately 30s for each class of payloads for the scenarios when the drone is hovering and flying at Nodes 1, 2 and 3, thus, spanning for a duration of 7-10 minutes. The size of the original data comprised of the dimension (150000 x 128) in pulses and range bins, which is consistent for all the recordings (Table 5.1).

## 4.2 Data Collection: PARSAX, Delft University of Technology

The second set of data is collected using PARSAX, which is an S-Band fully polarimetric FMCW Doppler radar (with channels VV, VH, HV, HH), where both the transceiver and receiver have two extremely independent polarimetric RF channels. The radar has a high resolution with a maximum bandwidth of 100 MHz which relates to an equivalent range resolution of 1.5 m. The transmit power for each of the channels is up to 50 dBm, with the noise floor of the receiver in the range of -93 dBm. The PARSAX radar is mounted on roof top of the Faculteit Elektrotechniek, Wiskunde and Informatica (EWI) in TU Delft [28]. The bandwidth for measurement is 50 MHz with a Pulse Repetition Frequency (PRF) of 4 kHz (240 $\mu$s). The measurements are performed in an open ground in the Technical University of Delft, Netherlands. The measured distance between the PARSAX radar and the open ground is approximately 570 m to 575 m, which can be seen from the satellite image in Figure 4.3 (a).

(a) DJI M200 Quadcopter

(b) DJI M600 Hexacopter

Figure 4.2: Drone models DJI M200 Quadcopter and DJI M600 Hexacopter used for data collection using PARSAX radar [29]

Two types of drones are used for this purpose: DJI M200 (Matrices 200) quadcopter and DJI M600 (Matrices 600) hexacopter, in Figure 4.2. The drones are subjected to carry payloads of two different weights. Depending on the designated payload weight the drone is designed to carry, the DJI M200 was made to carry 0 kg and 1 kg, whereas the DJI M600 hexacopter carried 0kg and 2.35 kg. It is to be noted that 0 kg represents when the drone is not carrying any payload. The data are recorded for approximately 30 s, for the scenarios where the drones M200 quadcopter and M600 hexacopter are (a) hovering in the same place, (b) flying back and forth in a 50 m linear path, and (c) moving waypoints in a rectangle of dimensions 60 m x 20 m, for both the cases of with and without payload as shown in figure 4.3 (b)-(c). The data are obtained for multiple recordings of the same scenarios. The entire duration of the recording lasted between 11 and 15 minutes. The subsequent investigation also considered the combined scenario of the drone flying back and forth and in rectangular waypoints in the feature extraction level. The dimensions of the originally recorded data are approximately (114688 x 400), however, for some of the measurements, the dimensions varied since the drone left the radar beam at times (Table 5.2).

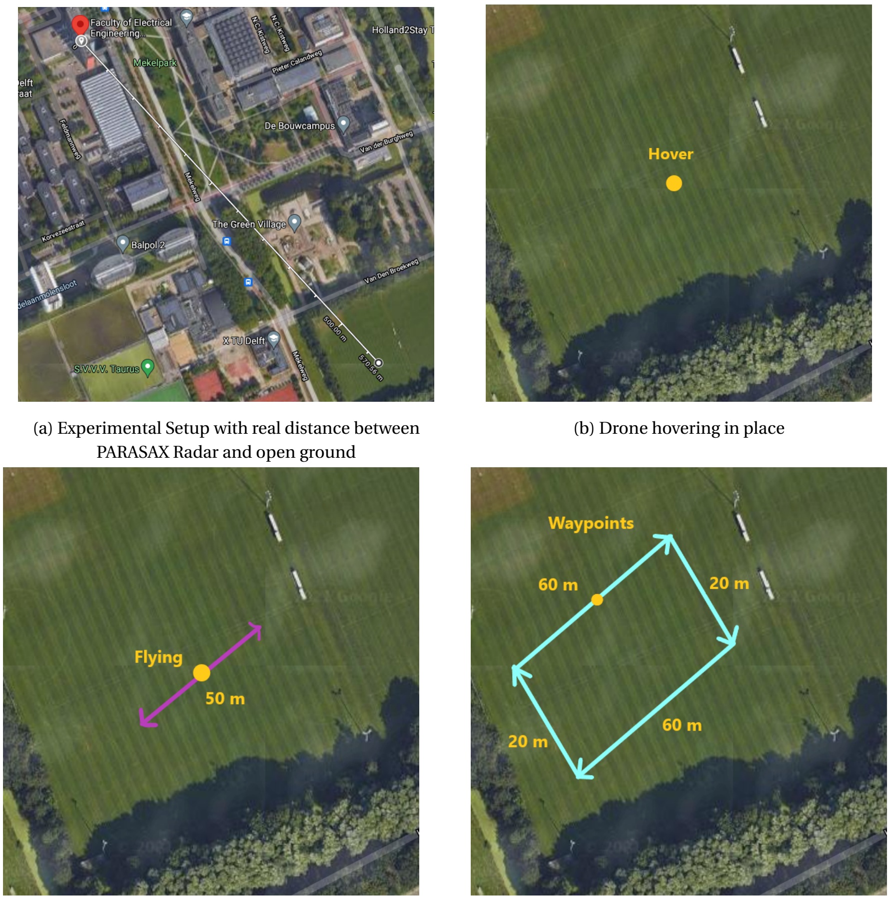


(a) Experimental Setup with real distance between PARASAX Radar and open ground

(b) Drone hovering in place

(c) Drone flying back and forth in 50 m distance

(d) Drone flying in Waypoints in rectangular dimension of 60m x 20m

Figure 4.3: Experimental Setup of PARSAX Radar with drone movement scenarios: (a) Measured distance between PARSAX radar and open ground; (b) Drone hovering; (c) Drone flying; (d) Drone moving along rectangular waypoints

## 4.3 Data Preprocessing

After the data is being collected through the NetRAD measurement setup in Figure 4.1, the unprocessed samples that were obtained from all the nodes were subjected to signal processing to arrive at visual plots. In order to map the data as a Range Time Intensity plot (RTI plot), the original data was subjected to Hilbert Transformation and matched filter was applied over a baseline signal. A constant false alarm rate (CFAR) detector was devised and deployed to dynamically interpret the data by first determining the range cells in which the drone operated and then ascertaining if the drone was hovering or flying [6].

In the case of PARSAX radar from the measurement setup in 4.3, the data from the FMCW radar were processed to generate range-time maps, which were later used to identify the range-time bins containing the signature of the drones in the different recordings. The blade flashes from the rotors and the main body are visible in the Figure 4.4, which represents pictorially the range profile model of a helicopter. The range profiles of the experimental data can be seen from the plots in the following sections.

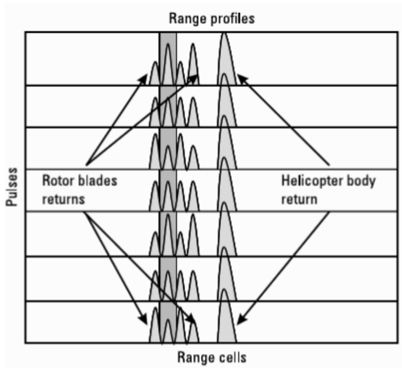


Figure 4.4: Model of range profiles from a drone (helicopter) [30]

## 4.4 Range Time Plot

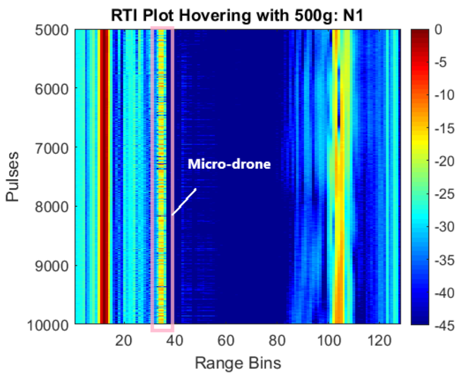


(a) Drone hovering with 500g payload at Node 1

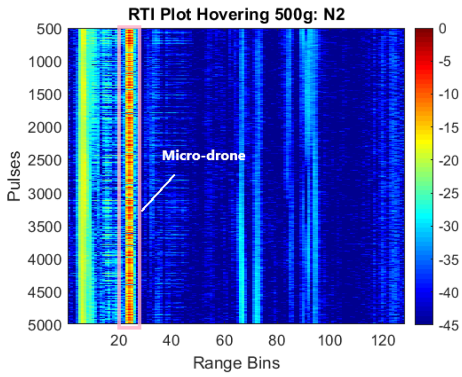


(b) Drone hovering with 500g payload at Node 2

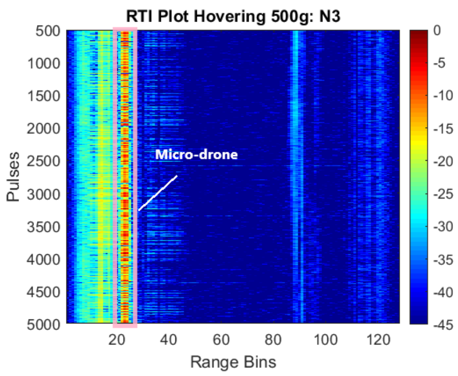


(c) Drone hovering with 500g payload at Node 3

Figure 4.5: RTI Plot for Drone hovering with 500g payload at (a) Node 1; (b) Node 2; (c) Node 3 of NetRAD Radar

In the case of the NetRAD data, the movements of the drone that were recorded are (a) drone hovering and (b) drone flying, whereas, with the PARSAX data, the extra scenario of waypoints in rectangle was also captured. The Range-Time Intensity (RTI) plots for the mentioned scenarios are shown in Figures 4.5- 4.8. As the experiment was conducted in an open ground, both at UCL and TU Delft, the Range-Time plot comprises of range bins where the drone is present, along with other artefacts, such as radar reflections, and the disturbances on the ground. The RTI plot will help in analyzing the high-level bird's eye view of the drones' motion and maneuvering. However, it provides insufficient information while capturing the micro-Doppler specifics of drones, such as blade rotation, velocity of blades, vibrations from the rotor, and other electromagnetic information.

In the scenario of hovering, for both the datasets from NetRAD and PARSAX, the range bins where the drone is present are spread out within few bins (3 to 4 bins) in Figure 4.5. The reason is that the micro-drone is in the same position and only rotating its blades, thus there is only potential energy, and no kinetic energy is observed, given that the main body is stationary. The highlighted regions in Figure 4.5 represent the range bins where the drone carrying 500g payload is present. For the NetRAD radar, Node 1 is in the Line of Sight (LOS) to the drone, and the range bins are expected to have a higher intensity, whereas phase correction was applied on Nodes 2 and 3 in order to make the rage bins more distinguishable. The Nodes 2 and 3 are at about 40° angle to the micro-drone. The diversity in intensity among the nodes is due to the fact that the aspect angle is different and hence each node perceives the drone which is in flight, differently. However, this criteria does not play a major difference possibly, since all the nodes are able to view the rotor blades, irrespective of the direct Line of Sight.

It can be noticed that, as the weight of the payload increases, there is a discernible influence, both on the rotation of the blades as well as in the movement of the micro-drone for both the NetRAD and PARSAX datasets. Though the velocity change in blade flashes is imperceptible with RTI plots, the variation in drone trajectory is quite interesting and can be witnessed evidently for the case of drone flying with payloads, as seen in figure 4.6 (a-f)- 4.8. However, this change in trajectory is not noticed visually from the plot of the drone hovering.

The range bins where the drone is flying is more spread out and wider in comparison to the case where the drone is hovering. This is because the drone is following the trajectory of back and forth motion, unlike the case where the drone is floating still in mid-air, with only the blades rotating, hence achieving both potential energy and kinetic energy of the principal body. Comparing the cases where the drone is not carrying any payload to the case where the drone is carrying a payload of 500g, there is a noticeable difference in the flight of the drone when it is carrying a heavier payload in the NetRAD data. From Figure 4.6 (b), (d), (f), the drone's trajectory is slightly tilted in contrast to the no payload cases in (a), (c) and (e) where the RTI block is more or less rectilinear, which is because the drone is only 2.5 times heavier in weight than the 500g payload which has resulted in the mildly distorted path [29]. By rectilinear RTI block, it is implied that the to and fro motion of the drone is not affected by the weight of the payload, which tends to drag the drone, by interrupting the designated trajectory.

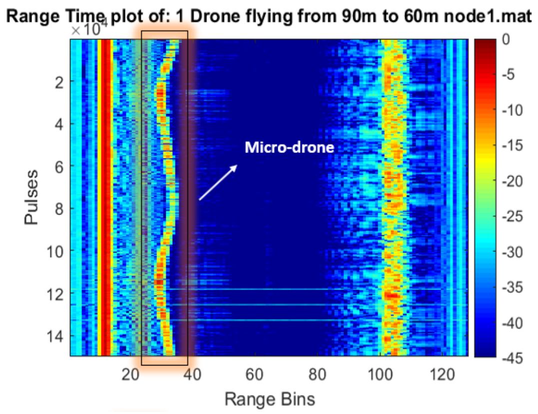


(a) Drone flying without payload at Node 1

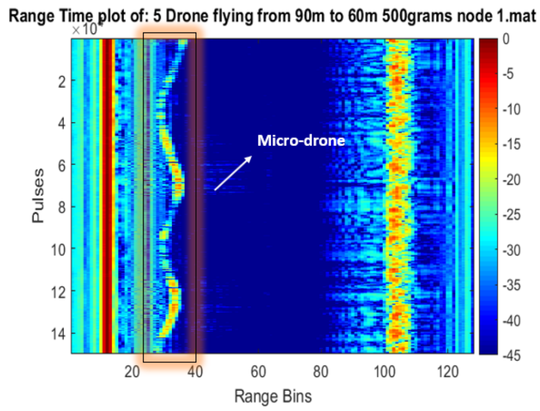


(b) Drone flying with 500g at Node 1

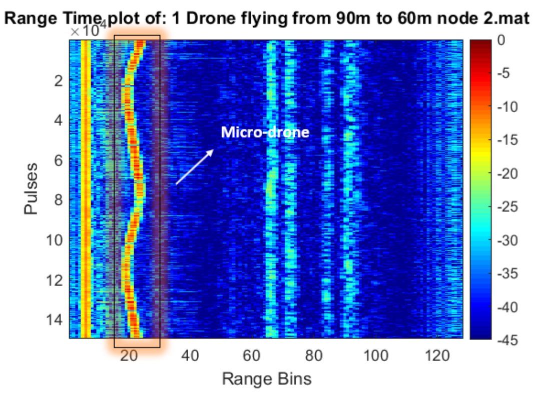


(c) Drone flying without payload at Node 2

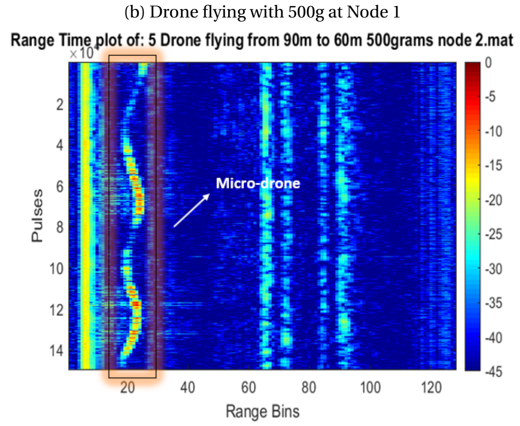


(d) Drone flying with 500g at Node 2

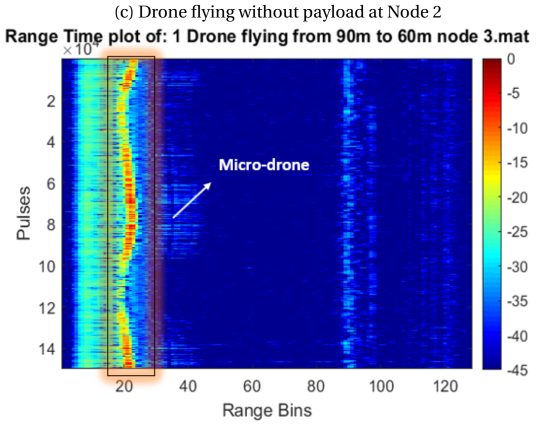


(e) Drone flying without payload at Node 3

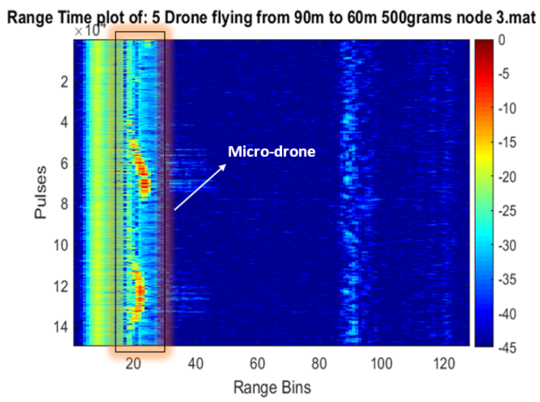


(f) Drone flying with 500g at Node 3

Figure 4.6: RTI Plot for Drone flying with 0g payload at (a) Node 1; (c) Node 2; (e) Node 3 and with 500g payload at (b) Node 1; (d) Node 2; (f) Node 3 of NetRAD Radar

A similar trend in drone locomotion is observed for the PARSAX measurements for quadcopter M200 and hexacopter M600. The Figures 4.7 and 4.8 depict the RTI plots when the hexacopter M600 is flying and moving in rectangular waypoints respectively, with a payload of 2.35kg. The empty blocks in the RTI bins indicate that the drone has left the beam of radar (temporarily), and hence did not appear in those range-time maps. Here, the HH polarization is in the line of sight to the drones, in contrast to other polarizations. This variation in polarization is illustrated in the spectrograms in Chapter 5.

Figure 4.7 which illustrates the hexacopter M600 that is flying with 2.35 kg of payload, has much shorter RTI bins than for the case of hexacopter M600 moving waypoints in a rectangle, as in Figure 4.8. Since the drone is making multiple turns in rectangular waypoints and covering a wider area, the range bins are also broader for this scenario of drone motion. The weights of quadcopter M200 and hexacopter M600 series are approximately 4kg and 9.3kg and are carrying payloads of weights 1kg and 2.35kg [29]. The payloads are much lesser in weight in proportion to their respective drone weights. Hence, due to the sturdiness of the drone, they are not drifted in path even after the payload weight, as opposed to the NetRAD data for drone flying with payload in Figure 4.6 (b), (d), (f).

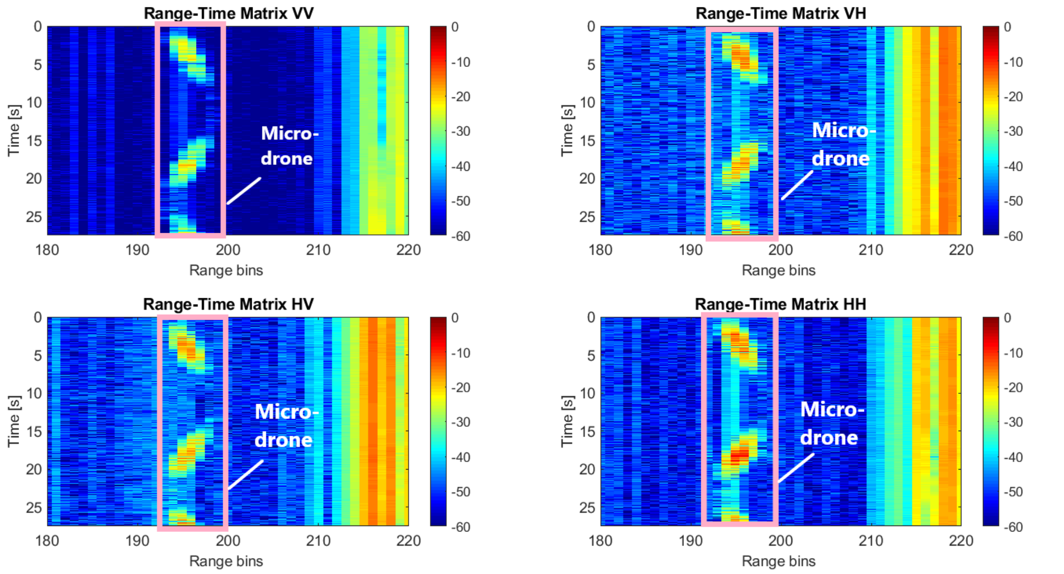


Figure 4.7: RTI Plot at VV, VH, HV and HH channels for Drone M600 Hexacopter Flying with 2.35kg payload of PARSAX Radar

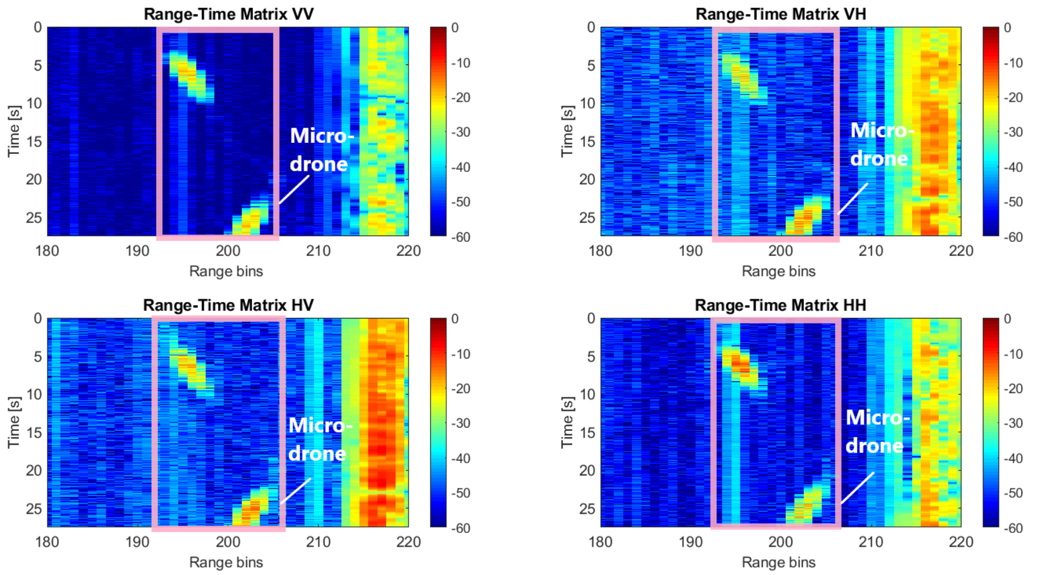


Figure 4.8: RTI Plot at VV, VH, HV and HH channels for Drone M600 Hexacopter in Rectangular Waypoints with 2.35kg payload of PARSAX Radar

## 4.5 Conclusion

In this chapter, the experimental setup of the NetRAD (single polarized) and PARSAX (fully polarized) radars, including the scenarios of the drone trajectory along with the various classes of payloads are discussed. The RTI plots after the corresponding data processing indicate the bins where the drone is present. The important highlights from the RTI plot are summarized below:

- It is observed that the range bins where the drone is present vary largely based on the scenarios. The range bins over which the drone signatures span increase in the order hovering, to flying, to rectangular waypoints scenarios.
- For the hovering scenario in NetRAD and PARSAX datasets, the range bins are linear, irrespective of the weight carried by the drone since the drone is not moving.
- In the case of flying for NetRAD radar, the range bins are shifted slightly when the drone carries a heavy payload (500g). The range bins are continuous in NetRAD dataset, as the drone is always in the beam of the radar.
- For the flying and rectangular waypoints scenarios in PARSAX data, the ranges bins are not continuous due to the drones leaving temporarily at times the beam of the radar. The quadcopter M200 and hexacopter M600 are sturdier to withstand the increased payload weight, thereby not impacting the drones' trajectories.

# Chapter 5

# Research Methodology

*This chapter delves into the main research methodology on the NetRAD and PARSAX datasets, as represented in Figure 5.1. The main contributions of the thesis are highlighted in the yellow blocks.*

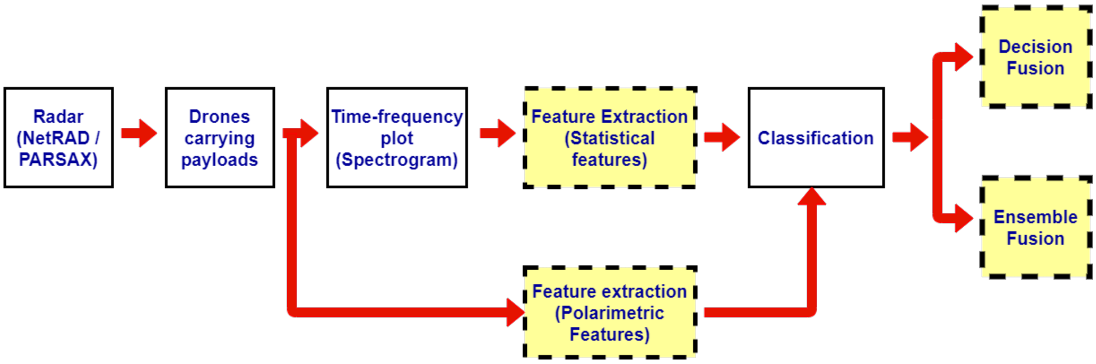


Figure 5.1: Flow chart of Research methodology, with main contribution blocks highlighted in yellow blocks

*Firstly, the impact created on the blade rotation by the different payload weights is depicted by the time-frequency plot- spectrogram. Secondly, significant components of the spectrogram are derived via feature extraction techniques. Two sets of features are generated in this step: (a) the statistical features, that are obtained by applying Singular Value Decomposition (SVD), centroid and bandwidth on the spectrogram; (b) the polarimetric features, by tapping in information from the RTI plot of the fully polarimetric channels, which are confined only to PARSAX data, as fully polarimetric information is required. Thirdly, the samples from the extracted features are passed as input to the selected supervised machine learning classifiers to evaluate the classification performance for all the scenarios of drone movement from the two datasets. Finally, two novel fusion techniques, decision fusion and ensemble fusion are employed to enhance the performance metrics.*

## 5.1 Short-Time Fourier Transform (STFT)

Short-Time Fourier Transform (STFT) is the application of Fourier Transform (FT) to the overlapped short-time windows along a signal [30]. The equation 5.1 is the Fourier Transform of the radar signal s(t) in the time domain. The STFT function which results in a two-dimensional matrix makes use of a window function w(t), whereas s(t) is a one-dimensional vector. The resultant of the magnitude of the Short-Time Fourier Transform, $|STFT(t,\omega)|$ is the spectrogram, which gives the information of the variation in frequency spectrum with respect to the time axis. It is to be noted that the magnitude of the spectrogram in some cases is defined as the power, so it is denoted as the square magnitude.

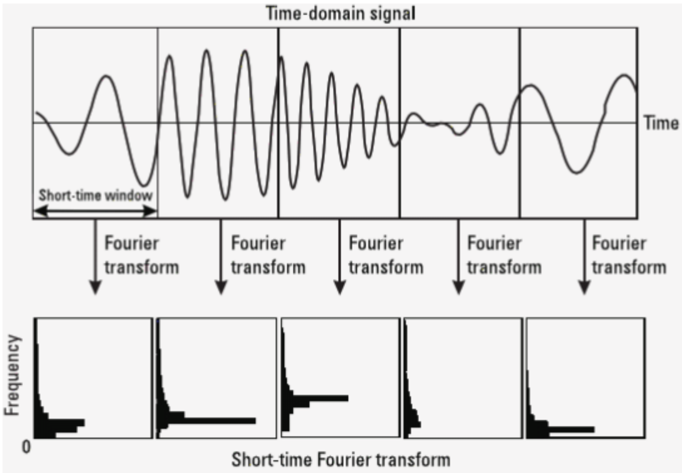


Figure 5.2: Visual Representation of Short-Time Fourier Transform (STFT) [30]

$$S(\omega) = \int_{-\infty}^{\infty} s(t) exp(-j2\omega t) dt \tag{5.1}$$

$$STFT(t,\omega) = \int s(t') w(t'-t) exp(-j\omega t') dt' \tag{5.2}$$

The equation 5.3 denotes the representation of STFT in the frequency domain, which implies that STFT can be retrieved by window moving in time or frequency. One of the observations is that the window size plays a vital role and is constant across the time-frequency and that a signal which has a lesser duration than that of the window is blurred. Likewise, the size of the frequency window influences the resolution in the frequency domain. As a result, there is an inverse proportionality between the window widths in frequency and time. Thus, an inefficient resolution in frequency is entailed due to good resolution in the time domain, and vice versa.

$$STFT(t,\omega) = \frac{1}{2\pi} exp(-j\omega t) \int S(\omega) W(\omega - \omega') exp(-j\omega' t) d\omega' \tag{5.3}$$

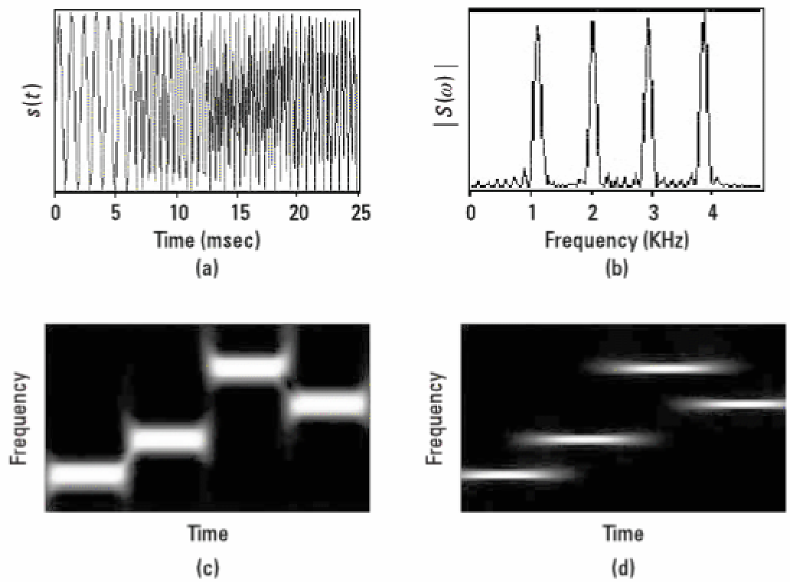


Figure 5.3: (a) A test sinusoidal signal; (b) Fourier Transform of the test signal; (c) Spectrogram with Hanning window size 32 points; (d)Spectrogram with Hanning window size 128 points, [30]

From the Figure 5.3 (c), it is observed that a short window in time has a clear start/stop in time, but blurs the frequency axis (the spectrogram matrix has many columns and few rows). On the other hand, a long window in time in 5.3 (d) has a clear start/stop in frequency, but blurs the durations on the time axis (the spectrogram matrix has many rows and few columns) [30].

Now that the general idea behind STFT and its resultant spectrogram is established, the applications on the two real datasets from NetRAD and PARSAX are discussed.

### 5.1.1 Spectrogram: NetRAD Data

After the Constant False Alarm Rate (CFAR) has effectively determined the significant regions, the double-sided spectrograms are obtained by performing a Short-Time Fourier Transform (STFT) to these spectra of range cells. The discrete window function is given by $w$ and the discrete frequency is represented by $k$. A Hamming window is employed and equation 5.5 (a) is the basis for translation from discrete frequency to Doppler frequency $f_d$. After pre-processing, the sample frequency $f_s$ of the radar is identical to the operable frequency of the radar of 5 kHz and $N$ where $N$ denotes the total count of samples taken during the shot time frame of the window. Again, equation 5.5 (b) could be used to translate between Doppler frequency and velocity, where $\lambda$ is the radar's operational wavelength. The equation 5.5 (c) can be performed to quantify the propellers' angular rotational velocity, in which $\theta$ is the angle between the incoming radar beam and the drone orientation, and $r$ is the size of a single rotor blade.

$$STFT[f_d, n_0] = \sum_{n=-\infty}^{\infty} x[n] \times w[n-n_0] e^{-j2\pi nk/N_s} \tag{5.4}$$

$$\begin{aligned} k &= \frac{N_s f_d}{f_s} \\ v &= \frac{f_d \lambda_{op}}{2} \\ w_{rpm} &= \frac{30v}{\pi r} cos\theta \end{aligned} \tag{5.5}$$

| Payload Weight | Original Data (RTI) | Spectrogram Hovering | Spectrogram Flying |
|---|---|---|---|
| 0 g | 150000 x 128 | 2000 x 5981 | 2000 x 5981 |
| 200 g | 150000 x 128 | 2000 x 5981 | 2000 x 5981 |
| 300 g | 150000 x 128 | 2000 x 5981 | 2000 x 5981 |
| 400 g | 150000 x 128 | 2000 x 5981 | 2000 x 5981 |
| 500 g | 150000 x 128 | 2000 x 5981 | 2000 x 5981 |

Table 5.1: Dimensions of spectrogram (Doppler bins x Time bins) at spectrogram window duration of 0.1s for drone hovering and flying: NetRAD Dataset

The resultant spectrogram is of dimension (2000 × 5981) (Doppler bins x Time bins). The Table 5.1 represents the dimension of the resultant spectrogram after STFT is applied to the original data for the NetRAD radar. The dimensions are same for the different classes of payloads since the spectrogram is continuous for the entire duration. In the scenario for the case of hovering in Figure 5.4, the data used to formulate each spectrogram spanned for the entire duration of recording for 30s. These spectrograms evidently illustrate the parallel lines associated with the spinning of the blades of the micro-drones, as expected from literature studies [31], [32], [33]. The central red line at 0 Hz signifies the main body of the mini-UAV, whereas the horizontal lines in the positive and the negative Doppler regions reflect the intensity of blade flashes and its velocity of rotation. Since the drone is hovering in the air, and there is no movement, the line is straight, indicating the main body of the drone is essentially immobile. Considering the two elevated instances where the quadcopter is hovering without any payload and carrying 500 grams of payload, the contrast in the spectrograms can be noticed objectively, with the blade lines seeming to be smoother and linear in the latter event, as well as the lines approaching higher Doppler frequencies in the positive and negative directions. The blade rotation speeds are influenced majorly by the weight of the drone's payload. The rotor blades are bound to rotate much faster in order to create sufficient elevation when the drone is carrying a significantly heavier payload.

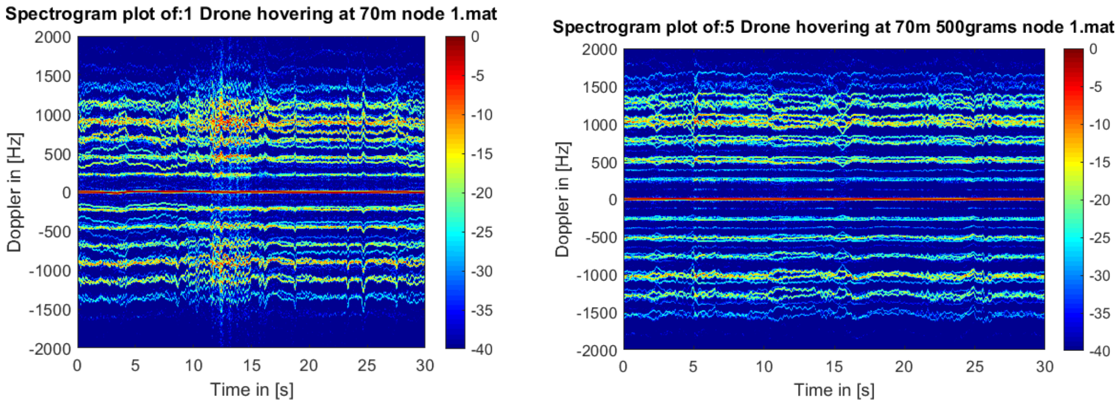


(a) Drone hovering without payload at Node 1

(b) Drone hovering with 500g at Node 1

Figure 5.4: Spectrogram of Drone hovering (a) no payload; (b) 500g payload at Node 1: NetRAD Data

For the case of drone flying, the blade flashes are particularly evident in a way that they illustrate visually the variation in rotational velocity from 0g to 500g, and also the motion of the main body is depicted well. In the Figure 5.5 (b), since the drone is carrying a 500g payload, the central line denoting the main body of the drone seems to have more deviations in contrast to the case when the drone is not carrying any payload. It should be emphasized that the Figures 5.4 and 5.5 (a-b) are the spectrograms that are outcome as observed by Node 1. Since Node 1 is in the Line of Sight to the drone, the spectrograms are sufficiently clear (as also seen in the RTI plots in Figure 4.6). However, in the case of Node 2 and Node 3, phase correction was imposed on their respective RTI plots to generate spectrograms that have fewer distortions. The study is subjected to different parametric analyses (delineated in Chapter 6), such as (a) Dwell time, (b) Varying spectrogram window duration, and (c) Noise of different SNRs; the classification performance at each of these parameters are calculated for further inference. The spectrograms for the other scenarios of the drone hovering and flying with different payloads can be found in Appendix B.

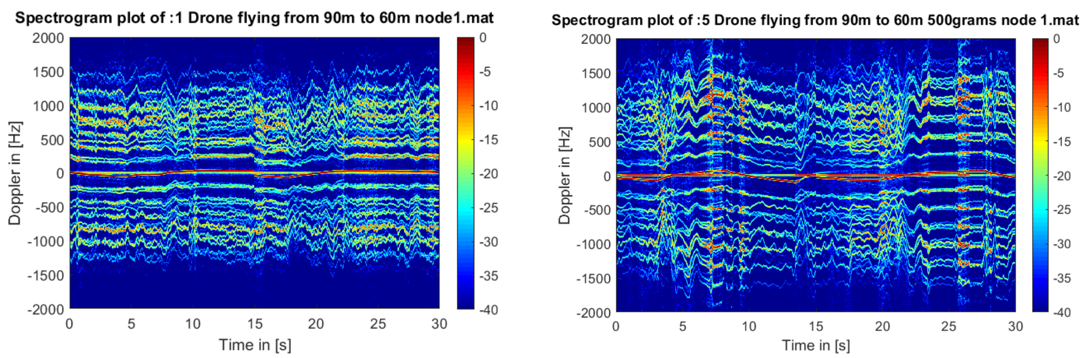


(a) Drone flying without payload at Node 1

(b) Drone flying with 500g at Node 1

Figure 5.5: Spectrogram of Drone flying with (a) no payload; (b) 500g payload at Node 1: NetRAD Data

### 5.1.2 Spectrogram: PARSAX Data

| Drone Model and Payload | Drone Flying | | Drone in Waypoints | | Drone Hovering | |
|---|---|---|---|---|---|---|
| | Original Data (RTI) | Spectrogram Dimension | Original Data (RTI) | Spectrogram Dimension | Original Data (RTI) | Spectrogram Dimension |
| M200 - 0kg | 114688 x 400 | 4164 x 256 | 114688 x 400 | 4164 x 292 | 114688 x 400 | 4164 x 572 |
| M200 - 0kg | 114688 x 400 | 4164 x 262 | 114688 x 400 | 4164 x 83 | | |
| M200 - 1kg | 114688 x 400 | 4164 x 209 | 114688 x 400 | 4164 x 158 | 114688 x 400 | 4164 x 572 |
| M200 - 1kg | 114688 x 400 | 4164 x 242 | 105564 x 400 | 4164 x 208 | | |
| M600 - 0kg | 91168 x 400 | 4164 x 292 | 93567 x 400 | 4164 x 343 | 105563 x 400 | 4164 x 526 |
| M600 - 0kg | 98366 x 400 | 4164 x 271 | 114688 x 400 | 4164 x 284 | | |
| M600 - 0kg | | | 98366 x 400 | 4164 x 203 | | |
| M600 - 2.35kg | 114688 x 400 | 4164 x 345 | 114688 x 400 | 4164 x 284 | 114688 x 400 | 4164 x 572 |
| M600 - 2.35kg | 114688 x 400 | 4164 x 366 | 114688 x 400 | 4164 x 284 | | |

Table 5.2: Dimensions of RTI data and spectrogram (Doppler bins x Time bins) for window duration 0.1s for drone flying, maneuvering in waypoints and hovering: PARSAX Data. The varying dimension of spectrogram is due to the drone temporarily leaving the radar beam. Experiments are recorded for different number of times for each scenario

A similar procedure is followed for the next set of data collected via PARSAX radar, where after identifying the range bins containing the drones and extracting them, a Short Time Fourier Transform (STFT) of 0.1s Hamming window and an overlap of 95% between adjacent windows is applied. Unlike the NetRAD data which has only one polarization, the PARSAX radar has 4 polarimetric channels, as seen from the spectrograms in Figure 5.6. Since HH polarization is in the Line of Sight to the drone, the blade flashes are significant in this polarimetric channel, however, they are also fairly predominant in the cross-polarizations HV and VH also. It is also noted that the extent of blade flashes in Doppler is larger when the drone is carrying a payload, as expected from literature [10], [11] and [19]. The blade flashes are not consistent like in the NetRAD radar data (due to the drones leaving the radar beam at times), so only the contributing portions where the micro-Doppler signatures are present are segmented and used for further analysis in feature extraction and classification algorithms. An observation is that though the blade flashes are visible, clear information about the rotor blade velocity cannot be explained from these time-frequency plots. Similarly, parametric analyses are performed to assess the behaviour at different instances of the parameters to obtain an optimal value for classification.

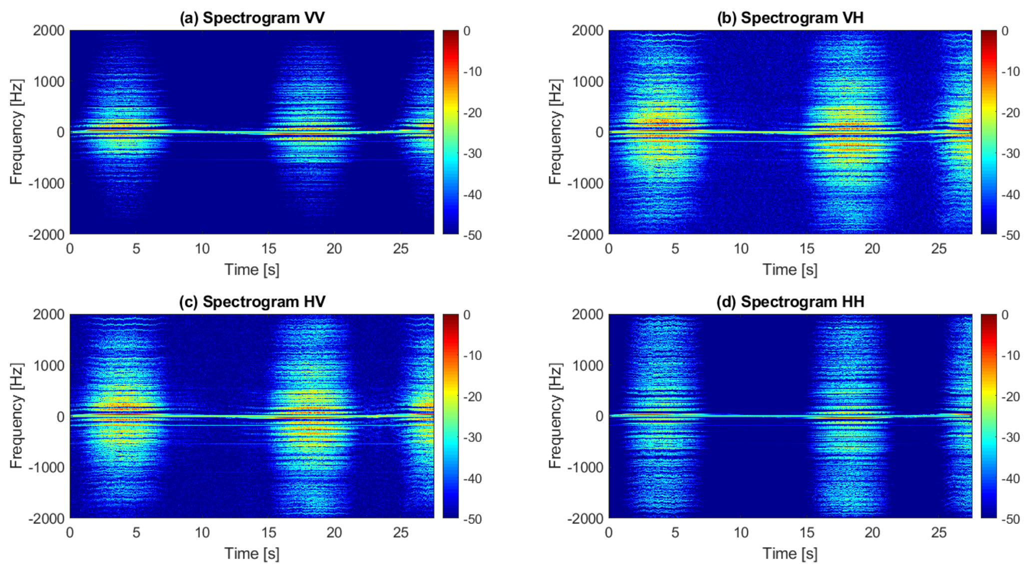


Figure 5.6: Spectrogram Plot for Drone M600 Hexacopter Flying with 2.35kg payload: PARSAX Data

## 5.2 Feature Extraction

Following the generation of spectrogram from the two datasets, the next algorithm is Feature Extraction. Machine learning techniques are predominantly used for the extraction of suitable features from micro-Doppler signatures [34]. Although based on the literature reviews many feature extraction algorithms have been proposed, the strategy that is covered in this thesis is to extract features from the spectrogram directly. These features from the spectrogram neither necessitate pre-processing phases, nor do they demand any evidential cut-off values that are generally required to retrieve periodicity, bandwidth, and other physical attributes of the drone. The goal is to extract certain important features which eventually facilitate higher classification performance, both for standalone classifiers and for their fusion [35]. Hence, for the two datasets from NetRAD and PARSAX radars, the features predicated on Singular Value Decomposition (SVD), Centroid and Bandwidth (BW) are extracted for optimal classification. Moreover, the same set of features are derived from all of the radar nodes (NetRAD) and polarizations (PARSAX) to determine if there is a boost in the performance metrics. This is the initial step for obtaining suitable features to feed as input to the classifiers.

### 5.2.1 Features based on Singular Value Decomposition

The first feature extraction method is via Singular Value Decomposition (SVD). The dimensionality of the feature space can be minimized by this technique since the method involves retaining just the singular vectors corresponding to the greatest singular terms. The specific vectors in SVD are correlated to the physical attributes (blade velocity, periodicity, etc.) of the micro-drone. The spectrograms are subjected to SVD for generating relevant features. When SVD method is performed on a set, the existing matrix is decomposed into a reduced dimension space defined only by the critical elements of the previous original matrix. The Singular Value Decomposition can be mathematically represented as in equation 5.7, for a matrix $X$, where $a \geq b$, the singular terms in $X$ are contained as diagonal elements of $D$ (in the descending order), and the left and right singular vectors are present in the $U$ matrix and $V$ matrix respectively [19]. The dimensions of $D$ matrix are ($a$ x $b$), ($a$ x $a$) corresponds to $U$ matrix, where for $V$ matrix it is ($b$ x $b$). Thus, $U$ and $V$ are called the orthogonal matrix and $D$ is real and is known as the diagonal matrix. By computing SVD, the eigenvalues and eigenvectors of $\mathrm{XX}^T$ and $\mathrm{X}^T\mathrm{X}$ are derived. $V$ matrix comprises of columns of eigenvectors of $\mathrm{X}^T\mathrm{X}$, while the columns in $U$ consist of eigenvectors of $\mathrm{AA}^T$ [19].

$$X \in Y^{axb} \tag{5.6}$$

$$X = \sum_{i=1}^{r} U_i D_i V_i^T \tag{5.7}$$

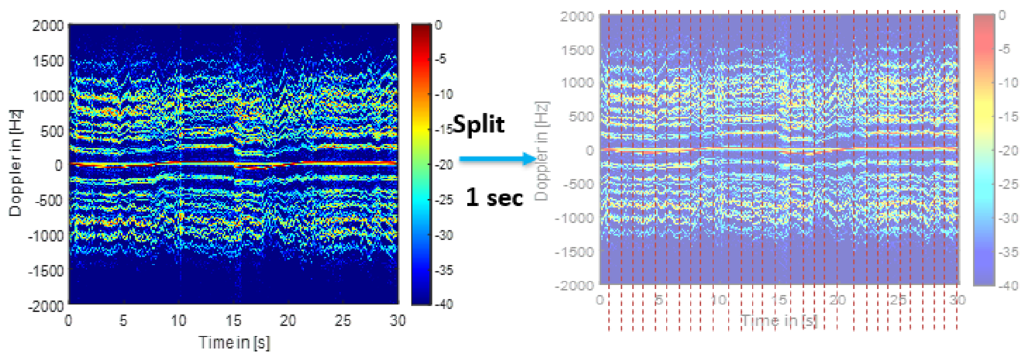


Figure 5.7: Mechanishm of spectrogram split in time for feature extraction

The spectrograms, which are approximately of 30s duration, are segregated into smaller segments in time and in order to capture more suitable features in each block and applying SVD on each of the blocks, rather than applying SVD on the entire spectrogram. Figure 5.7 illustrates how the spectrogram is split in time as 1s. Similarly, the duration of the segments for the parametric analysis is 0.5s, 1s, 1.5s and 2s. The varying duration would help in assessing from the classification accuracy whether a longer or a shorter spectrogram split is ideal. The same algorithm of SVD is applied on both the datasets from NetRAD and PARSAX radars. The idea behind feature extraction by SVD is based on the assumption that significant details are dispersed throughout several vectors in the entire matrices $U$ and $V$, rather than being tightly focused only in a few singular vectors. However, the extracted features from the orthogonal matrices did not indicate notable differences for different payloads. On the other hand, the diagonal matrix contained appropriate features for achieving successful discrimination across the classes. In the case of NetRAD data, the algorithm is performed on each node for the varying dwell time and for all the payload weights when the drone is hovering and flying. For the PARSAX data, the same strategy is performed on all the polarizations for the scenarios where the drone is hovering, flying and maneuvering in rectangular waypoints. Therefore, the statistical features extracted based on SVD from both the datasets are:

- Moment Ordinal 1: Mean of the diagonal matrix
- Moment Ordinal 2: Standard Deviation (SD) of the diagonal matrix
- Moment Ordinal 3: Skewness of the diagonal matrix
- Moment Ordinal 4: Kurtosis of the diagonal matrix

### 5.2.2 Features based on Centroid and Bandwidth

The next set of features are based on Centroid and Bandwidth. The computation of the micro-Doppler signature's centre of mass results in centroid. The calculation of bandwidth of the signature around the centre of gravity is the Doppler bandwidth. The formula for centroid and bandwidth are in equations 5.8 and 5.9 respectively, where the terms denote the *m*th bin Doppler frequency f(*m*) in the centroid equation, *m*th Doppler bin and *n*th time bin of the spectrogram matrix D(*m,n*) in the BW equation [19].

$$fc(n) = \frac{\sum_m f(m)D(m,n)}{\sum_i S(m,n)} \tag{5.8}$$

$$BW_c(n) = \sqrt{\frac{\sum_m (f(m) - f_c(n))^2 D(m,n)}{\sum_m D(m,n)}} \tag{5.9}$$

In the experiments involving analysis of human gait, the centroid and BW based features proved to be very efficient with an accuracy of 98% [36]. This gives the motivation to implement these algorithms for the case of rotating and moving targets like the UAVs. Similarly, just like SVD, the spectrograms are split into smaller segments of varying dwell time for the application of centroid and BW algorithms. The procedure is performed individually on the datasets from NetRAD (Nodes 1,2,3) for drone hovering and flying with payloads 0g to 500g; and from PARSAX (VV, VH, HV, HH polarizations) for the scenarios of drones M200 and M600 hovering, flying, and rectangular waypoint with various payloads. The study also extended to the combined scenario of the drones flying and moving in rectangular waypoints, as this closely resembles the real-life scenario of a drone's trajectory. On the whole, eight features that are extracted are also statistical moments as follows:

- Moment Ordinal 1: Mean of the Centroid
- Moment Ordinal 2: Standard Deviation (SD) of the Centroid
- Moment Ordinal 3: Skewness of the Centroid

- Moment Ordinal 4: Kurtosis of the Centroid
- Moment Ordinal 1: Mean of the Bandwidth
- Moment Ordinal 2: Standard Deviation (SD) of the Bandwidth
- Moment Ordinal 3: Skewness of the Bandwidth
- Moment Ordinal 4: Kurtosis of the Bandwidth

Thus, totally, 12 features are derived based on SVD, Centroid and BW. The Figures 5.8 (a) and (b) represent the distribution of the samples after feature extraction among the five classes of payloads for the drone hovering, taken from the NetRAD radar (Node 1). The samples belonging to their corresponding classes are split well for the features based on centroid and BW, in comparison to that by SVD. However, there are still other features to be considered and complete knowledge about the performance cannot be gauged from just visual depiction of plots. An interesting observation is that, from theory and from the spectrogram plots, it is observed that in principle, with an increase in the payload weight, the velocity of blade rotation also increases to provide enough lift [10]. However, the distribution of samples in the Figure 5.8 (c) seems slightly distorted than that expected from literature. The main reason is that the sample set of the features is limited, and there are possibly other features (such as the empirical physical attributes) that still remain unexplored and can be used for future research. Since the statistical features that were extracted are still able to bring out the essence of the theory, these features are used for further analysis in this research.

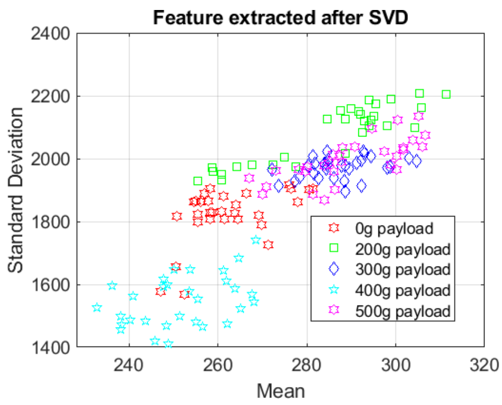


(a) 2D feature plot with Mean and Standard Deviation of SVD

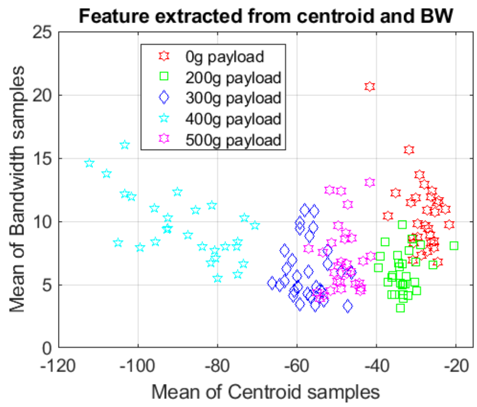


(b) 2D feature plot with Mean of centroid and Mean of bandwidth

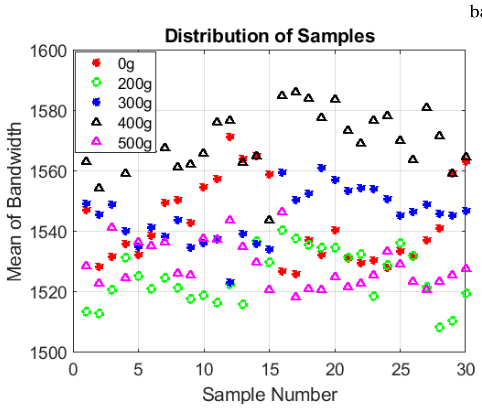


(c) 1D feature plot with Mean of bandwidth and number of samples

Figure 5.8: Feature plots from NetRAD N1 data (a) 2D feature plot with Mean and Standard Deviation of diagonal matrix in SVD; (b) 2D feature plot with Mean of centroid and Mean of bandwidth; (c) 1D feature plot with Mean of bandwidth and number of samples

### 5.2.3 Polarimetric Features

| **Parameter** | **Relation to S** | **Explanation** |
|---|---|---|
| $\delta$ | $2\langle\lvert S_{hv}\rvert^2\rangle/\langle\lvert S_{hh}\rvert^2\rangle$ | Linear depolarization ratio |
| $\gamma$ | $\langle\lvert S_{vv}\rvert^2\rangle/\langle\lvert S_{hh}\rvert^2\rangle$ | Differential polarization ratio |
| $\rho$ | $\langle S_{hh}S_{vv}^*\rangle\sqrt{\langle\lvert S_{hh}\rvert^2\rangle/\langle\lvert S_{vv}\rvert^2\rangle}$ | Co-polarized correlation coefficient |
| $\beta$ | $\langle S_{hh}S_{hv}^*\rangle\sqrt{\langle\lvert S_{hh}\rvert^2\rangle/\langle\lvert S_{hv}\rvert^2\rangle}$ | Cross-polarized correlation coefficient |
| $\epsilon$ | $\langle S_{hv}S_{vv}^*\rangle\sqrt{\langle\lvert S_{hv}\rvert^2\rangle/\langle\lvert S_{vv}\rvert^2\rangle}$ | Cross-polarized correlation coefficient |

Table 5.3: List of polarimetric features extracted, inspired from [8], [37]

The polarimetric features are the special set of features used exclusively for the fully polarimetric PARSAX radar dataset (since NetRAD has only a single polarimetric channel). In [8] polarimetric features contribute positively in improving accuracy for drone vs birds classification. The polarimetric features are especially relevant in the case when the modulations from RCS are non-periodic, such as the case of birds and UAVs whose rotor blades are too fragile to have a substantial meaningful micro-Doppler signature. Multiple scattering techniques, each with its own polarimetric characteristic, may influence the overall scattered field despite the electrical and visually small dimensions of the birds (or drones). The polarimetric features can be retrieved either in the time-frequency domain (e.g., from spectrograms) or in the time domain, and the latter is discussed in this section with an idea to analyze if meaningful features can be derived with a very short dwell time, shorter than the possible spectrogram window in aiding the classification performance constructively. The advantage of this approach would be overcoming the necessity to generate spectrograms for feature extraction, since the features are generated directly from the RTI plots.

$$\mathbf{S} = \begin{bmatrix} \lvert S_{hh}\rvert e^{j\phi_{hh}} & \lvert S_{hv}\rvert e^{j\phi_{hv}} \\ \lvert S_{vh}\rvert e^{j\phi_{vh}} & \lvert S_{vv}\rvert e^{j\phi_{vv}} \end{bmatrix} \tag{5.10}$$

The polarimetric features in Table 5.3 are known as polarimetric inter-correlation parameters, which are applied on the range bins where the drone is present from the range-time plots. From the analysis of the scattering matrix S, it is possible to decipher if relevant information can be derived from the micro-drones (with/without payloads) for classification. The operator $\langle * \rangle$ represents the spatial or temporal ensemble averaging considering the uniformity of random medium [37]. The bins where the drone is present in the range-time plot are split in this case into smaller segments of varying dwell time of 0.05s, 0.10s, 0.25s, 0.50s and 1s and the polarimetric features are extracted. In this scenario, an ensemble of the classifiers is employed to enhance the classification performance, since the features from all polarimetric channels are combined as a single block.

## 5.3 Classification

Classification is an important supervised machine learning (ML) technique which contains all the data samples to be labelled in the training and testing sets. The count of the number of classes is equal to the number of various labels used for tagging the dataset. From the works of literature, for determining the presence of a drone, the binary classification is used, where the two classes are 'drone' VS 'no drone' [7]. Similarly, binary classification is used for discriminating between birds VS drones and two types of drones, wherein the former, the two classes are birds and drones and in the latter, the classes being drone model A and drone model B [8], [18]. While binary classification is more often than not, simplistic, the extended version of it, that is, multiclass classification is very realistic and provides more information about the nature of the targets. [19] discusses the multiclass problems and the classifiers used.

The NetRAD dataset consists of 5 classes, each of the classes being the weight of the payloads 0g, 200g, 300g, 400g and 500g that are carried by the drone. Since the spectrogram is consistent throughout, the number of samples via feature extraction is also the same for the spectrogram split durations, which can be seen in Table 5.4.

PARSAX data is likewise classified as a multiclass problem. Instead of relying on two sets of binary classes (quadcopter M200 carrying payload or no payload; hexacopter M600 carrying payload or no payload), the experiment focused on a more practical multiclass problem by blending the two binary sets. Overall, there are four classes predicated on the type of drone and the payload weight it carries, as depicted in Table 5.5. The number of samples is distributed unevenly among the classes, as only contributing parts were taken from the spectrogram. Thus, the number of samples varies for different scenarios and also for different classes in the same scenario.

As seen in Tables 5.4 and 5.5 the number of samples decreases proportionally when the dwell time is increased, whereas the number of samples is constant when the spectrogram window duration is varied and when noise to vary the SNR is added to the spectrogram, for both NetRAD and PARSAX datasets. The classification by obtaining the number of samples from each class is performed on the scenarios of drone (a) hovering (b) flying for the nodes 1, 2 and 3 of NetRAD data, whereas for PARSAX data, the scenarios were the drones M200 and M600 (a) hovering, (b) flying, (c) maneuvering in rectangular waypoints, (d) combined scenario of flying and rectangular waypoints; for all the polarizations HH, HV, VH and VV.

| **Number of Samples** | | | | | | | | |
|---|---|---|---|---|---|---|---|---|
| **Class** | **Hovering** | | | **Flying** | | | | |
| **Dwell Time** | **0.75s** | **1s** | **2s** | **0.5s** | **0.75s** | **1s** | **1.5s** | **2s** |
| **0g** | 40 | 30 | 15 | 60 | 40 | 30 | 20 | 15 |
| **200g** | 40 | 30 | 15 | 60 | 40 | 30 | 20 | 15 |
| **300g** | 40 | 30 | 15 | 60 | 40 | 30 | 20 | 15 |
| **400g** | 40 | 30 | 15 | 60 | 40 | 30 | 20 | 15 |
| **500g** | 40 | 30 | 15 | 60 | 40 | 30 | 20 | 15 |
| **Total** | 200 | 150 | 75 | 300 | 200 | 150 | 100 | 75 |

Table 5.4: Number of feature samples in each class for different scenarios: NetRAD Data

| **Number of Samples** | | | | | | | | | | | | |
|---|---|---|---|---|---|---|---|---|---|---|---|---|
| **Class** | **Hovering** | | | **Flying** | | | **Rectangle Waypoints** | | | **Flying+Waypoints** | | |
| **Dwell Time** | **0.5s** | **1s** | **1.5s** | **0.5s** | **1s** | **1.5s** | **0.5s** | **1s** | **1.5s** | **0.5s** | **1s** | **1.5s** |
| **M200/ 0kg** | 55 | 27 | 18 | 52 | 27 | 17 | 40 | 19 | 13 | 92 | 46 | 30 |
| **M200/ 1kg** | 55 | 27 | 18 | 48 | 24 | 15 | 39 | 20 | 13 | 87 | 44 | 28 |
| **M600/ 0kg** | 50 | 25 | 16 | 57 | 28 | 19 | 83 | 42 | 28 | 140 | 70 | 47 |
| **M600/ 2.35kg** | 55 | 27 | 18 | 77 | 38 | 25 | 58 | 30 | 20 | 135 | 68 | 45 |
| **Total** | 215 | 106 | 70 | 234 | 117 | 76 | 220 | 111 | 74 | 454 | 228 | 150 |

Table 5.5: Number of feature samples in each class for different scenarios: PARSAX Data

The 12 features have a total number of samples that are split into Training set' and the 'Testing set'.

In the training phase, out of the total number of observations, a certain percentage of samples are given to the supervised classifiers. In this research, for both the datasets, the samples after feature extraction are split into 80% training data and 20% test data. The test data (which is unseen by the classifier) is fed to the trained classifier to make predictions, typically with a form of an estimate of its confidence. The workflow of the classification process is summarized in Figure 5.9

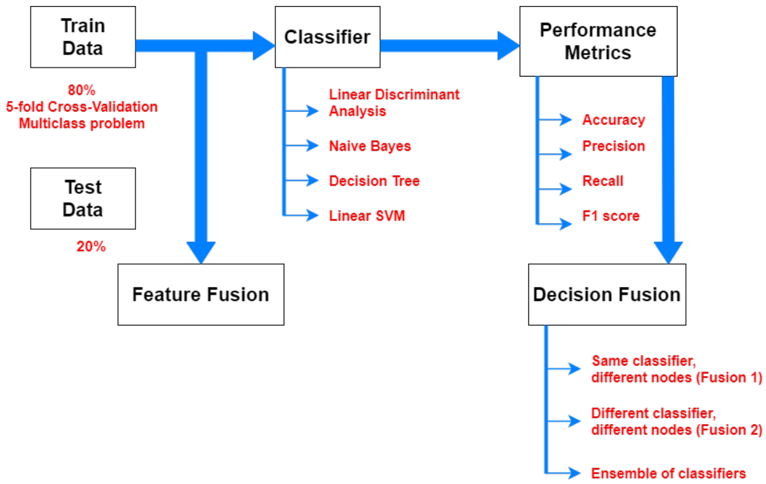


Figure 5.9: Supervised learning classification techniques utilised in this thesis: summarising flow chart

A 5-fold Cross-Validation (CV) is used for assessing the effectiveness of the model, which helps in mitigating overfitting of the data. The cross-validation step is crucial in order to avoid getting a biased result. The CV is broadly divided into three types, they are:

- *One-time split:* This involves the random splitting of the total observations into training and testing sets. This technique is not always suitable, since the result is more often than not, biased.
- *K-fold cross-validation (CV):* In this technique, the entire training set is divided into multiple folds, the classifier is trained on the parts, leaving one part behind for validation in each iteration. Usually, 5-fold cross-validation is used. The procedure continues till the end of the iteration and the average performance is assessed. This strategy is often suitable, since the outcome is unbiased, and the overfitting of data is curbed. The 5-fold cross-validation mechanism is pictorially represented in Figure 5.6.
- *Leave-out validation:* In this method, one part of the data is left out on the basis of specific criteria, such as training some models of drones, and testing on different models of drones; or training on data collected in one location, and testing with data collected by the same radar in another location.

| | | | | | | |
|---|---|---|---|---|---|---|
| | **All data** | | | | | |
| | **Training Data** | | | | | **Test Data** |
| | Fold 1 | Fold 2 | Fold 3 | Fold 3 | Fold 5 | |
| **Split 1** | Fold 1 | Fold 2 | Fold 3 | Fold 3 | Fold 5 | **Finding parameters** |
| **Split 2** | Fold 1 | Fold 2 | Fold 3 | Fold 3 | Fold 5 | |
| **Split 3** | Fold 1 | Fold 2 | Fold 3 | Fold 3 | Fold 5 | |
| **Split 4** | Fold 1 | Fold 2 | Fold 3 | Fold 3 | Fold 5 | |
| **Split 5** | Fold 1 | Fold 2 | Fold 3 | Fold 3 | Fold 5 | |
| | **Final Evaluation** | | | | | Test Data |

Table 5.6: Cross-validation (CV) 5-fold mechanism [38]

### 5.3.1 Types of Classifiers

Based on the computational complexity with the dataset and the classification performance, four classifiers, Linear Discriminant Analysis (LDA), Gaussian Naive Bayes (NB), Decision Tree (DT), and Linear Support Vector Machine (SVM) are chosen. However, some classifiers work well with some features, and other classifiers depend on other features, it is usually complex to gauge which classifier performs better in a general machine learning scenario.

#### Discriminant Analysis

The first classifier used for classification on the datasets is Discriminant Analysis (DA), which is particularly useful when the number of classes is 2 or more than 2, so DA is one of the ideal classifiers for both binary and multiclass classification problems. The two types of Discriminant Analysis are Linear Discriminant Analysis (LDA) and Quadratic Discriminant Analysis (QDA). Both these classifiers differ by the boundary of separation among their classes. The former employs a linear separation (a straight line), while on the other hand, the latter makes use of non-linear separation, such as hyperbola, ellipse, etc. [39]. This technique is built on the hypothesis that each class's data are expressed by a multivariate Gaussian distribution.

$$P_{(x|k)} = \frac{1}{\sqrt{2\pi|\sum_k|}} exp\left(-\frac{1}{2}(x-\mu_k)^T \sum_k^{-1}(x-\mu_k)\right) \tag{5.11}$$

$$\hat{y} = \underset{y=1,2,\ldots,K}{\text{argmin}}\ \hat{P}(k|x)C(y|k) \tag{5.12}$$

In this method, at the classifier's training phase, the constraints of the Gaussian distribution are computed. The constraints are the mean and co-variance, as denoted by $\mu_k$ and $\sum_k$ in the equation of Probability Density Function (PDF). With the objective of reducing the estimated cost of classification $C$ as much as possible, the sample space is partitioned into various parts, with each anticipated classification posterior probability being associated to $C$. Following this, the Linear Discriminant Analysis is considered for further analysis on classification performance [19].

#### Naive Bayes

The next type of classifier employed is the Naive Bayes classifier. Similar to the case of DA classifiers, the Naive Bayes classifier is based on the premise that there is uniform Gaussian distribution of samples of the constituent features of each class, such that the simplified equation comprises the main components, that is, the mean and variance of the features. In this approach, Bayes rule is made use of to represent the posterior probabilities. The posterior probability of a sample corresponding to every class for any unseen test data is computed in this algorithm. From equation 5.15, as per the posterior probability of the highest posterior probability, the testing set is then classified [40]. The Gaussian Naive Bayes is used as the classifier for the PARSAX and NetRAD datasets.

$$p(C_k|x) = \frac{p(C_k)p(x|C_k)}{p(x)} \tag{5.13}$$

$$p(x|C_k) = \prod_{i=1}^{n} P(x_i|C_k) \tag{5.14}$$

$$p(x|C_k) = \underset{k\epsilon 1,2,\ldots,K}{\text{argmin}}\ P(C_k)\prod_{i=1}^{n} P(x_i|C_k) \tag{5.15}$$

$x$: input samples
$k$: class
$p(x)$: probability of samples

$p(C_k)$: probability of classes
$p(C_k|x)$: probability of class $k$ provided samples $x$
$p(x|C_k)$: probability of sample $x$ provided class $k$

**Decision Tree**

The third classifier used in this research is the Decision Tree (DT). The root node, internal node, leaf node and branch are the integral components that constitute the Decision Tree (DT). The uppermost part of the decision tree is the root node, which comprises of no arriving links, on the other hand, the leaf node that has no departing links reflects the decision tree's desired end result. The evaluation criteria or decision rules on a feature are indicated by the internal node, and the test result is conveyed by the branch. The count of leaves utilized to distinguish among the classes determines the classification of the DT algorithm. The main types of DT are based on the number of splits are Fine DT, Medium DT and Coarse DT, where the number of divisions can go from 4 up to 20-100 for Coarse DT and Fine DT respectively [39]. The extended version of this is Random Forest, which is also a supervised machine learning algorithm that uses a sequence of decision trees to classify between distinct initial datasets. Moving forward, the fine decision tree is utilized for classification.

**Support Vector Machine**

The final classifier used is the Support Vector Machine (SVM). SVM operates on the notion of structural risk minimization theory, where it creates an ideal hyperplane considering a collection of positive and negative values. Based on the largest margin that optimally partitions the data point, the SVM chooses the best decision boundary, such that it attains minimal classification error [41].

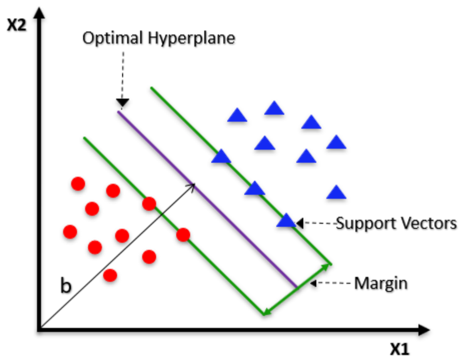


Figure 5.10: Support Vector Machine (SVM) classifier, inspired from [41]

$$a^T m + b = \pm 1 \tag{5.16}$$

The support vectors (as seen in Figure 5.10) are the training samples that are closer to the hyperplane and represented by equation 5.16, where $a$, and $m$ (perpendicular to the decision boundary) are vectors and $b$ is the bias. The three models of kernels of SVM are, Linear, Polynomial and Gaussian.

- *Linear SVM kernel:*

$$Y(m_i, m_j) = m_i^T m_j \tag{5.17}$$

- *Polynomial SVM kernel:*

$$Y(m_i, m_j) = (1 + m_i^T m_j)^k \tag{5.18}$$

dot product is generated by the two vectors $m_i$ and $m_j$ are depicted in a space of order k.

- *Gaussian SVM kernel:*

$$Y(m_i, m_j) = \frac{exp\left(-\|x_i - x_j\|\right)^2}{2\sigma^2} \tag{5.19}$$

where the difference provides the distance between two data points in Euclidean space. The variance, which governs the classifier performance, can be used to alter the width of the Gaussian kernel. For classification of extracted features for the NetRAD and PARSAX datasets, Linear SVM will be used.

### 5.3.2 Performance Metrics

After the classification process, it is essential to analyze the performance metrics. The confusion matrix is an efficient tool to assess the efficacy of the model, since it provides information to observe where the ambiguity lies between the classes and the corresponding misclassification. From the confusion, some vital performance metrics can be derived. The components in the confusion matrix are: True Positive (TP), False Negative (FN), True Negative (TN) and False Positive (FP) [42]:

True Positive (TP): The samples are positive and are also classified as positive.
True Negative (TN): The samples are negative and are also classified as negative.
False Positive (FP): The samples are negative, but are classified as positive.
False Negative (FN): The samples are positive, but are classified as negative.

The performance metrics evaluated from the components of the confusion matrix are:

- *Accuracy:* Accuracy provides the overall performance of the model. It is the ratio of the correctly predicted observations to the total number of observations.

$$Accuracy = \frac{TP + TN}{TP + TN + FP + FN} \tag{5.20}$$

- *Precision:* It is the ratio of the predicted positive outcomes to the total positive outcomes. The Precision reduces if the number of false positives increases, which is not desirable, since the ideal Precision value is 1, which is true when there are no false positives.

$$Precision = \frac{TP}{TP + FP} \tag{5.21}$$

- *Recall:* Recall, which is also called the sensitivity, is the ratio is predicted positive outcomes to the sum of true positive and false negative. To achieve a high Recall value, the number of false negatives should decrease.

$$Recall = \frac{TP}{TP + FN} \tag{5.22}$$

- *F1 score:* This metric gives a more accurate measure of the classifier performance, especially in the case when the samples are unevenly distributed. F1 score is the harmonic mean of Precision and Recall. The ideal F1 score is 1.

$$F1score = \frac{2 \times (Precision \times Recall)}{(Precision + Recall)} \tag{5.23}$$

  For the NetRAD data, the classes have an equal number of observations, that is the samples are distributed evenly. So macro-average F1 score (with equal weights) is used, which is the mean of the F1 scores. However, in the case of PARSAX data, the samples are unequally spread across the classes. Thus, a weighted F1 score in terms of attaining an accurate performance metric is employed.

Thus, the four supervised classifiers that will be used are: (a) Linear Discriminant Analysis (LDA), (b) Gaussian Naive Bayes (NB), (c) Fine Decision Tree (DT), and (d) Linear Support Vector Machine (SVM).

### 5.3.3 Fusion Techniques

In an attempt to boost the classification performance, different approaches for combining the data from the 3 nodes (in the NetRAD dataset), and 4 polarimetric channels (in the PARSAX dataset) are investigated. The three types of fusions that are explored are: (a) Decision fusion, (b) Feature fusion, and (c) Ensemble fusion.

#### Decision Fusion

Decision fusion is a technique which takes place after the classification phase, wherein the many classifiers' judgements are assimilated and incorporated into a single outcome [43] [44]. The decision fusion combines the three radar nodes 1, 2, 3 independently as if they were separate simultaneous measurements. Likewise, for the PARSAX data, the four polarimetric channels are fused separately with the assumption of being different simultaneous measurements. Two types of decision fusion are proposed. In this report, the two types of decision fusions will be termed as Fusion 1 and Fusion 2.

| True Class | | Class A (Predicted) | Class B (Predicted) | Class C (Predicted) | | True Class | | Class A (Predicted) | Class B (Predicted) | Class C (Predicted) | | True Class | | Class A (Predicted) | Class B (Predicted) | Class C (Predicted) |
|---|---|---|---|---|---|---|---|---|---|---|---|---|---|---|---|---|
| | Class A | a | b | c | | | Class A | r | s | t | | | Class A | ar | bs | ct |
| | Class B | d | e | f | x | | Class B | u | v | w | = | | Class B | du | ev | fw |
| | Class C | g | h | i | | | Class C | x | y | z | | | Class C | gx | hy | iz |

**'Node P' LDA Classifier Confusion Matrix** — **'Node Q' LDA Classifier Confusion Matrix** — **Resultant Confusion Matrix**

Table 5.7: Mechanism of Decision Fusion 1 by imposing same classifier (here, LDA classifier) on each node or channel

- *Fusion 1- same classifier, different node:* In the first type, a specific model of classifier (from LDA, NB, DT and linear SVM) is imposed on all the nodes or polarization channels. Then, the final performance metric is calculated by elementwise multiplication of the confusion matrices of individual nodes (NetRAD) or polarimetric channels (PARSAX). The Figure 5.7 shows the generalized (3 x 3) confusion matrix with classes A, B, C and radar nodes $P$ and $Q$. An LDA classifier (as an example) is imposed on all the two nodes/ channels, thus, the confusion matrix of LDA classifier from $Node\ P$ is multiplied to the LDA classifier of $Node\ Q$, and the product is the resultant confusion matrix, on which the performance metrics are calculated. The same strategy is followed for the other classifiers as well. The objective here is to increase the density of the diagonal matrix (indicated in green), so that the classification performance also increases.

| True Class | | Class A (Predicted) | Class B (Predicted) | Class C (Predicted) | | True Class | | Class A (Predicted) | Class B (Predicted) | Class C (Predicted) | | True Class | | Class A (Predicted) | Class B (Predicted) | Class C (Predicted) |
|---|---|---|---|---|---|---|---|---|---|---|---|---|---|---|---|---|
| | Class A | a | b | c | | | Class A | r | s | t | | | Class A | ar | bs | ct |
| | Class B | d | e | f | x | | Class B | u | v | w | = | | Class B | du | ev | fw |
| | Class C | g | h | i | | | Class C | x | y | z | | | Class C | gx | hy | iz |

**'Node P' Best Classifier Confusion Matrix** — **'Node Q' Best Classifier Confusion Matrix** — **Resultant Confusion Matrix**

Table 5.8: Mechanism of Decision Fusion 2 by selecting Best classifier from each node or channel

- *Fusion 2- different classifier, different node:* In the second type of decision fusion, the best classifier from each of the nodes or polarizations is selected, and the resulting confusion matrices are fused to get the performance metrics. The best classifier may or may not always be the same at each node, and is bound to vary for different scenarios (hovering, flying, rectangular waypoints) and parameters (dwell time, window duration of spectrogram). To provide an example, the Figure 5.8 is again a generic (3 x 3) confusion matrix consisting of A, B and C as classes and $P$ and $Q$ as radar nodes. Unlike decision Fusion 1, a particular classifier is not applied on the nodes, whereas, the classifier which performed best at that particular node is chosen. So in this case, the best classifiers from $Node\ P$ and $Node\ Q$ are taken and multiplied elementwise to obtain the resultant confusion matrix, and the accuracy, F1 score, and other performance metrics are evaluated. The advantage of this fusion is since only the best classifier is chosen, the possibility to have the null value in the diagonal of the confusion matrix is minimal, and hence, results eventually in enhanced classification performance.

**Feature Fusion**

In this fusion, the significant and most contributing features are selected for application of the fusion technique. The first step in feature fusion is Feature Selection (FS). Feature selection is the method of finding and choosing the most relevant feature(s) from a set of extracted features (obtained through feature extraction). The objective in feature selection is to find an optimal subset that consists of a fewer number of features that improve the performance of classification. This can be achieved by eliminating the correlated redundant feature and selecting the features that are relevant, discriminative and easier to extract.

The filter and the wrapper are the two major techniques to choose the optimum subset from the main set of data. T-test, Battacharya and Euclidean distances, as well as other information metrics. are used to determine the significance of features based on the scores in the Filter method. The wrapper technique undertakes a brute force approach in order to identify which collection of parameters (features) delivers the ideal classification result. Unlike the filter method which is unperturbed by the choice of classifier, the wrapper method on the other hand selects the optimal combination of features based on the classifier. Due to lesser computational complexity, Sequential Forward Selection (SFS) and Sequential Backward Elimination (SBE) are employed. In SFS, the features are inserted progressively to the initial blank set, when the performance seems to diminish, no more features are added to the set. The SBE works inverse to SFS, where the initial set contains all the features. The features are progressively removed until the accuracy begins to diminish [45].

The Sequential Forward Selection (SFS) algorithm is implemented in this thesis since it is a simpler and straightforward technique. In this feature selection process, out of the total set of features, more important features are selected from each of the nodes or polarimetric channels, after which the samples from the union of these features are merged. In feature fusion, the features that are generated from feature selection are combined. The coalition of selected features from the complete collection of features are given as input to the supervised classifiers. The classifiers process these samples and provide the classification metrics.

**Ensemble Fusion**

| True Class | | A | B | C |
|---|---|---|---|---|
| | A | w1 | w2 | w3 |
| | B | w4 | w5 | w6 |
| | C | w7 | w8 | w9 |
| | | **Predicted Class** | | |

**'Node P' LDA Confusion Matrix**

**x**

| True Class | | A | B | C |
|---|---|---|---|---|
| | A | x1 | x2 | x3 |
| | B | x4 | x5 | x6 |
| | C | x7 | x8 | x9 |
| | | **Predicted Class** | | |

**'Node P' NB Confusion Matrix**

**x**

| True Class | | A | B | C |
|---|---|---|---|---|
| | A | y1 | y2 | y3 |
| | B | y4 | y5 | y6 |
| | C | y7 | y8 | y9 |
| | | **Predicted Class** | | |

**'Node P' DT Confusion Matrix**

**x**

| True Class | | A | B | C |
|---|---|---|---|---|
| | A | z1 | z2 | z3 |
| | B | z4 | z5 | z6 |
| | C | z7 | z8 | z9 |
| | | **Predicted Class** | | |

**'Node P' SVM Confusion Matrix**

Table 5.9: Mechanism of Ensemble Fusion where different classifiers are applied on same node; used for polarimetric features

The ensemble fusion is different from decision fusion in the way that this method operates on one node by fusing the confusion matrices of all the classifiers applied to the data of that node. The technique of ensemble fusion (which is basically *same node, different classifiers*) is particularly ideal for the polarimetric features, where an ensemble of classifiers is used to enhance the classification performance. Since the features from all polarimetric channels are combined as a single block as seen in Table 5.3, the possibility to apply Fusion 1 and Fusion 2 is ruled out. The ensemble fusion involves all the classifiers to come into play, as shown in 5.9. Similarly here, a (3x3) confusion matrix with A, B and C classes are considered for $Node\ P$ with LDA, NB, DT and SVM classifiers. By fusing through an ensemble of classifiers, the confusion matrices of the independent classifiers (LDA, NB, Decision Tree, Linear SVM) are multiplied elementwise. The classification metrics of the resultant product are assessed to analyze the improvement in the accuracy.

## 5.4 Conclusion

In this chapter, the main research methodology from Figure 5.11 is covered. The algorithms involve generating spectrogram, extracting suitable features, followed by supervised classification and increasing the performance using fusion. The yellow-coloured blocks indicate the novel techniques developed in the research methodology for this thesis' objectives in the research methodology. Some of the highlights are:

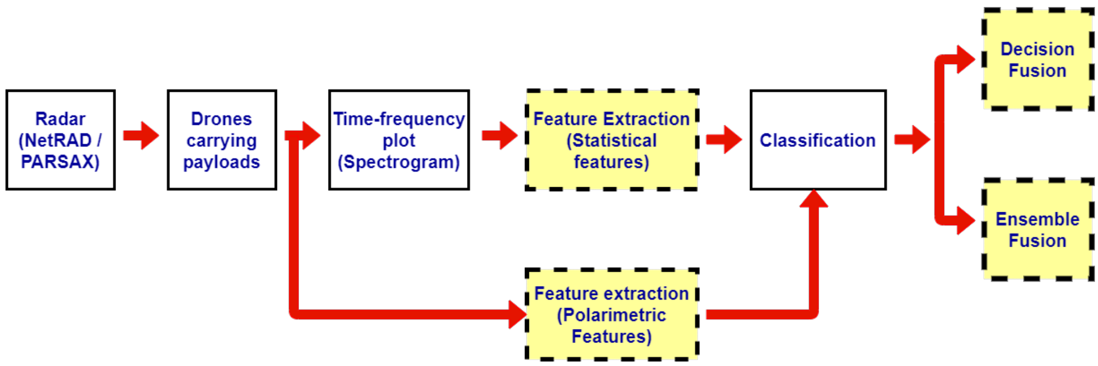


Figure 5.11: Flow chart of Research methodology, with main contribution blocks highlighted in yellow blocks

- The spectrogram clearly indicates the finer micro-Doppler specifics of the blade rotations. The blade flashes become straighter for the increase in payload weight. The spectrogram is continuous for NetRAD data, whereas the PARSAX data has intermittent spectrogram due to the drones deviating from the radar beam.
- The two sets of features are: Statistical and Polarimetric. After feature extraction, the samples are equally distributed for the NetRAD data, on the other hand, for the PARSAX data, unequal sample distribution per class is obtained due to discontinuity in the spectrogram.
- Multiclass classification problem is opted for both the datasets. The 5 classes in the NetRAD data are 0g, 200g, 300g,400g and 500g. The PARSAX data has 4 classes, Quadcopter M200/0kg, Quadcopter M200/1kg, Hexacopter M600/0kg and Hexacopter M600/2.35kg.
- The four supervised classifiers: LDA, Gaussian NB, Decision Tree and Linear SVM are considered based on the classification accuracy and the computational complexity.
- For enhancing the classification performance, feature fusion and decision fusion techniques are used for the statistical features. In the case of polarimetric features, an ensemble of classifiers is employed since the features from all polarimetric channels are tied together as a single block.

# Chapter 6

# Results and Observations

*In this chapter, the two types of fusion on statistical features, namely, the feature and decision fusions are analyzed initially to assess which technique outperforms the other. Thereafter, the results of classification performances for the two sets of data, from NetRAD and PARSAX are investigated, and observations are made on the parametric analysis for the different scenarios. The parameters of interest are (a) Varying dwell time, (b) Varying window duration of the spectrograms, (c) Adding noise to vary the SNR of the spectrograms.*

*As mentioned previously, the drones follow multiple trajectories, referred to as 'scenarios'. For the NetRAD dataset, the scenarios are (a) drone hovering and (b) drone flying. On the other hand, the scenarios for the PARSAX dataset are (a) drones hovering, (b) drones flying, (c) drones moving in rectangular waypoints, and (d) combined scenario of drones flying and moving in waypoints. The classification performance of the individual nodes or polarimetric channels is evaluated for the different parameters. The fusion techniques on the statistical and polarimetric features are also incorporated to observe the change in performance in comparison to the independent nodes or channels.*

*The factors on which the observations depend are the datasets, the scenario considered, and how the classifiers perform. So, the results vary from one scenario to another, and may not always be constant even for the same scenarios of two different datasets.*

## 6.1 Fusion Results: Decision Fusion and Feature Fusion

The results of the decision fusion (Fusion 1 and Fusion 2) and feature fusion are discussed, and a comparison is made on the better fusion between the two techniques. The decision Fusion 1 involves assigning the same specific classifier on all the nodes or channels; whereas decision Fusion 2 selects the best classifier from each node or channel for analysis. The feature fusion operates at the feature phase, on the contrary, the decision fusion is applied after the classification phase.

### 6.1.1 Decision Fusion

The Table 6.1 represents the confusion matrices for the Fusion 1 technique. The NetRAD dataset for the scenario of drone flying is taken, and the LDA classifier is assigned for all the nodes 1, 2 and 3. Here, the LDA classifier is taken as an example to illustrate the mechanism of Fusion 1 technique, and the same procedure is followed for other classifiers also. The product of these confusion matrices is represented as resultant confusion matrix, which has most of the samples concentrated in its diagonal. The aim is to increase the density of the diagonal matrix, such that it is sufficiently populated to show improvement in accuracy. In this way, the possibility for the other cells of the matrix to nullify (as seen in Tables 6.1

and 6.2) also increases. On the contrary, in case if the diagonal matrix of one of the nodes contains huge misclassification, this will result in the classification performance to reduce upon fusion. In this case of drone flying, the Fusion 1 has benefitted in achieving the target of increased classification accuracy.

| True Class \ Predicted Class | 0g | 200g | 300g | 400g | 500g |
|---|---|---|---|---|---|
| 0g | 4 | 0 | 1 | 0 | 1 |
| 200g | 3 | 1 | 0 | 0 | 2 |
| 300g | 0 | 1 | 3 | 2 | 0 |
| 400g | 1 | 1 | 1 | 2 | 1 |
| 500g | 0 | 0 | 4 | 0 | 2 |

**LDA Node 1**

x

| True Class \ Predicted Class | 0g | 200g | 300g | 400g | 500g |
|---|---|---|---|---|---|
| 0g | 6 | 0 | 0 | 0 | 0 |
| 200g | 3 | 2 | 1 | 0 | 0 |
| 300g | 0 | 2 | 1 | 0 | 3 |
| 400g | 0 | 2 | 2 | 1 | 1 |
| 500g | 0 | 1 | 1 | 1 | 3 |

**LDA Node 2**

x

| True Class \ Predicted Class | 0g | 200g | 300g | 400g | 500g |
|---|---|---|---|---|---|
| 0g | 4 | 1 | 0 | 1 | 0 |
| 200g | 3 | 2 | 0 | 0 | 1 |
| 300g | 1 | 0 | 4 | 0 | 1 |
| 400g | 1 | 0 | 0 | 2 | 3 |
| 500g | 0 | 0 | 1 | 2 | 3 |

**LDA Node 3**

| True Class \ Predicted Class | 0g | 200g | 300g | 400g | 500g |
|---|---|---|---|---|---|
| 0g | 96 | 0 | 0 | 0 | 0 |
| 200g | 27 | 4 | 0 | 0 | 0 |
| 300g | 0 | 0 | 12 | 0 | 0 |
| 400g | 0 | 0 | 0 | 4 | 3 |
| 500g | 0 | 0 | 4 | 0 | 18 |

**Resultant Confusion Matrix**

Table 6.1: Decision Fusion 1 of LDA classifier for Drone flying: NetRAD data

In the second type of decision Fusion 2, the best classifier from each of the nodes is selected, and the resulting confusion matrices are fused to get the performance metrics. The Table 6.2 is again for the case of NetRAD data for drone flying. But this time, out of the four classifiers, the one that resulted in the highest accuracy is chosen from every node. In this case, for Node 1, the LDA classifier performed well, whereas, for Nodes 2 and 3, the SVM classifier secured the maximum results. Their corresponding confusion matrices are multiplied for the evaluation of accuracy. It is evident that the diagonal of the resultant matrix is richly populated, making most of the other cells to be 0, leading to lesser misclassification. Thus, the classification performance is improved.

| True Class \ Predicted Class | 0g | 200g | 300g | 400g | 500g |
|---|---|---|---|---|---|
| 0g | 4 | 0 | 1 | 0 | 1 |
| 200g | 3 | 1 | 0 | 0 | 2 |
| 300g | 0 | 1 | 3 | 2 | 0 |
| 400g | 1 | 1 | 1 | 2 | 1 |
| 500g | 0 | 0 | 4 | 0 | 2 |

**LDA Node 1**

x

| True Class \ Predicted Class | 0g | 200g | 300g | 400g | 500g |
|---|---|---|---|---|---|
| 0g | 6 | 0 | 0 | 0 | 0 |
| 200g | 1 | 4 | 1 | 0 | 0 |
| 300g | 0 | 3 | 2 | 0 | 1 |
| 400g | 0 | 1 | 2 | 2 | 1 |
| 500g | 0 | 1 | 2 | 1 | 2 |

**SVM Node 2**

x

| True Class \ Predicted Class | 0g | 200g | 300g | 400g | 500g |
|---|---|---|---|---|---|
| 0g | 4 | 2 | 0 | 0 | 0 |
| 200g | 0 | 6 | 0 | 0 | 1 |
| 300g | 1 | 0 | 4 | 0 | 1 |
| 400g | 1 | 1 | 0 | 2 | 2 |
| 500g | 0 | 0 | 2 | 1 | 3 |

**SVM Node 3**

| True Class \ Predicted Class | 0g | 200g | 300g | 400g | 500g |
|---|---|---|---|---|---|
| 0g | 96 | 0 | 0 | 0 | 0 |
| 200g | 0 | 24 | 0 | 0 | 0 |
| 300g | 0 | 0 | 24 | 0 | 0 |
| 400g | 0 | 1 | 0 | 8 | 2 |
| 500g | 0 | 0 | 16 | 0 | 12 |

**Resultant Confusion Matrix**

Table 6.2: Decision Fusion 2 of best classifier for Drone flying: NetRAD data

### 6.1.2 Feature Fusion

| Node 1 | Node 2 | Node 3 |
|---|---|---|
| Mean of the diagonal matrix | Mean of the diagonal matrix | Mean of the diagonal matrix |
| SD of the diagonal matrix | Kurtosis of the diagonal matrix | SD of the diagonal matrix |
| Kurtosis of the diagonal matrix | Mean of the centroid | Kurtosis of the diagonal matrix |
| Mean of the centroid | Mean of bandwidth | Mean of the centroid |
| | | SD of the centroid |

Table 6.3: Features selected from the Nodes 1, 2 and 3 for Drone hovering without payload: NetRAD data

As a part of feature selection, the Sequential Forward Selection (SFS) algorithm is implemented initially on the NetRAD dataset for the scenario of drone hovering. The Table 6.3 represents the collection of suitable features individually from Nodes 1, 2 and 3. The combined set contains 6 out of the total 12 features. The union of these selected features are used for further evaluation by feature fusion. The classifiers are trained on the 80% training set with 5-fold CV and tested on the 20% of samples to calculate the classification performance in Table 6.4. A comparison is made on the feature and decision fusions to evaluate which technique is more suitable and performs optimally on the datasets.

| Dwell Time 1s | | | | | |
|---|---|---|---|---|---|
| **Classifier** | **Node 1** | **Node 2** | **Node 3** | **Feature Fusion** | **Decision Fusion** |
| **LDA** | 0.93 | 0.93 | 0.97 | 0.57 | 1.00 |
| **Naive bayes** | 0.83 | 0.75 | 0.89 | 0.58 | 1.00 |
| **Decision Tree** | 0.86 | 0.71 | 0.87 | 0.78 | 1.00 |
| **Linear SVM** | 0.97 | 0.93 | 0.93 | 0.64 | 1.00 |

Table 6.4: F1 scores of Feature fusion and Decision Fusion of nodes from NetRAD data for Drone hovering without payload

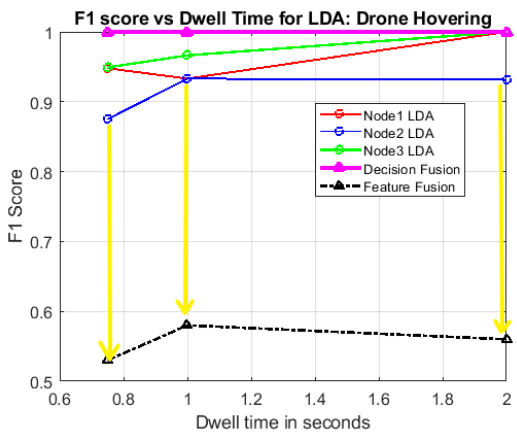


Figure 6.1: F1 scores VS Dwell Time of Feature fusion and Decision fusion 1 result of LDA classifier for Drone hovering with 0g payload: NetRAD data

The Table 6.4 gives information about the F1 score of independent nodes, and their fusion via feature and decision (here, Fusion 1) fusions. It is transparent that feature fusion does not contribute to the improvement in performance, but rather counteracts the accuracy by providing accuracies lesser than the individual nodes for all the classifiers. In an ideal case, the accuracy would increase with an increase in the number of features, and after the cut-off value is reached, the classification starts to depreciate due to an overload of features. In this scenario of drones with payloads, the poor performance is believed to be related to differences in the micro-Doppler signatures for different nodes. Consequently, the samples from feature extraction also vary as the data from each radar node is different due to the difference in aspect angle. Thus, when the union of these approximately disjoint features are provided to the classifiers, the performance is disrupted due to their inability to distinguish the classes.

The Figure 6.1 (F1 score VS dwell time for LDA classifier) graphically represents the loss of performance metric (F1 score) when features are combined, which indicates that feature fusion is not an ideal technique in this situation. However, decision fusion presents a significant enhancement in performance. The decision fusion takes place after the classification phase, so there is no indulgence with the spectrogram or the aspect angles in this type of fusion.

Therefore, as feature fusion has a negative effect on the performance for these kinds of datasets (where aspect angles are involved), moving forward, only the two types of decision fusions will be evaluated for the parametric analyses of the NetRAD and PARSAX datasets.

## 6.2 UCL: NetRAD Radar Results

Firstly, the data from NetRAD radar is considered. The performance metrics of the individual nodes of the NetRAD radar are calculated for the three said parameters (varying dwell time, varying spectrogram window duration, and adding noise to vary the SNR of the spectrogram) at each instance, and inferences are obtained for analyses. In the case of NetRAD data, There are 5 classes of payloads (0g, 200g, 300g, 400g and 500g), each of them with an equal number of samples. So mathematically, for a classifier to have a good performance, it should have an accuracy of at least 20% (since the probability of randomly selecting 1 out of 5 is 0.2) even though for practical usage, a much higher accuracy is required. Based on the classification performance, some observations are drawn for the various parameters for the scenarios of (a) drone flying and (b) drone hovering.

### 6.2.1 Drone Flying

The first scenario is drone flying back and forth and the performance of independent nodes and their fusion results are discussed for all the parameters.

#### Varying Dwell Time

In the scenario for drone flying, the dwell time is varied from 0.5s, 0.75s, 1s, 1.5s and 2s, in order to deduce a pattern in the accuracy for the different duration of spectrogram splits. From the plots of the four classifiers, it can be seen that a smaller value of spectrogram split duration is favoured in the classifiers. By micro-analyzing it at every instance, the classification performance is high at 0.5s in all the classifiers, then takes a dip at 0.75s and 1s, and again goes on to increase slightly. However, in principle, a shorter dwell time is desirable, since it also highlights the radar's ability to detect and distinguish among the targets at a faster time. Also, with the increase in dwell time, the number of samples reduces (Table 5.4). As a result, the classifiers have fewer data points (samples) to learn from, thus resulting in poorer classification. For the dwell time of 0.5s, the classification performance is of the range approximately 38% to 53% for the individual Nodes 1, 2 and 3. It can be inferred that the classifier is able to classify up to 2 or 3 classes.

So, in order to improve the classification performance, the 2 types of fusion (as discussed before) are performed. The Fusion 1 has the particular classifier assigned at each node, whereas in Fusion 2, the best classifier is different at different dwell times. Both the decision fusions have resulted in enhanced results, and in comparison, the Fusion 2 (black line - best classifier at each node) has performed better than Fusion 1 (pink line - fixed classifier at each node). The classification performance has increased up to 89% to 96% at 0.5s, implying that the classifier is able to distinguish 4 out of 5 classes successfully upon fusion.

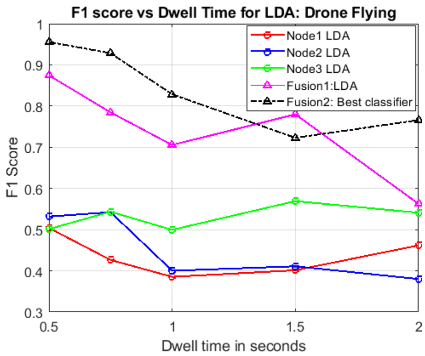


(a) Linear Discriminant Analysis Classifier

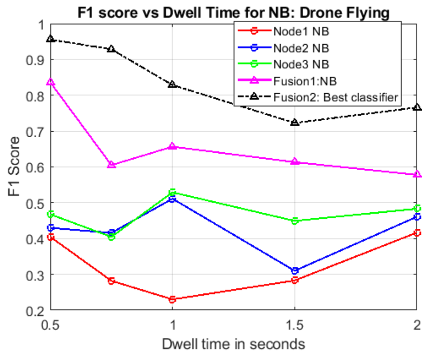


(b) Gaussian Naive Bayes Classifier

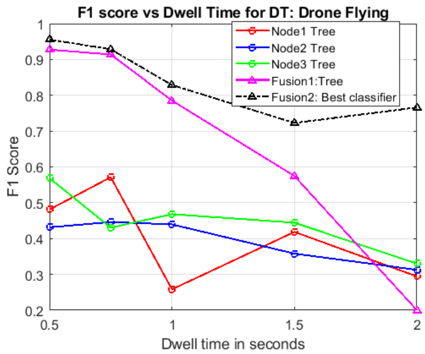


(c) Fine Decision Tree Classifier

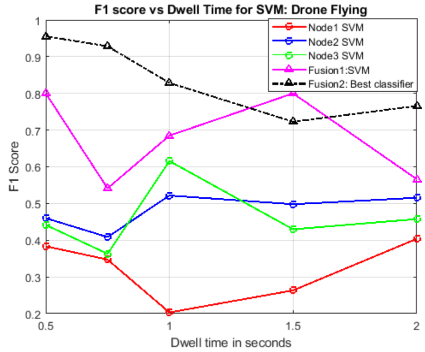


(d) Linear Support Vector Machine Classifier

Figure 6.2: NetRAD data: Classification performance of classifiers as F1 score vs spectrogram split duration (i.e. dwell time): Drone Flying

### Varying Spectrogram Window Duration

The next parameter is varying the spectrogram window duration. The trade-off exists in time and frequency domains for variations in durations of the spectrogram window as discussed in Figure 5.3 of Chapter 5. In Figure 6.3, the dimensions have changed from (1000x12480) to (8000x1481) in (Doppler x Time) for the spectrogram window durations from 0.05 to 0.4s respectively. The frequency is blurred in (a), where as in (b), the time axis is blurred, corresponding to worse Doppler resolution in the former (Figure 6.3a) and worse time resolution in the latter (Figure 6.3b).

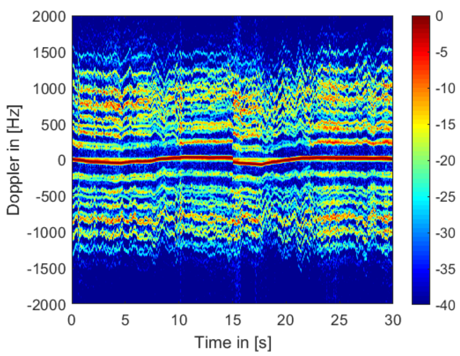


(a) Spectrogram for Drone flying with 0g when spectrogram window duration is 0.05s

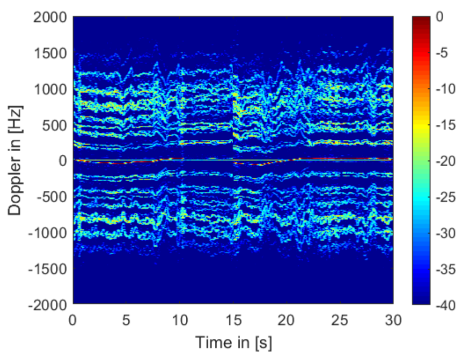


(b) Spectrogram for Drone flying with 0g when spectrogram window duration is 0.4s

Figure 6.3: NetRAD data: Spectrogram for Drone flying with 0g when spectrogram window duration is changed from 0.05s to 0.4s

For varying the spectrogram window duration from 0.05s, 0.1s, 0.25s and 0.4s, the individual Nodes 1, 2 and 3 have a performance of F1 score in the range of 36% to 56%. So again, the classifier is able to classify atmost 3 classes at the individual nodes. So, again by the two types of decision fusions, the performance has increased considerable well, reaching a value of up to 91%, thus resulting in the hike in the classifier's ability to distinguish 4 or approximately 5 classes. The enhancement in classification performance by the two fusions has proved to be beneficial. The Fusion 1, though has a performance little lesser than Fusion 2, however, it has shown an increased accuracy at most instances. On the other hand, as seen in Figure 6.4, Fusion 2 has largely outperformed Fusion 1.

To ascertain the ideal window duration, from the plots, it is visible that most classifiers perform better for the window sizes of 0.05s and 0.1s. So, out of the two, a shorter duration of spectrogram window is favourable for the drone flying. For the spectrogram window durations from 0.25s and 0.4s, the performance goes down. The resolution in time diminishes with an increase in window duration, so the important components in the features are possibly lost, which can be the reason for the decline in accuracy at longer spectrogram window durations.

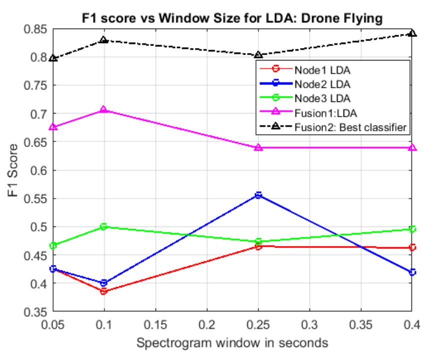


(a) Linear Discriminant Analysis Classifier

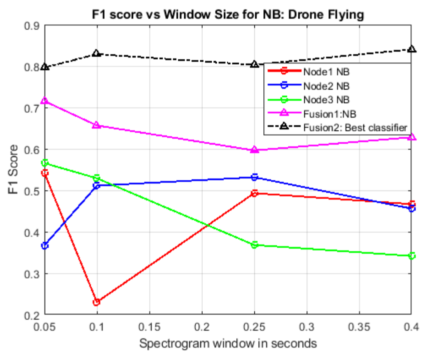


(b) Gaussian Naive Bayes Classifier

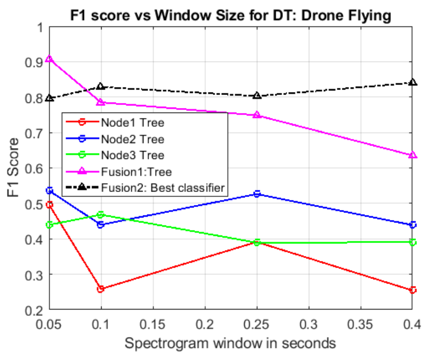


(c) Fine Decision Tree Classifier

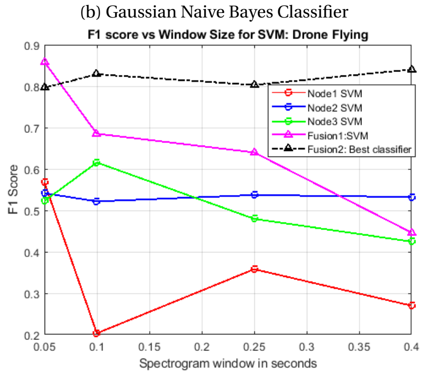


(d) Linear Support Vector Machine Classifier

Figure 6.4: NetRAD data: Classification performance of classifiers as F1 score vs spectrogram window duration: Drone Flying

### Adding Noise to Vary SNR

The third parameter is adding noise of varying SNRs. After the RTI plots are generated, noise to generate an equivalent SNR of 2dB, 5dB, 8dB, 10dB, 15dB, 25dB are added to the RTI plots, before calculating the STFT. Figure 6.5 depicts the variation in the blade flashes and main body of the drone for the SNR of 2dB, 10dB and 25dB.

It is seen that the central red line at 0 Hz, which is the main body of the drone, is visible distinctly regardless of the variation in noise. Since the primary part of the drone is sturdier than the rotor blades, the addition of noise did not majorly affect its presence in the spectrogram. On the other hand, the rotor blades are comparatively flimsy and hence, are covered in noise at lower SNRs. It is observed that Node 2 is upbeat at 2dB SNR when the drone is not carrying any payload, however with an increase in payload weights, the spectrogram is distorted.

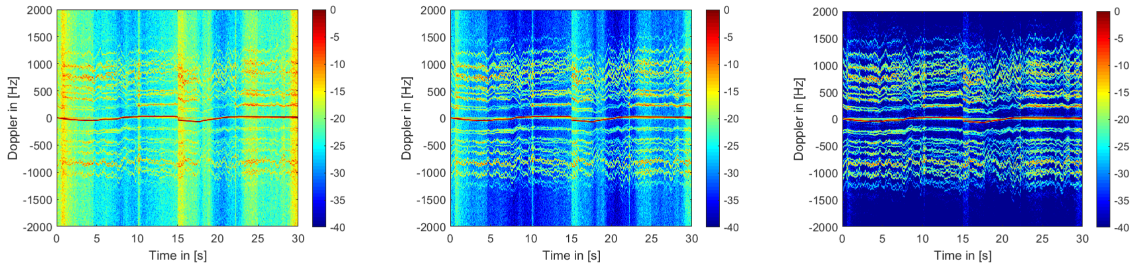


(a) SNR 2 dB (b) SNR 10 dB (c) SNR 25 dB

Figure 6.5: Effect on spectrogram when noise to vary SNR is added: Drone Flying without payload at N1- NetRAD radar. Blade flashes are faint at low SNR

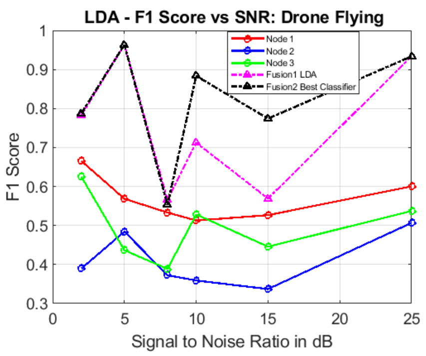


(a) Linear Discriminant Analysis Classifier

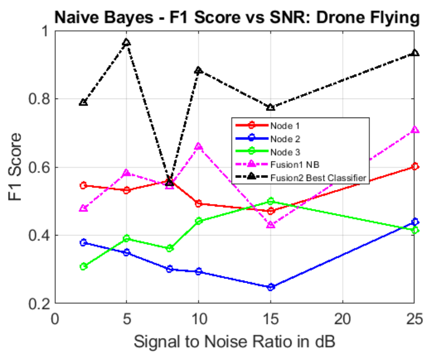


(b) Gaussian Naive Bayes Classifier

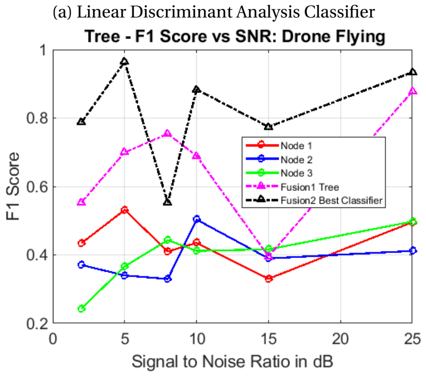


(c) Fine Decision Tree Classifier

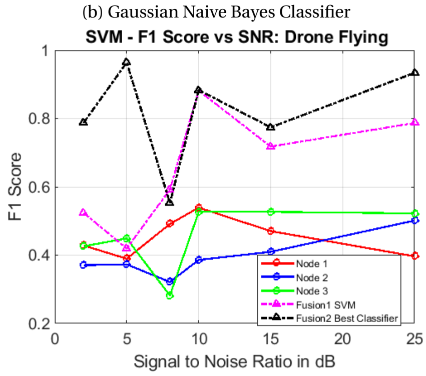


(d) Linear Support Vector Machine Classifier

Figure 6.6: NetRAD data: Classification performance of classifiers as F1 score vs Noise: Drone Flying

The Figure 6.6 represents the plots for SNR versus F1 score for the independent Nodes 1, 2 and 3, along with the Fusion 1 and Fusion 2 results at varying SNRs. It is evident, from theory and from the plots that at lower SNR, the spectrograms consist of a lot of disturbances and artefacts. Since the spectrograms are not decipherable, and the important elements are overlapped by noise, the classification accuracy is poor. As the SNR increases, the significant components in the spectrogram become distinguishable, thus leading to improved classification. All the four supervised classifiers show a similar trend in classification performance, where an increase in F1 score is directly proportional to an increase in SNR. However, it is hard to ascertain a particular SNR as the ideal value at which maximum classification is obtained, since it depends on the base SNR during data collection. However, it can be inferred that the feature extraction technique is robust to additional noise, as it is able to distinguish the classes more or less accurately. The Node N1 has a higher F1 score as far as individual nodes are considered. Furthermore, the two fusion techniques have resulted in overall enhanced classification performance, with Fusion 2 performing better than Fusion 1 in most instances of SNR.

### 6.2.2 Drone Hovering

The drone hovering is likewise subjected to three parametric analyses and subsequent fusion techniques. The Fusion 1 is where a particular classifier is assigned to each node, and the classification performance is evaluated from the resultant confusion matrix, after multiplying the individual confusion matrices. The Fusion 2 is selecting the best classifier at each node and again multiplying the CMs to get one final CM, whose performance metrics are calculated.

#### Varying Dwell Time

The first parametric analysis is the change in how the spectrogram is split (that is, the dwell time) into smaller segments. The initial dwell time is set as 1s and subsequently modified to study the trend in classification performance over the varying dwell time. For the case of drone hovering, the dwell times of 0.5s, 1s, and 2s were considered. Since in the real-life situation for the scenario where the drone is hovering alone is quite uncommon, only a few dwell times were taken into account. In the Figure 6.7, the classification performances of the four classifiers (LDA, NB, DT, Linear SVM) are seen, along with the decision fusion results. From the plots, it is shown that Nodes 1 and 3 have higher classification performance, as a result of how the features were extracted and how well the classifier is able to segregate the samples.

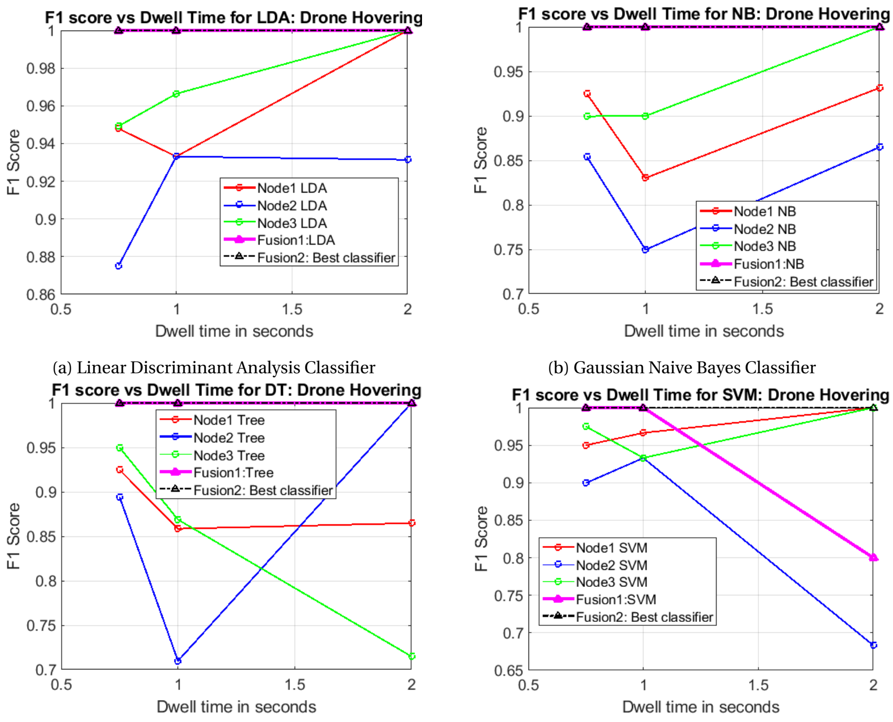


(a) Linear Discriminant Analysis Classifier

(b) Gaussian Naive Bayes Classifier

(c) Fine Decision Tree Classifier

(d) Linear Support Vector Machine Classifier

Figure 6.7: NetRAD data: Classification performance of classifiers as F1 score vs spectrogram split duration (i.e. dwell time): Drone Hovering

Though each of the classifiers depict a variety of interpretations at each instance of dwell time, on the whole from the majority of classifiers, the ideal dwell time is preferred as 0.75s, thus a comparatively shorter dwell time is desirable. Also, theoretically, as the dwell time is increased, the number of samples in each of the classes reduces proportionally as the dataset has a limited size (Table 5.4). Thus, the number of training samples decreases, making it difficult for the classifier to get well trained, and hence resulting in poorer classification.

Moreover, a shorter dwell time is profitable, since the radar is able to detect the target and classify it. An F1 score of approximately 94% to 97% is achieved at Nodes 1 and 3 for the dwell time of 0.75s, whereas for Node 2, it is about 89%. The variation in the F1 score is due to the difference in aspect angle. The other reason is how the samples were spread across in the confusion matrix. For Nodes 1 and 3, the samples were concentrated in the main diagonal matrix, whereas for Node 2, the samples are dispersed. However, the two types of decision fusions proved optimal, since an ideal classification of 100% is attained at each instance of dwell time. Thus, an improvement in the results is witnessed via fusion, even though the individual nodes had previously fairly good accuracy.

**Varying Spectrogram Window Duration**

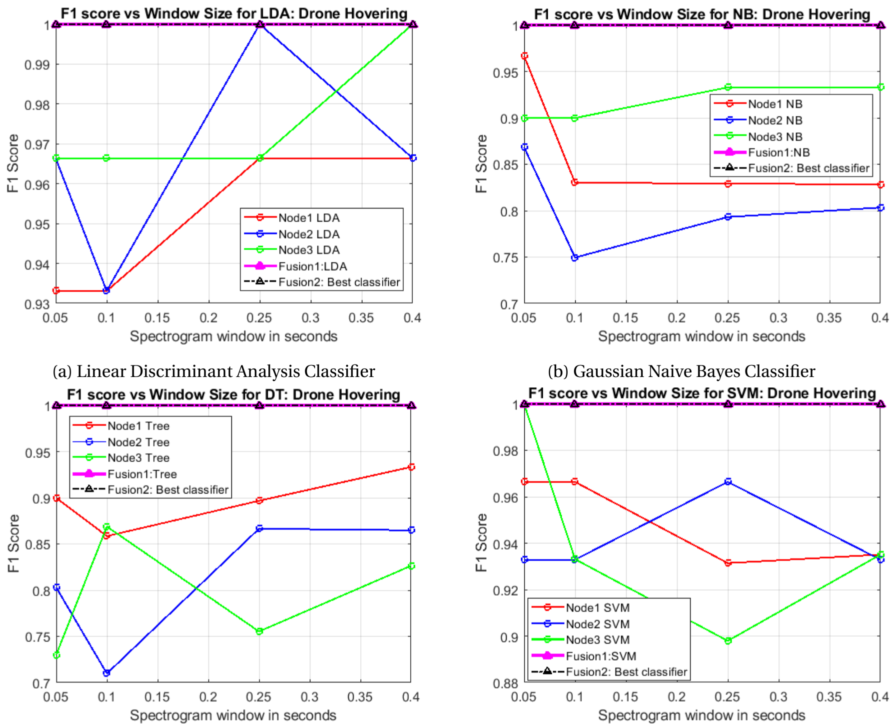


(a) Linear Discriminant Analysis Classifier

(b) Gaussian Naive Bayes Classifier

(c) Fine Decision Tree Classifier

(d) Linear Support Vector Machine Classifier

Figure 6.8: NetRAD data: Classification performance of classifiers as F1 score vs spectrogram window duration: Drone Hovering

The second parameter is the variation in spectrogram window durations in the range 0.05s, 0.1s, 0.25s and 0.4s. From the output of the classifiers in most of the cases, since it fluctuates for different window durations, it is complicated to come to a conclusion which window duration gives the optimum accuracy. At each instance of spectrogram window duration, the performance oscillates from 75% to approximately 95% in most cases, it can be gauged 0.05s shows good accuracy. The classifier in the scenario of drone hovering is already able to distinguish well among classes. For the classifiers Gaussian NB and Linear SVM, the performance drops with an increase in spectrogram window duration, so it can be deduced approximately that a shorter window duration is preferred. It is to be noted that the number of feature samples for classification remains the same, since the way the spectrogram is split is 1s duration throughout this analysis. For the decision fusions, the outcomes were perfect 100% F1 score.

### Adding Noise to Vary SNR

The final parameter is the addition of noise. The noise of SNRs 2dB, 5dB, 8dB, 10dB, 15dB, and 25dB are added to the spectrograms to assess the classification performance. From Figure 6.9, shows the scenario of drone hovering without payload at Node 1. The spectrograms cannot be interpreted at SNR 2 dB and becomes more decipherable at SNR 25 dB. The Figure 6.10 illustrates the plots between SNR and F1 scores for different classifiers. It can be seen that in terms of individual nodes, Node 1 has better performance in most cases. The variation in F1 scores of the independent nodes is due to differences in their aspect angles. The samples after feature extraction contain more noise components at lowers SNRs, which resulted in the performance to depreciate. However, the feature extraction via SVD, centroid and BW is ascertained to be beneficial, since the minimum classification obtained is 60% (at 2dB for DT classifier in 6.10 (c)), which implies that the classifier is able to discriminate up to 3 classes even in the presence of noise. Additionally, the Fusion 1 and Fusion 2 techniques have surpassed the performance of individual classifiers, by reaching an ideal F1 score of almost 100%.

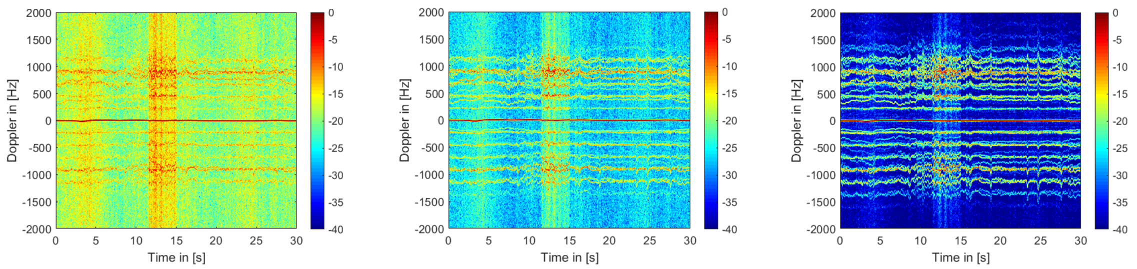


(a) SNR 2 dB (b) SNR 10 dB (c) SNR 25 dB

Figure 6.9: NetRAD data: Effect on spectrogram when noise to vary SNR is added: Drone Hovering without payload at N1- Faint blade flashes at low SNR

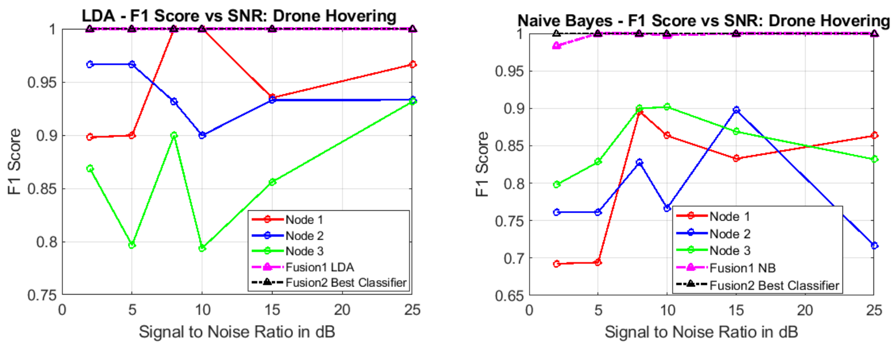


(a) Linear Discriminant Analysis Classifier (b) Gaussian Naive Bayes Classifier

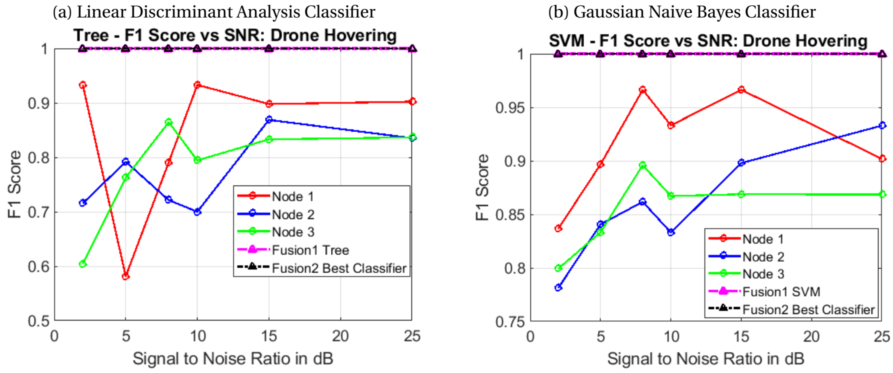


(c) Fine Decision Tree Classifier (d) Linear Support Vector Machine Classifier

Figure 6.10: NetRAD data: Classification performance of classifiers as F1 score vs Noise: Drone Hovering

## 6.3 TU Delft: PARSAX Radar Results

Similarly, just as in the case of NetRAD data, the performance metrics of the individual polarizations of PARSAX dataset are computed here. The same set of parameters are taken, that is, dwell time, spectrogram window duration and noise. The spectrogram is split for durations 0.5s, 1s and 1.5s; the spectrogram window is varied from 0.05s, 0.1s and 0.25s duration; and finally, additional noise is added for SNRs 2 dB, 5 dB, 8 dB, 10 dB, 15 dB and 25 dB, until a pattern in classification performance is attained for the parameters.

The four classes are the M200 quadcopter carrying 0kg and 1kg, and M600 hexacopter carrying 0kg and 2.35kg. Since the spectrogram is not continuous and there are multiple measurements for the same scenario, the number of samples is different for each of the classes. In this case, the minimum classification performance for a classifier is at least 25% (since there are 4 classes and selection 1 out of 4 is 0.25). Although this cannot be the exact assumption since the samples are distributed unevenly, it helps in gaining a broader overview of the classification performance. It is observed that the HH polarization produced the highest classification accuracy in all parametric analyses, and also in most of the individual instances of each analysis, as far as separate polarizations are considered. The classification performances of the 4 scenarios from the PARSAX dataset are discussed.

### 6.3.1 Drone Flying

The first scenario is the drones flying and their corresponding parametric analyses are illustrated in Figure 6.11. The two types of decision fusion, that is, Fusion 1 and Fusion 2 are indicated by the black and cyan coloured lines.

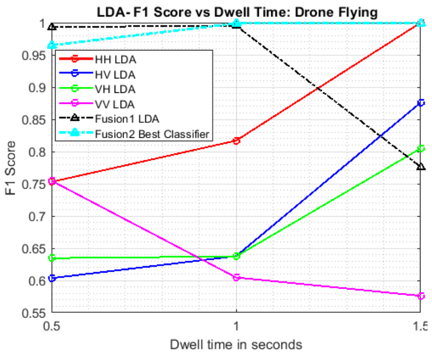


(a) F1 score VS Dwell time- Linear Discriminant Analysis Classifier

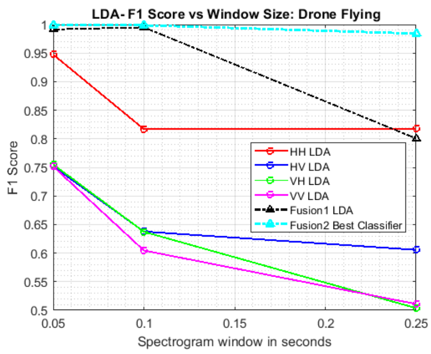


(b) F1 score VS Spectrogram Window Duration- Linear Discriminant Analysis Classifier

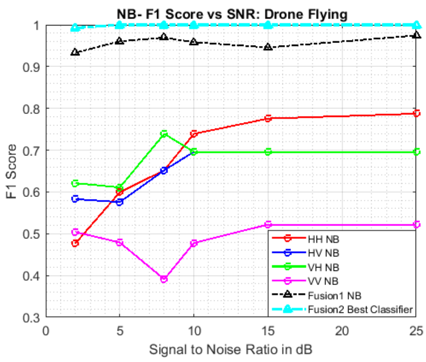


(c) F1 score VS SNR- Gaussian Naive Bayes Classifier

Figure 6.11: PARSAX data: Classification performance of classifiers as F1 score vs Parameters (a)Dwell Time; (b) Spectrogram window duration; (c) Noise: Drones Flying

| Type | No Normalization | | | | Min-Max Normalization | | | |
|---|---|---|---|---|---|---|---|---|
| **Classifier** | **HH** | **HV** | **VH** | **VV** | **HH** | **HV** | **VH** | **VV** |
| **LDA** | 82.6 | 65.2 | 65.2 | 60.9 | 73.6 | 47.8 | 52.2 | 52.2 |
| **Naive Bayes** | 82.6 | 73.9 | 73.9 | 56.5 | 60.9 | 60.9 | 43.5 | 34.8 |
| **Decision Tree** | 82.6 | 87.0 | 78.3 | 78.3 | 34.9 | 47.8 | 47.8 | 56.5 |
| **Linear SVM** | 87.0 | 69.6 | 69.6 | 65.2 | 69.6 | 52.2 | 43.5 | 47.8 |

Table 6.5: PARSAX data: Comparison of classification performance (Accuracy percentage) at dwell time 1s: With and without min-max normlization on the samples after feature extraction

For the case of drones flying, the results for the Linear Discriminant Classifier (LDA) are represented in Figure 6.11 (a)-(b) for the change in dwell time and spectrogram window duration respectively, and Figure 6.11(c) exhibits a Gaussian NB classifier for the parameter of additional noise. A similar trend in variation is observed for the other classifiers, and hence these plots are presented as their depictions.

The Table 6.5 shows the accuracy as a percentage of classification when no normalization or standardization is applied and when Min-Max normalization is applied to the samples derived after feature extraction. By normalizing the samples in the range [0,1], the classifier did not perform well in many cases, so for further analyses, only the non-normalized values are used for classification purposes.

- *Dwell Time:* Firstly, from the classification performance in this scenario, the ideal dwell time is 1 to 1.5s since a better accuracy value is achieved. For the case of VV polarization alone, the performance degrades with an increase in accuracy, whereas for the other polarizations VH, HV and HH, 1s - 1.5s spectrogram split duration produced a better accuracy. The HH polarization has an accuracy of almost 100% at 1.5s, which indicates that an increase in dwell time beyond this value would substantially cause a minimal difference in performance. However, the classifier's performance is expected to deteriorate past a specific spectrogram split duration, since theoretically as well, when the dwell time is increased, the number of samples in each of the classes reduces proportionally as the dataset has a limited size. Thus, as mentioned previously, a shorter dwell time is more often preferred. The Fusion 1 and Fusion 2 (black and cyan lines respectively) have a positive effect on the performance, attaining a maximum of 100% overall for all the instances of dwell time. It is observed that the Fusion 1 resulted in a reduced performance at 1.5s, even lesser than the individual polarizations HH, HV and VH. This is because, as seen, the VV performance has an approximately 60% F1 score, the LDA classifier has misclassified the quadcopter M200 0kg class, thus leading to the dominant diagonal matrix to be scattered, and hence the lower accuracy. Due to this misclassification of a particular class, the fusion of all the polarizations lowered the overall performance. So, in this case, fusion can also impair accuracy.
- *Spectrogram Window Duration:* Secondly, in the analysis of varying the spectrogram window duration, the observations were made for 0.05s, 0.1s and 0.25s. By sliding the window through these values, it is observed that the classification performance has diminished. Classification accuracy of about 95% is attained for HH polarization at spectrogram window of 0.05s. The VV and VH polarizations are relatively low in performance at 0.25s due to incorrect predictions, thus the Fusion 1 is not able to produce an enhanced value at that instance. However, in other instances, there is considerable improvement in the accuracy. The depreciating performance is due to worsening of resolution in time, thus, when window duration is extended, and critical components in feature extraction may get distributed across multiple spectrogram window duration. The Fusion 2 is not concentrated to LDA classifier alone, since it designates the best classifier at each polarization, the results obtained are mostly very optimum in all the scenarios.
- *Noise:* Thirdly, analyzing the impact of noise, the analogy can be interpreted as the lower the SNR, weaker the classification performance. In an ideal situation, the classification performs well when

the SNR is increased, and the plot is practically almost linear up to a point and saturates before becoming relatively stable for F1 score VS SNR. A similar pattern is witnessed in this case. The accuracy is lower at SNRs from 2dB to 10dB, and elevates from there, reaching consistency at 25dB. It is observed that the LDA classifier is able to perform well even at lower SNRs in comparison to other classifiers, so LDA is considered for Fusion 2 in most cases. The Gaussian NB classifier is shown in Figure 6.11 (c), since the trend in the variation is captured well for analysis. At lower SNRs, there are heavy distortions in the spectrogram, causing the significant components to overlap with the artefacts. As a result, there are a lot of misclassifications, negatively impacting the classification performance. For the Fusion 1, an F1 score of 92% to 96% is observed, which is approximately an increase by 20% in comparison to the individual polarizations.

### 6.3.2 Drone Maneuvering in Rectangular Waypoints

In the scenario of drone moving as waypoints in a rectangle, the results of the parametric analyses are shown in Figure 6.12. The decision Fusion 1 and 2 are represented in black and yellow lines respectively in the plots.

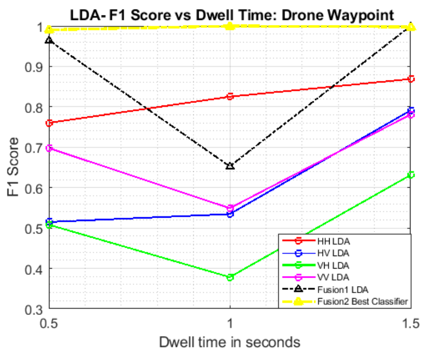


(a) F1 score VS Dwell time- Linear Discriminant Analysis Classifier

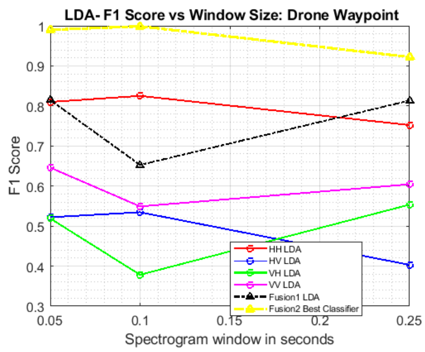


(b) F1 score VS Spectrogram Window Duration- Linear Discriminant Analysis Classifier

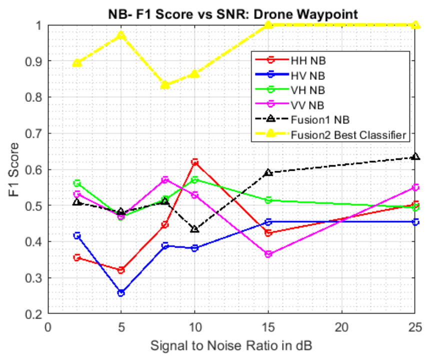


(c) F1 score VS SNR- Gaussian Naive Bayes Classifier

Figure 6.12: PARSAX data: Classification performance of classifiers as F1 score vs Parameters (a)Dwell Time; (b) Spectrogram window duration; (c) Noise: Drones along Rectangular Waypoints

- *Dwell Time:* In the first parametric analysis, the spectrogram split duration, that is, dwell time, is altered from 0.5s, 1 s and 1.5s, and it is demonstrated that the dwell times 0.5s and 1.5s have satisfactory classification outputs. As expected, the Line of Sight monostatic node HH has the maximum accuracy when individual polarization are considered. The cross-polarization VH has minimum F1 score of 38% at 1s dwell time, owing to the inability of the LDA classifier to accurately differentiate the M200 1kg class correctly (analyzed from confusion matrix). As a result of the non-optimal classification, the Fusion 1 exhibits no progress in performance. On the other hand, the Fusion 2 has an optimum performance of approximately 98% to 100% in each instance of dwell time. Between the two dwell times 0.5s and 1.5s, the shorter dwell time is better suited in the scenario of drones (and other targets), because it indicates that the radar is able to capture the drones' activities in a shorter time, so 0.5s is preferred.

- *Spectrogram Window Duration:* The second parametric analysis is the variation in the duration of spectrogram window. As in the case of drone flying for the PARSAX dataset, a diminishing trend in performance is noticed with the increase in duration of the spectrogram window for the drone flying in rectangular waypoints. The Fusion 1 shows minimal improvement in accuracy at 0.25s, whereas, at other instances of spectrogram windows, the Fusion 1 is not beneficial. However, the Fusion 2 exhibited much improvement, from 99% to 92% at the corresponding spectrogram window duration 0.05s and 0.25s. The reduction in F1 score at 0.1s duration of the window is due to misclassification of the quadcopter M200 1kg class by the LDA classifier. Thus, due to the orientation of samples in the confusion matrix, the augmentation of performance via Fusion 1 is not advantageous.

- *Noise:* The final parameter is the addition of noise. At lower SNRs, the classification performance deteriorates owing to the misclassification of some of the classes. So the samples are scattered throughout the confusion matrix, thus the diagonal matrix becomes weak due to lesser concentration of samples. However, it is seen the with the increase in SNR, due to lesser distortions, the classifier is able to segregate the samples according to their labels up to an extent. The pattern of gradual increase in performance is depicted by Gaussian NB classifier. Nevertheless, the Fusion 1 is able to show improvement at 25dB. Due to many inaccurate predictions at other lower SNRs, the decision Fusion 1 did not perform to its maximum potential. Here, (and also in other classifiers), the VH polarization has higher accuracy than the other polarizations, unlike the other parametric analyses, where HH has a greater result in terms of individual polarizations. Fusion 2, as in other cases attained 100% F1 score at 25dB. It can be inferred that the performance in the waypoint scenario is likely to increase for some SNR values before achieving the cut-off value. The LDA classifier works well with data with noise, in being able to classify when the SNR is less.

### 6.3.3 Drone Flying and Maneuvering in Rectangular Waypoints

This scenario is the extended case which involves the combination of drone flying and moving waypoints in a rectangle. This is a more realistic scenario and the parametric analyses from Figure 6.13 are examined.

- *Dwell Time:* The HH polarization has the highest classification performance with 84% at 0.5s, reaching up to 88% at 1s dwell times. The HH polarization, along with the other polarizations unanimously resulted in lesser classification performance with the increase in dwell time. Thus, the inference is that a shorter dwell time is desired in this scenario. The number of samples is increased due to the combined set of information from the standalone scenarios of drone flying and rectangular waypoint movements. The classifiers were fed with a sufficient number of data points to enable them to discriminate among the classes, and hence surpassing the independent performances of flying and waypoints. By fusing the outputs from individual polarimetric channels, a significant improvement in performance up to 99% is achieved for both the decision fusions Fusion 1 and Fusion 2.

- *Spectrogram Window Duration:* As the spectrogram window duration is increased, the resolution in time becomes worse, and significant components in feature extraction may become spread out across windows. Though the number of samples in the dataset remains the same, the classifier gives a lesser accuracy for the increase in the spectrogram window duration. The HH polarization yielded a significant increase in each instance of window duration. So, in this scenario, the ideal window size is obtained to be 0.1s. Again, with fusion, an optimum F1 score of approximately

100% is established at 0.1s, which is a 12% increase that the independent HH polarization. Also, an overall accuracy increase is found at each instance of varying spectrogram window duration for both Fusions 1 and 2.

- *Noise:* The HH polarization again has a better performance when compared to other classifiers. It is observed that the VH polarimetric channel performs particularly well when noise is present, such that the performance is better than HV and VV polarizations, which is in contrast to other parametric analyses where VH usually performs poorly. The decision fusion of LDA classifier for each polarimetric channel outperforms the individual channel's accuracy. As the SNR is decreased, the classification performance also worsens as expected, falling by around 20% below the ideal state of high SNR. Fusion 2 attained an F1 score of 100% with an increase in SNR.

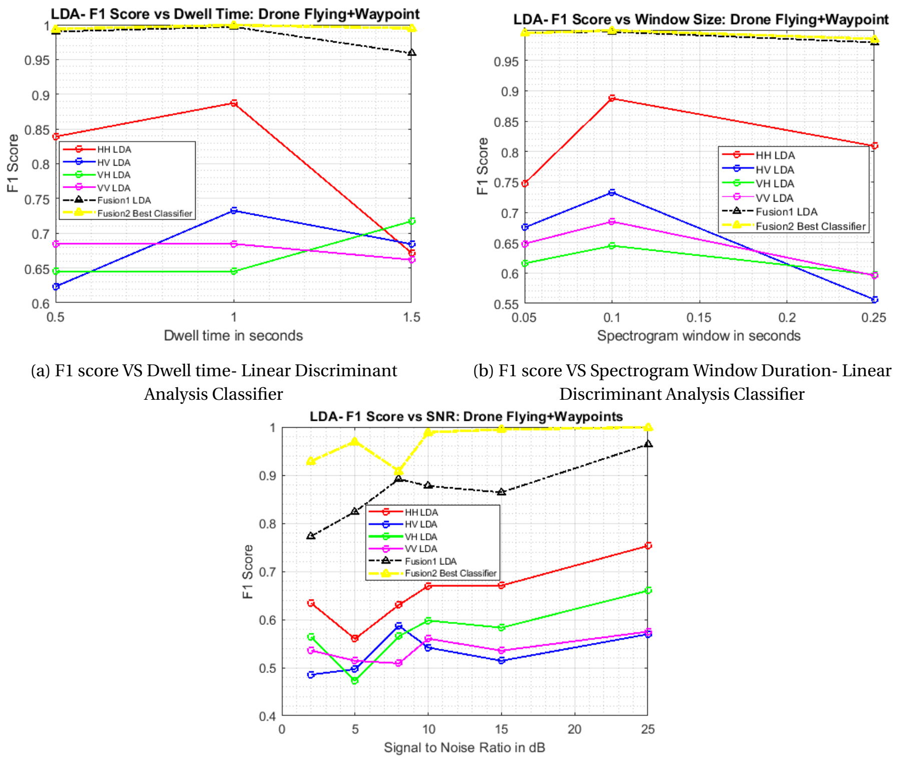


(a) F1 score VS Dwell time- Linear Discriminant Analysis Classifier

(b) F1 score VS Spectrogram Window Duration- Linear Discriminant Analysis Classifier

(c) F1 score VS SNR- Linear Discriminant Analysis Classifier

Figure 6.13: PARSAX data: Classification performance of classifiers as F1 score vs Parameters (a)Dwell Time; (b) Spectrogram window duration; (c) Noise: Drones Flying and Maneuvering in Rectangular Waypoints

### 6.3.4 Drone Hovering

This is the straightforward case when the drone is not making any movement, but is just hovering in mid-air and the variations in the parameters are illustrated in Figure 6.14.

- *Dwell Time:* The spectrogram is split into shorter time segments of durations 0.5s, 1s and 1.5s. The HH polarimetric channel, as observed in other scenarios shows higher accuracy than the rest of the channels in terms of performance based on individual polarimetric channels. Since the target does not follow any trajectory, the samples were classified easily by the LDA classifier. The optimum dwell time is 1s, since all the polarimetric channels have good performance. The HH polarization has approximately 95% to 100% accuracies in all the dwell times. Employing Fusion 1 and Fusion 2 enhanced the classification performance overall, reaching 100% accuracy.

- *Spectrogram Window Duration:* The shorter spectrogram window duration of 0.05s produced a better performance. Unlike in other scenarios where the longer spectrogram window resulted in much lesser accuracy, the 0.25s spectrogram window achieved from approximately 70% to 95% for HV and HH polarizations respectively, indicating lesser misclassifications even with diminishing time resolution. The Fusion 1 and Fusion 2 attained 100% accuracy in all the spectrogram window durations, due to lesser incorrect predictions by the classifiers as a result of simplistic samples.

- *Noise:* The similar trend of increase in classification performance with an increase in SNR is observed, and is shown by the LDA classifier here. An instant rise in accuracy is observed from 2dB to 8dB, but again reduces at 10dB and gradually increases up to 25dB. Since the SNR at which the original dataset is recorded is unknown, it is not possible to determine the cut-off accuracy beyond which the increase in SNR will not affect the classification performance. The Fusions 1 and 2 showed an overall improvement, with Fusion 2 performing better than Fusion 1.

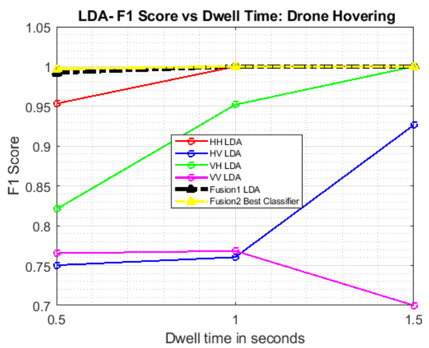


(a) F1 score VS Dwell time- Linear Discriminant Analysis Classifier

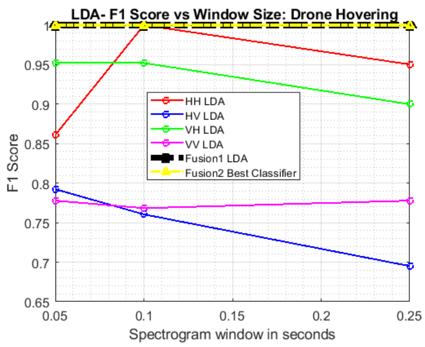


(b) F1 score VS Spectrogram Window Duration- Linear Discriminant Analysis Classifier

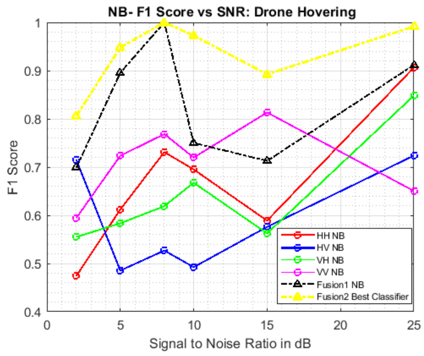


(c) F1 score VS SNR- Gaussian Naive Bayes Classifier

Figure 6.14: PARSAX data: Classification performance of classifiers as F1 score vs Parameters (a)Dwell Time; (b) Spectrogram window duration; (c) Noise: Drones Hovering

### 6.3.5 Polarimetric Features Classification

In the previous sections, the results from the statistical features (mean, standard deviation, skewness and kurtosis) that are derived via the application of SVD, centroid and bandwidth on the spectrogram are discussed, along with their inferences on the parametric analyses (dwell time, spectrogram window, noise).

In this case, the polarimetric channels (VV, VH, HV, HH) are combined together into a single polarimetric block. The dwell time, intended as the duration of the segment of data used for polarimetric feature extraction, is varied from 0.05s, 0.10s, 0.25s, 0.5s and 1.0s. It is observed that for a shorter dwell time, the classifier performs efficiently. A shorter dwell time is often desirable as it proves the efficiency of the classifier's ability to distinguish between classes in the shortest time possible.

| Classifier | Hovering | Flying | Rectangular Way-points | Flying+Rectangular Waypoints |
|---|---|---|---|---|
| LDA | 86.5 | 52.8 | 57.4 | 48.4 |
| Naive Bayes | 79.1 | 45.3 | 34.2 | 42.0 |
| Fine Decision Tree | 89.6 | 66.0 | 76.1 | 67.2 |
| Linear SVM | 87.7 | 61.2 | 60.0 | 50.9 |
| Ensemble Fusion | 99.9 | 90.5 | 95.9 | 75.8 |

Table 6.6: PARSAX data: Classification performance F1 score (Percentage) for polarimetric features for Dwell time of 0.05s

From the Table 6.6, it is observed that that the performance of the independent classifiers for all the scenarios except hovering is around 35% to 65%, but the ensemble of classifiers resulted in a significant improvement. However, though the standalone cases of flying and rectangular waypoints achieved 90.5% and 95.9% F1 score respectively, the combined scenario produced only 75.8% upon fusion. This is contrasting to the scenario of flying + waypoints via spectrogram where a higher accuracy is obtained. This is because, firstly, in this case, the spectrogram is split into much smaller segments of duration 0.05s (which is 20 times lesser than the 1s split in spectrogram), thus resulting in a much greater number of samples after feature extraction. Although a larger number of samples is favourable for the classifiers to train efficiently, in this situation, the classifier is confused due to incoherent samples from different drone trajectories. The overload of irrelevant information to the classifier resulted in the lesser classification performance. Secondly, the samples in the confusion matrix from the product of the ensemble fusion are distributed haphazardly, and not concentrated in the main diagonal, which again results in distorted performance. However, these polarimetric features that were employed to differentiate between birds and UAVs [8], have performed well in this research of differentiating different scenarios of drones with payloads.

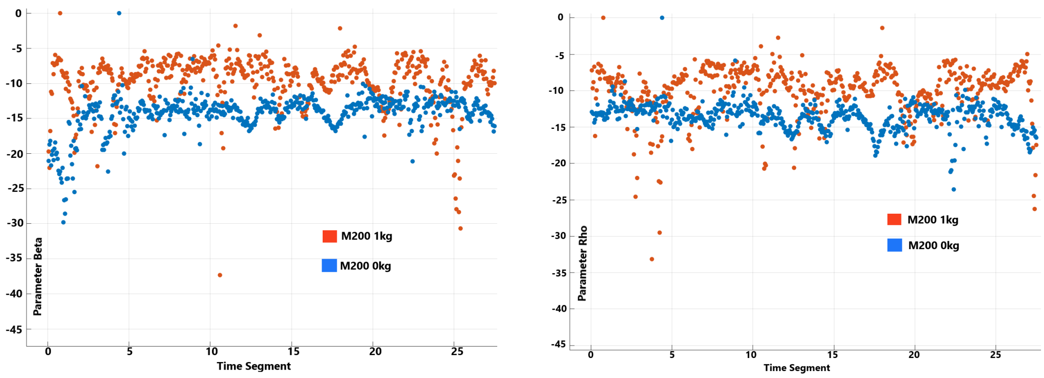


(a) Feature $\beta$

(b) Feature $\rho$

Figure 6.15: PARSAX data: Feature samples for the case of Quadcopter M200 hovering for (a) Feature $\beta$; (b) Feature $\rho$, dwell time = 0.05s. Red (payload); blue (no payload)

The classifiers with the polarimetric features are able to attain a classification performance equivalent to that obtained in different scenarios by time-frequency domain (spectrograms). The performance in polarimetric features is achieved even without the application Short-Time Fourier Transform, which is one step lesser computationally in the signal processing chain. Moreover, at a shorter dwell time of 0.05s, an improved accuracy is obtained for the classification based on polarimetric features, whereas for features extracted from spectrograms of independent polarimetric channels, the ideal dwell time is 0.5s-1s, which is comparatively longer.

In [10] and [19], it is shown how the presence of a payload would be visible in the faster rotation rate of the UAVs blades in the spectrograms, and this would be exploited for classification. Similar separation for the payload vs no-payload classes can be seen in Figure 6.15 for two examples of polarimetric features related to the hovering quadcopter. Unlike the easier kinematic interpretation of blade velocity in spectrograms, the electromagnetic interpretation of this separation seen in the polarimetric feature domain is still under investigation.

## 6.4 Conclusion

In this chapter, comprehensive discussions on fusion techniques and parametric results obtained from the analysis of the two experimental datasets, NetRAD and PARSAX, are covered. The key take-aways from this chapter are:

- The feature fusion had a negative impact on the classification performance as a result of combining diverse data. However, the decision fusion enhanced the overall classification performance. So the feature fusion technique is overruled.
- The parameters considered for analysis were varying (a) dwell time, (b) spectrogram window duration and (c) noise. The Table 6.7 shows the values of dwell time providing the optimal results, i.e. the highest F1 score (at individual node and by fusion) obtained by changing the dwell time. The summary of the outcomes from the two datasets (NetRAD and PARSAX) is tabulated in Table 6.8.
- In the NetRAD dataset, the independent nodes performed well for the hovering scenario, even without the intervention of the Fusion 1 and Fusion 2 techniques. However, a significant improvement in performance was yielded for Fusion 1 and Fusion 2, compared to the individual nodes for the drone flying.
- Multiple scenarios of drone movement was considered for the PARSAX data, in order to verify if the feature extraction technique worked regardless of the trajectories and produced optimal classification.
- The polarimetric features from the PARSAX data secured optimum performance at a much shorter dwell time of 0.05s for the features extracted on the RTI plot, hence outperforming the statistical features.

| **NetRAD Data** | | |
|---|---|---|
| **Scenarios** | **Maximum F1 Score (%) Individual Node** | **F1 Score (%) Fusion(Dwell Time)** |
| Drone Flying | Approx. 55% at 0.5s for Node 3 | 89% to 96% |
| Drone Hovering | Approx. 95% at 0.75s for Nodes 1, 3 | 100% |
| **PARSAX Data** | | |
| **Scenarios** | **Maximum F1 Score (%) Individual channel** | **F1 Score (%) Fusion(Dwell Time)** |
| Drone Flying | 100% at 1.5s for HH | Approx. 100% |
| Drone Rectangular Waypoints | Approx. 78% at 0.5s for HH | 100% |
| Drone Flying + Rectangular Waypoints | Approx. 88% at 1s for HH | Approx. 100% |
| Drone Hovering | Approx. 100% at 1s for HH | 100% |

Table 6.7: Optimum F1 score (as percentage) based on Dwell time for all scenarios for independent nodes/ channels: NetRAD and PARSAX datasets

| NetRAD Data | | | | | |
|---|---|---|---|---|---|
| **Scenarios** | **Dwell Time** | **Spectrogram Window** | **Noise** | **Fusion 1** | **Fusion 2** |
| Drone Flying | Maximum accuracy at 0.5s<br><br>Shorter dwell time | Maximum accuracy at 0.05s to 0.1s<br><br>Shorter spectrogram window duration | Increases with SNR | Significant improvement | Significant improvement<br><br>Fusion 2 > Fusion 1 |
| Drone Hovering | Maximum accuracy at 0.75s and 2s<br><br>Comparatively shorter dwell time of 0.75s | Maximum accuracy at 0.05s<br><br>Shorter spectrogram window duration | Increases with SNR<br><br>Fusion 1 and Fusion 2 resulted in 100% accuracy | Significant improvement | Significant improvement<br><br>Fusion 1 = Fusion 2 |
| **PARSAX Data** | | | | | |
| **Scenarios** | **Dwell Time** | **Spectrogram Window** | **Noise** | **Fusion 1** | **Fusion 2** |
| Drone Flying | Maximum accuracy at 1s to 1.5s<br><br>Comparatively longer dwell time | Maximum accuracy at 0.05s<br><br>Shorter spectrogram window duration | Increases with SNR<br><br>LDA works well at lower SNR | Minimal improvement in Dwell time and Window duration<br><br>Significant improvement for Noise | Significant improvement<br><br>Almost 100% accuracy |
| Drone Rectangular Waypoints | Maximum accuracy at 0.5s and 1.5s<br><br>Shorter dwell time preferred, so 0.5s | Maximum accuracy at 0.05s to 0.1s<br><br>Shorter spectrogram window duration | Increases with SNR<br><br>LDA works well at lower SNR | Minimal improvement in Dwell time and Window duration<br><br>Significant improvement for Noise | Significant improvement<br><br>Almost 100% accuracy |

| | | | | | |
|---|---|---|---|---|---|
| Drone Flying + Rectangular Waypoints | Maximum accuracy at 1s<br><br>Shorter dwell time | Maximum accuracy at 0.1s<br><br>Shorter spectrogram window duration | Increases with SNR | Significant improvement | Significant improvement |
| Drone Hovering | Maximum accuracy at 0.5s and 1s<br><br>Shorter dwell time preferred | Maximum accuracy at 0.05s<br><br>Shorter spectrogram window duration | Increases with SNR | Significant improvement<br><br>Almost 100% accuracy | Significant improvement<br><br>Almost 100% accuracy |

Table 6.8: Summary of results from parametric analyses of NetRAD PARSAX datasets for the different drone scenarios

# Chapter 7

# Conclusion and Future Work

*In this thesis, the main concepts of radar signal processing, generation of micro-Doppler signature, extraction of suitable statistical and polarimetric features, analysis of supervised machine learning classifiers decision fusion algorithms are examined in detail and formulated the techniques on two sets of experimental data from single polarimetric and fully polarimetric radars.*

*The entirety of this research is segregated sequentially based on the step-wise research methodology. The initial proof of concept is carried to highlight the importance of micro-Doppler signature to visualize the fuselage and rotor blade flashes. The novel approach on statistical and polarimetric feature extraction algorithms and decision fusion on supervised classification are delineated in-depth in Chapter 5*

*In this chapter, the final outcomes and highlights have been articulated in the conclusions on the results. Based on the findings from this thesis and subsequent limitations, potential additional investigations are suggested for the future fields of view.*

## 7.1 Conclusion

The thesis emphasizes the growing need to monitor operations of drones that are carrying payloads, as a result of increased reports on drones being one of the major contributors of malicious activities. The state of the art works of literature is dominated by extensive studies on the detection of the presence of drone, and distinguishing between drones and birds, and other targets. The niche subject sheds light on the domain of drones carrying payloads and since there is not much assessment about it at least in the open literature, this thesis aims to address some of the prevailing literature gaps by providing novel solutions. The approach and contributions, in brief, involve extracting polarimetric and statistical features from spectrograms, which are given as input to the supervised classifiers. Unique fusion techniques are proposed to enhance the classification performance, and the algorithms are applied on two sets of real experimental data.

The objective of the thesis is to tackle the issue of drones that are carrying payloads of different weights by optimum classification. The initial task is to identify key attributes of drones and payloads, such that they can be used as relevant parameters for classification. From literature reviews, the Radar Cross Section (RCS) was considered to be an insignificant parameter, owing to the small difference between the RCS of the drone and that of the drone and payload combined. This concept was quantitatively reiterated in the thesis by mathematical modelling based on certain approximations to generate a simplistic model. The geometry of the drone and payload were assumed to be spherical and would lie in the optical region, and the material of the payload is Aluminium. However, the insignificant difference of 1-3 dBsm between RCS of drone alone and that of drone and payload combined stabilized the theory mentioned in literature studies. On the contrary, a visible distinction between the drone and payload was observed in the Doppler and micro-Doppler signatures, as seen in [10] and [23]. Moreover, the trajectories followed by the drone (with and without payload), impact due to heavier payloads, effect on the drone due to dynamic payload, and other minute details were observed in the time-frequency plots, thus establishing an infallible approach to detection and classification of drones carrying payloads. The rest of the thesis employed spectrograms for further in-depth analysis.

The choice of datasets depended on the types of radar: a single polarimetric NetRAD radar and fully polarimetric PARSAX radar collected original data of dimensions (15000 x 128) and (114688 x 400) respectively in pulse and range bins. The scenarios were drone DJI Phantom Vision 2+ hovering and flying for NetRAD data with classes of payloads 0g, 200g, 300g, 400g and 500g; and M200 Quadcopter with 0kg/ 1kg and M600 Hexacopter with 0kg/ 2.35 kg for PARSAX data where the scenarios were drones hovering, flying, and moving in rectangular waypoints. The flattening of the blade flashes in the spectrogram was evident in the NetRAD data when the drone carried heavier payloads.

For the extraction of suitable features, two independent sets of features were generated. The first one was statistical features that were derived by direct application of Singular Value Decomposition (SVD), Centroid and Bandwidth (BW). The next set of features was polarimetric features, specific to PARSAX data only since it tapped information from all its polarimetric channels. In all, there were 12 statistical features and 5 polarimetric features. The samples after feature extraction were uniform for NetRAD data, however; for the PARSAX data, the samples were inconsistent due to the drones temporarily leaving the radar beam at times during data collection.

Following feature extraction, the data points were fed to the classifier to evaluate the performance metrics. The thesis focused on supervised machine learning, so the classifiers (a) Linear Discriminant Analysis (LDA), (b) Gaussian Naive Bayes (NB), (c) Fine Decision Tree (DT) and (d) Linear Support Vector Machine (SVM), were selected based on the accuracy and computational time. For both the NetRAD and PARSAX datasets, a multiclass problem was assigned, to closely relate to realistic drone applications. The NetRAD data was a 5-class problem, whereas the PARSAX data dealt with a 4-class problem, where the payloads were the different classes. The classifier was trained using 80% data with 5-fold cross-validation and tested on 20% of the samples. The macro-F1 score was evaluated to assess the classification performance (weighted F1 score for PARSAX data due to uneven distribution of samples).

The different novel fusion techniques were aimed at further improving the classification performance. The three types of fusion were feature fusion, decision fusion and ensemble fusion. The feature fusion was used after the feature extraction phase, the decision fusion operated after the classification phase, and the ensemble fusion was specific to the polarimetric features. After calculating the F1 score, it was observed that feature fusion resulted in a reduced accuracy whereas decision fusion produced better performance comparative to when only independent nodes were considered. In the NetRAD data for drone hovering, the independednt nodes produced F1 score in the range 85%-97%. However, the feature fusion reduces the values to 58%, on the other hand, decision fusion yielded 100% performance. The depreciating performance using feature fusion was due to combining samples from nodes that perceived the drone and the payload from different aspect angles. On the contrary, the decision fusion was concentrated only with the outcomes from the nodes or polarimetric channels for subsequent evaluations.

The thesis extended to analyze the impact on classification performance by subjecting the different scenarios of drones (from both datasets) to various parametric analyses in order to achieve a pattern of variation in performance. The summary of the observations is tabulated in Table 6.8 of Chapter 6. The decision Fusion 1 and 2 contributed positively with a prominent increase in accuracy. To recap, Fusion 1 involves assigning the same classifier to each node or channel, while, on the other hand, Fusion 2 selects the best classifier from each node to evaluate the performance metrics. The parameters and consolidated observations were:

- *Varying dwell time:* Shorter dwell time was favourable since it produced an increase in relevant samples from feature extraction. So, the classifiers attained a higher classification performance.
- *Varying spectrogram window duration:* Shorter window duration was preferred in most scenarios, since it resulted in better resolution in time (by compromising on frequency up to an extent).
- *Addition of noise to vary SNR:* Lower SNR resulted in spectrogram with distortions, hence there were overlapping significant components in feature extraction. Classification performance improved with an increase in SNR.

Finally, the polarimetric features were derived from the RTI plots for the PARSAX dataset. In this case, ensemble fusion is applied, by making use of the results from the individual classifiers. It was found that an equivalent classification performance to that of statistical features was obtained here at a much shorter dwell time (of 0.05s) than that of the spectrogram. A notable point is that the comparable performance was attained even without the application of STFT, which means one lesser computational step in signal processing. The advantage of this approach would be overcoming the necessity to generate spectrograms for feature extraction. Moreover, the features were successfully able to differentiate between the payloads, thus making this set of features equally feasible.

Thus, for the statistical features from both datasets, a maximum of 95% to 100% accuracy was achieved upon decision fusion for the NetRAD and PARSAX datasets (at 0.5s to 1s dwell time). On the other hand, the polarimetric features attained an accuracy up to 99% by ensemble fusion, at a much shorter dwell time of 0.05s.

The conference paper, titled ***'Classification of Unmanned Aerial Vehicles (UAVs) Carrying Payloads with Polarimetric Radar'*** that has been submitted to the European Microwave Week 2021, summarizes the results from this thesis.

## 7.2 Limitations and Future Work

Although this thesis provides robust techniques for the extraction of features and optimum classification performance, there are few shortcomings. The main focus of the research dealt with the classification of drones with payloads, and the electromagnetic background and the detection of drones are not covered in detail. On the basis of the results, some of the directions in which the research can be taken forward are mentioned below:

- The electromagnetic interpretation of the kinematics of blade velocity needs to be investigated from the polarimetric features. The spectrogram was able to distinctly identify the variation in payload weight from the change in rotor velocity. The polarimetric features that are largely based on the Range Time plot are also able to establish the distinction in weights for different classes of payloads, as seen in Figure 6.15. However, the theory of making a more representative EM model of drones and payloads and their corresponding reasoning behind the dispersion of payload classes can be explored further, also by incorporating different weights of payloads and drone models. Furthermore, additional polarimetric aspects can be probed for extraction.
- Comparison with other time-frequency distributions. In this research, the micro-Doppler signatures were assessed using the spectrogram. Although the spectrogram has yielded remarkable classification performance, it can be verified if the same set of features are specific only to Short-Time Fourier Transform (STFT) technique. In this thesis, it is already established that these sets of

features work well with the two different sets of data from NetRAD and PARSAX. As an extension to the same set of feature extraction and supervised machine learning algorithms, other time-frequency plots, such as scalogram from the application of wavelets, Wigner-Ville distribution, etc. can be examined. A contrast in the classification performance among the time-frequency distributions can be evaluated. By analyzing their performances, it can also be determined if these feature extraction techniques are robust irrespective of their time-frequency distributions also.

- Multiple sensors can be employed for the detection and classification of drones carrying payloads. For example, incorporating a camera with radar to optimize the detection and classification performance. A similar technique on sensor fusion was investigated in [43] for categorizing human activities. The research can be limited to a smaller arena considering the specification of the sensors. The different fusion techniques (hard and soft fusions) can be evaluated for the same set of statistical and polarimetric features.
- As a continuation on using multiple sensors, algorithms to evaluate qualitatively the nature and composition of the payload can be researched, after identifying the presence of payload and its associated quantitative attributes.
- Different sets of features can be evaluated (e.g. physical features of drones) by performing other algorithms on the spectrograms or other time-frequency distributions. Additionally, various complex machine learning or deep learning algorithms can be utilized for attaining optimum classification, even without the application of fusion techniques.

# Appendix A

# Radius and RCS calculation of metallic spherical payloads

*In this section, the detailed calculation of the radius and Radar Cross Section (RCS) of the payloads of different DJI drone models is covered. The specifications of the drones are taken from [29]. The payload that the drone is carrying is approximated to be spherical in shape for simplicity.*

*The different models of drones considered for calulation of RCS of their payloads are (a) General DJI drone, (b) DJI Mavic, (c) DJI Mavic 2, (d) DJI Mavic Mini/ Mini 2, (e) DJI Agras T20. Detailed information can be found in Table 3.3.*

*Various models of drones and their allowable payload weights are chosen in order to verify if RCS can be considered as an optimal parameter for the detection and classification of drones carrying payloads. The results are summarized in Table 3.4.*

The calculations are as follows:

- *Radius of payload for DJI Mavic with payload of 1200 g:*

$$\begin{aligned}
\text{Mass = Density * Volume} \\
Volume = \frac{Mass}{Density} \\
\text{For a DJI Mavic drone, weight of payload} = 1200g \\
\text{Density of Aluminium} = 2.7g/cm^3 \\
Volume = \frac{1200g}{2.7gcm^{-3}} = 444.44cm^3 \\
\text{Volume of sphere} = \frac{4}{3}\pi r^3 = 444.44cm^3 \\
\text{Radius of payload} r_{DJImavic1200} = 4.73cm \\
\text{RCS of sphere at high frequency in the optical region} = \\
\pi * r^2_{DJImavic1200} = 3.14 * (4.73)^2 = 70.25cm^2
\end{aligned} \quad (A.1)$$

- *Radius of payload for DJI Mavic with payload of 300g:*

$$
\begin{aligned}
\text{Mass} &= \text{Density} * \text{Volume} \\
Volume &= \frac{Mass}{Density} \\
\text{For a DJI Mavic drone, weight of payload} &= 300g \\
\text{Density of Aluminium} &= 2.7g/cm^3 \\
Volume = \frac{300g}{2.7gcm^{-3}} &= 111.11cm^3 \\
\text{Volume of sphere} = \frac{4}{3}\pi r^3 &= 111.11cm^3 \\
\text{Radius of payload} r_{DJImavic300} &= 2.98cm \\
\text{RCS of sphere at high frequency in the optical region} &= \\
\pi * r^2_{DJImavic300} = 3.14 * (2.98)^2 &= 27.88cm^2
\end{aligned}
\tag{A.2}
$$

- *Radius of payload for DJI Mavic with payload of 400 g:*

$$
\begin{aligned}
\text{Mass} &= \text{Density} * \text{Volume} \\
Volume &= \frac{Mass}{Density} \\
\text{For a DJI Mavic drone, weight of payload} &= 400g \\
\text{Density of Aluminium} &= 2.7g/cm^3 \\
Volume = \frac{400g}{2.7gcm^{-3}} &= 148.15cm^3 \\
\text{Volume of sphere} = \frac{4}{3}\pi r^3 &= 148.15cm^3 \\
\text{Radius of payload} r_{DJImavic400} &= 3.28cm \\
\text{RCS of sphere at high frequency in the optical region} &= \\
\pi * r^2_{DJImavic300} = 3.14 * (3.28)^2 &= 33.78cm^2
\end{aligned}
\tag{A.3}
$$

- *Radius of payload for DJI Mavic 2 :*

$$
\begin{aligned}
\text{Mass} &= \text{Density} * \text{Volume} \\
Volume &= \frac{Mass}{Density} \\
\text{For a DJI Mavic 2 drone, weight of payload} &= 1100g \\
\text{Density of Aluminium} &= 2.7g/cm^3 \\
Volume = \frac{1100g}{2.7gcm^{-3}} &= 407.41cm^3 \\
\text{Volume of sphere} = \frac{4}{3}\pi r^3 &= 407.41cm^3 \\
\text{Radius of payload} r_{DJImavic2} &== 4.60cm \\
\text{RCS of sphere at high frequency in the optical region} &= \\
\pi * r^2_{DJImavic2} = 3.14 * (4.60)^2 &= 66.44cm^2
\end{aligned}
\tag{A.4}
$$

- *Radius of payload for DJI Mavic Mini/ Mini 2 :*

$$
\begin{aligned}
\text{Mass} &= \text{Density} * \text{Volume} \\
Volume &= \frac{Mass}{Density} \\
\text{For a DJI Mavic Mini/ Mini 2 drone, weight of payload} &= 80g \\
\text{Density of Aluminium} &= 2.7g/cm^3 \\
Volume &= \frac{80g}{2.7gcm^{-3}} = 29.63cm^3 \\
\text{Volume of sphere} &= \frac{4}{3}\pi r^3 = 29.63cm^3 \\
\text{Radius of payload} r_{DJImavicmini} &= 1.92cm \\
\text{RCS of sphere at high frequency in the optical region} &= \\
\pi * r^2_{DJImavicmini} &= 3.14 * (1.92)^2 = 11.58cm^2
\end{aligned}
\tag{A.5}
$$

- *Radius of payload for DJI Agras T20 with payload of 15100 g:*

$$
\begin{aligned}
\text{Mass} &= \text{Density} * \text{Volume} \\
Volume &= \frac{Mass}{Density} \\
\text{For a DJI Agras T20 drone, weight of payload} &= 15100g \\
\text{Density of Aluminium} &= 2.7g/cm^3 \\
Volume &= \frac{15100g}{2.7gcm^{-3}} = 5592.59cm^3 \\
\text{Volume of sphere} &= \frac{4}{3}\pi r^3 = 5592.59cm^3 \\
\text{Radius of payload} r_{DJIagras1} &= 11.01cm \\
\text{RCS of sphere at high frequency in the optical region} &= \\
\pi * r^2_{DJIagras1} &= 3.14 * (11.013)^2 = 380.63cm^2
\end{aligned}
\tag{A.6}
$$

- *Radius of payload for DJI Agras T20 with payload of 20000 g:*

$$
\begin{aligned}
\text{Mass} &= \text{Density} * \text{Volume} \\
Volume &= \frac{Mass}{Density} \\
\text{For a DJI Agras T20 drone, weight of payload} &= 20000g \\
\text{Density of Aluminium} &= 2.7g/cm^3 \\
Volume &= \frac{20000g}{2.7gcm^{-3}} = 7407.41cm^3 \\
\text{Volume of sphere} &= \frac{4}{3}\pi r^3 = 7407.41cm^3 \\
\text{Radius of payload} r_{DJIagras2} &= 12.09cm \\
\text{RCS of sphere at high frequency in the optical region} &= \\
\pi * r^2_{DJIagras2} &= 3.14 * (12.09)^2 = 458.97cm^2
\end{aligned}
\tag{A.7}
$$

# Appendix B

# Range Time Plots and Spectrograms

*In this section, the Range Time plots and spectrogram of some of the scenarios from the NetRAD and PARSAX data are covered. The detailed explanation on the micro-Doppler signatures can be found in Chapters 4 and 5. In the RTI plot, the pink block denotes the area of interest where the micro-drone is present. The PARSAX data contains signatures of the drone to be sporadic since the drone moved away from the radar beam at some instances, where as the NetRAD data is continuous throughout.*

## B.1 PARSAX Data: Range Time Plots

This section presents the RTI plots for the M200 Quadcopter for the scenarios of drone flying and moving along rectangular waypoints. The plots focus mainly on the situations where the drones are carrying a payload. The other cases of M600 Hexacopter with 2.35 kg payload is discussed previously in the thesis in Chapter 4.

From the RTI plots of B.1 and B.2, it is visible that the drones in rectangular waypoints are spread out in larger number of range bins compared to the flying scenario, owing to the fact of the drones following different trajectories. The irregularities in the plots is due to the drones momentarily departing the radar beam.

1. PARSAX Data: RTI Plot of M200 Quadcopter flying with 1kg payload

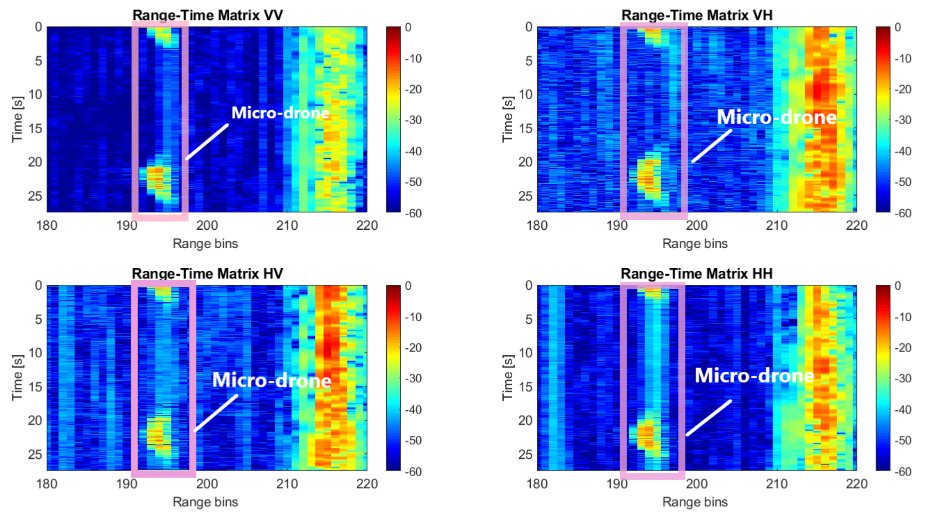


Figure B.1: PARSAX Data: RTI Plot VV, VH, HV, HH channels for Drone M200 Quadcopter Flying with 1kg payload

2. PARSAX Data: RTI Plot of M200 Quadcopter moving in rectangular waypoints with 1kg payload

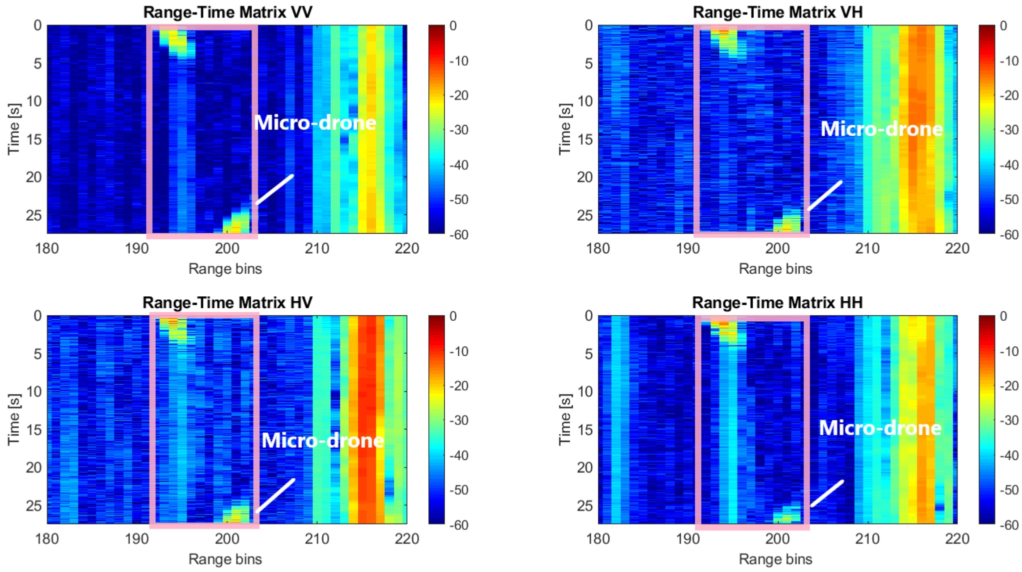


Figure B.2: PARSAX Data: RTI Plot of VV, VH, HV, HH channels for Drone M200 Quadcopter Waypoint with 1kg payload

## B.2 Time-Frequency Plots: Spectrograms

In this section, the time-frequency plots, that is spectrograms of some of the scenarios of drones from the NetRAD and PARSAX datasets are illustrated.

### B.2.1 NetRAD Data

Firstly, the NetRAD dataset is considered. The RTI plots have been discussed in-depth in Chapter 4. The spectrograms for the scenarios of drone hovering and flying for the cases of 0g and 500g are explained in Chapter 5.

The spectrograms in this section focus on the Nodes 2 and 3, for the similar scenarios of hovering and flying without payload and with 500g payload. The choice of these two cases is to demonstrate how the blade flashes vary for these extreme cases. 1. NetRAD Data: Spectrogram of drone hovering without any payload and with 500g payload: Node 2

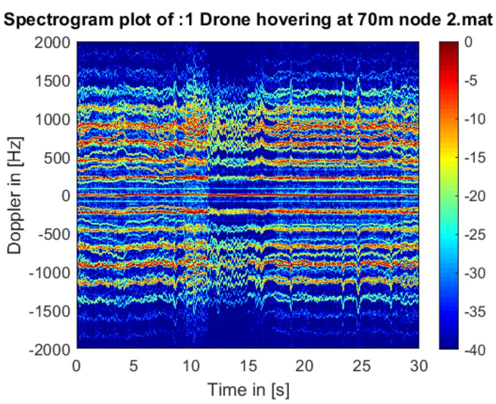


(a) Drone hovering without payload at N2

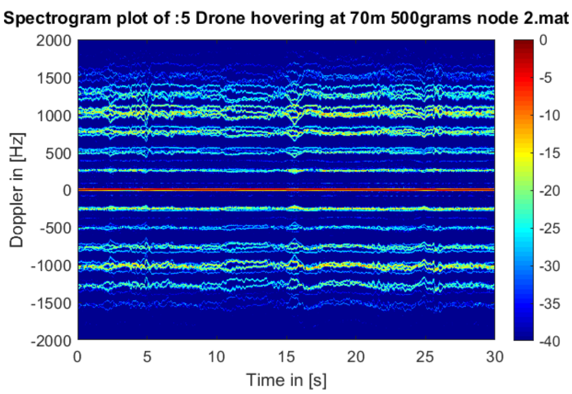


(b) Drone hovering with 500g at N2

Figure B.3: NetRAD Data: Spectrogram of Drone hovering at N2 (a) No payload; (b) 500g payload

2. NetRAD Data:Spectrogram of drone hovering without any payload and with 500g payload:Node 3

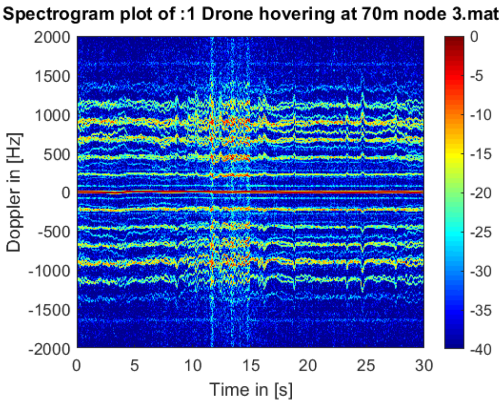


(a) Drone hovering without payload at N3

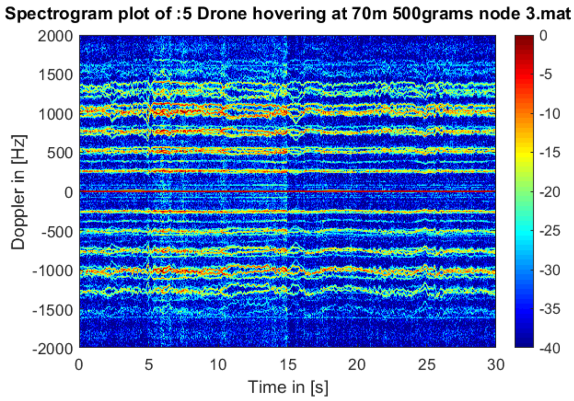


(b) Drone hovering with 500g at N3

Figure B.4: NetRAD Data: Spectrogram of Drone hovering at N3 (a) No payload; (b) 500g payload

3. NetRAD Data: Spectrogram of drone flying without any payload and with 500g payload: Node 2

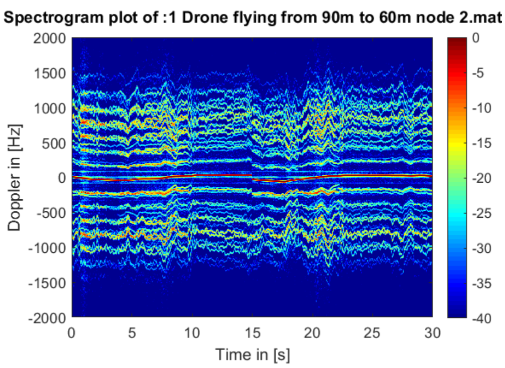


(a) Drone flying without payload at N2

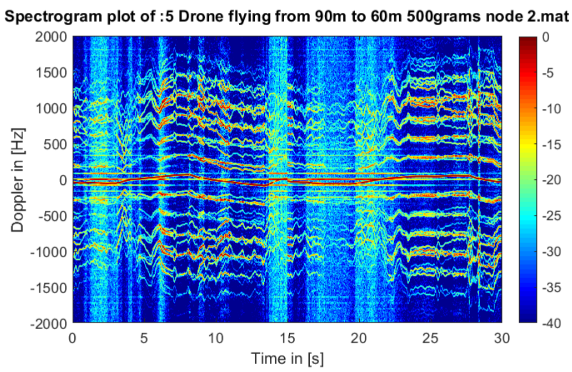


(b) Drone flying with 500g at N2

Figure B.5: NetRAD Data: Spectrogram of Drone flying at N2 (a) No payload; (b) 500g payload

4. NetRAD Data: Spectrogram of drone flying without any payload and with 500g payload: Node 3

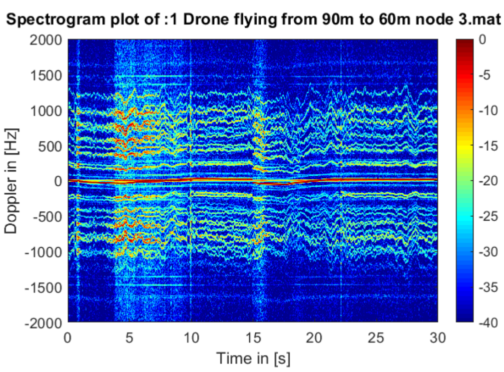


(a) Drone flying without payload at N3

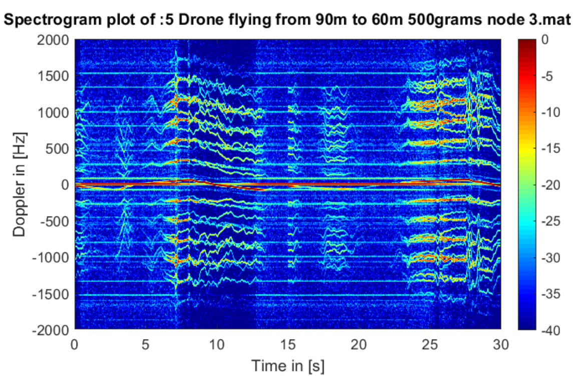


(b) Drone flying with 500g at N3

Figure B.6: NetRAD Data: Spectrogram of Drone flying at N3 (a) No payload; (b) 500g payload

### B.2.2 PARSAX Data

Secondly, the PARSAX dataset is used for plotting the spectrograms. As seen already in RTI plots of Figures B.1 and B.2, the drones temporarily leave the radar beam, hence resulting in discontinuity in the plots. In order to optimize the process, only the contributing segments where the blade flashes are present in the spectrogram are taken, and used later for feature extraction. Hence, their dimensions also vary accordingly based on their spectrograms. The micro-Doppler signatures of M200 Quadcopter and M600 hexacopter carrying payloads for the scenarios of drones flying and moving along rectangular waypoints are depicted in this section in the Figures B.7, B.8 and B.9.

1. PARSAX Data: Spectrogram of M200 Quadcopter flying with 1kg payload at all polarimetric channels

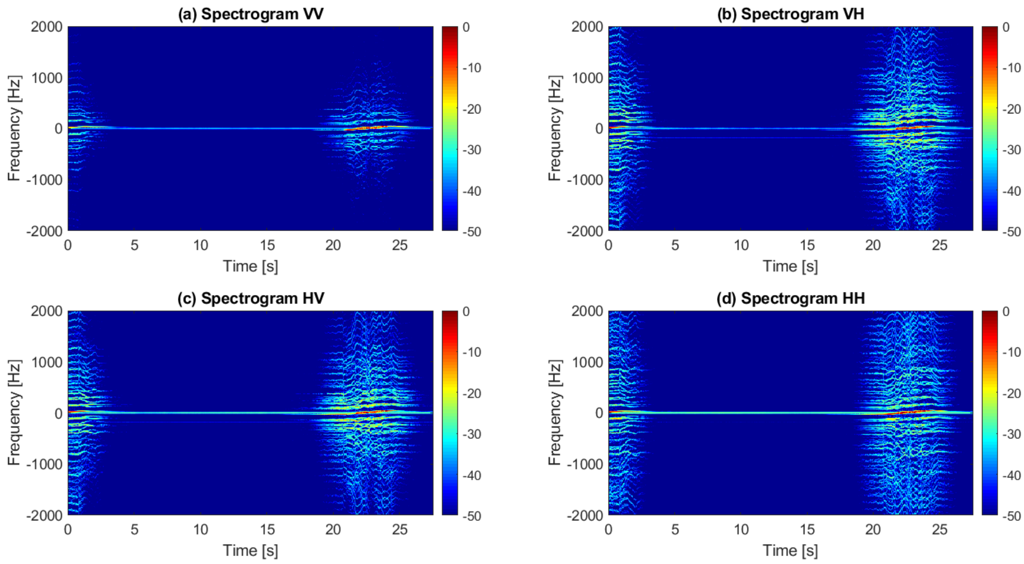


Figure B.7: PARSAX Data: Spectrogram Plot at VV, VH, HV, HH channels for Drone M200 Hexacopter Flying with 1kg payload

2. PARSAX Data: Spectrogram of M200 Quadcopter in rectangular waypoints with 1kg payload at all polarimetric channels

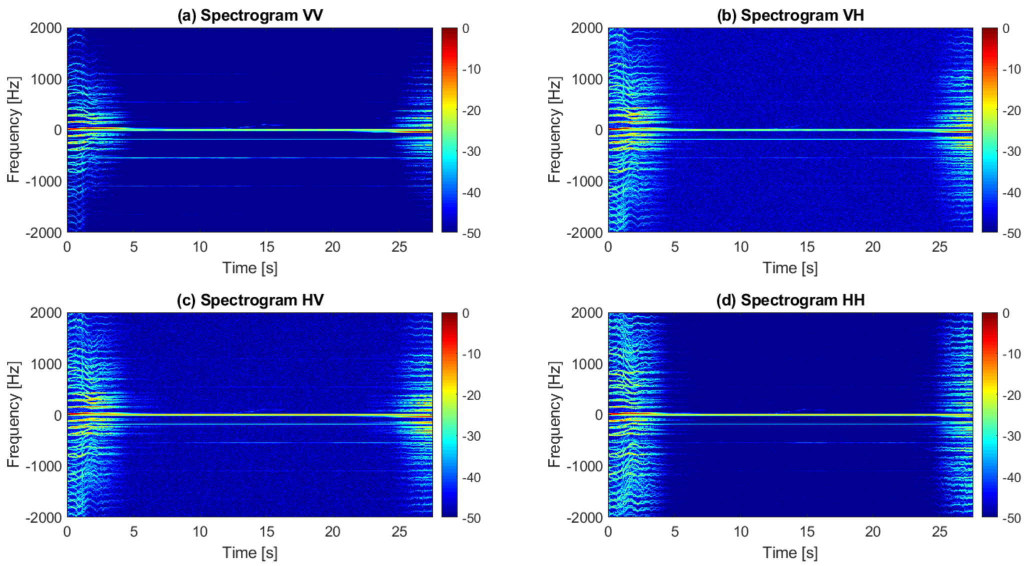


Figure B.8: PARSAX Data: Spectrogram Plot at VV, VH, HV, HH channels for Drone M200 Quadcopter in Waypoints with 1kg payload

3. PARSAX Data: Spectrogram of M600 Hexacopter in rectangular waypoints with 2.35kg payload at all polarimetric channels

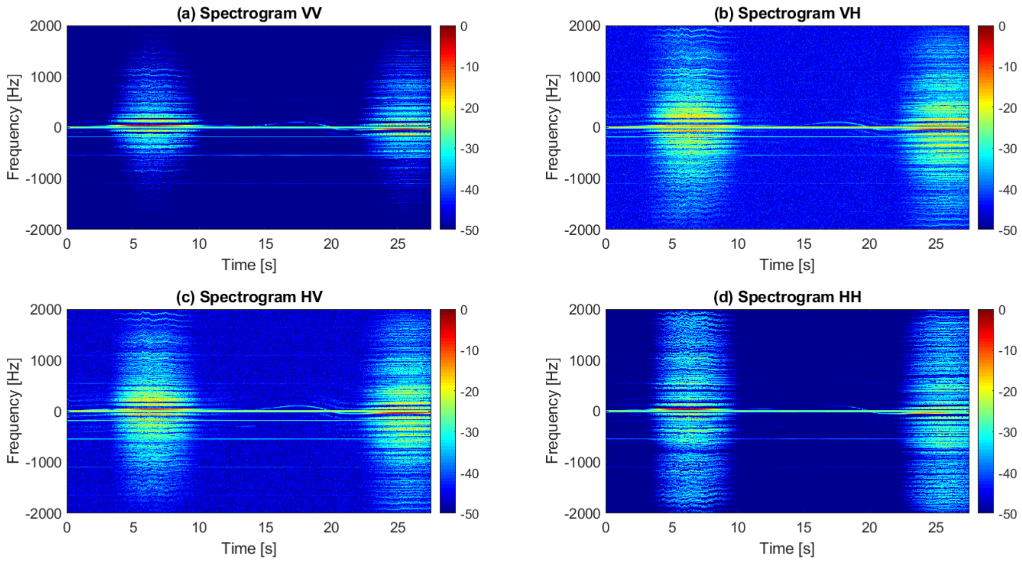


Figure B.9: PARSAX Data: Spectrogram Plot at VV, VH, HV, HH channels for Drone M600 Hexacopter in Waypoints with 2.35kg payload

# Bibliography


[1] *Clarity from above: Pwc global report on the commercial applications of drone technology.* [Online]. Available: https://www.skillsforaustralia.com/2016/06/10/test-post-14/.

[2] *Evolution of the drone threat: Top ten drone incidents.* [Online]. Available: https://www.robinradar.com/press/blog/evolution-of-the-drone-threat-top-ten-drone-incidents.

[3] *Uas by the numbers.* [Online]. Available: https://www.faa.gov/uas/resources/by_the_numbers.

[4] J.-P. Yaacoub, H. Noura, O. Salman, and A. Chehab, "Security analysis of drones systems: Attacks, limitations, and recommendations," *Internet of Things*, vol. 11, p. 100 218, 2020. DOI: 10.1016/j.iot.2020.100218.

[5] J. Patel, F. Fioranelli, and D. Anderson, "Review of radar classification and rcs characterisation techniques for small uavs or drones," *IET Radar, Sonar Navigation*, vol. 12, Jun. 2018. DOI: 10.1049/iet-rsn.2018.0020.

[6] J. S. Patel, C. Al-Ameri, F. Fioranelli, and D. Anderson, "Multi-time frequency analysis and classification of a micro-drone carrying payloads using multistatic radar," *The Journal of Engineering*, vol. 2019, no. 20, pp. 7047–7051, 2019. DOI: 10.1049/joe.2019.0551.

[7] M. Jahangir and C. Baker, "Robust detection of micro-uas drones with l-band 3-d holographic radar," in *2016 Sensor Signal Processing for Defence (SSPD)*, 2016, pp. 1–5. DOI: 10.1109/SSPD.2016.7590610.

[8] B. Torvik, K. E. Olsen, and H. Griffiths, "Classification of birds and uavs based on radar polarimetry," *IEEE Geoscience and Remote Sensing Letters*, vol. 13, no. 9, pp. 1305–1309, 2016. DOI: 10.1109/LGRS.2016.2582538.

[9] A. Huizing, M. Heiligers, B. Dekker, J. de Wit, L. Cifola, and R. Harmanny, "Deep learning for classification of mini-uavs using micro-doppler spectrograms in cognitive radar," *IEEE Aerospace and Electronic Systems Magazine*, vol. 34, no. 11, pp. 46–56, 2019. DOI: 10.1109/MAES.2019.2933972.

[10] J. J. De Wit, D. Gusland, and R. P. Trommel, "Radar measurements for the assessment of features for drone characterization," in *2020 17th European Radar Conference (EuRAD)*, 2021, pp. 38–41. DOI: 10.1109/EuRAD48048.2021.00021.

[11] L. Pallotta, C. Clemente, A. Raddi, and G. Giunta, "A feature-based approach for loaded/unloaded drones classification exploiting micro-doppler signatures," in *2020 IEEE Radar Conference (RadarConf20)*, 2020, pp. 1–6. DOI: 10.1109/RadarConf2043947.2020.9266458.

[12] S. Rahman, D. A. Robertson, and M. A. Govoni, "Radar signatures of drones equipped with liquid spray payloads," in *2020 IEEE Radar Conference (RadarConf20)*, 2020, pp. 1–5. DOI: 10.1109/RadarConf2043947.2020.9266374.

[13] A. Coluccia, G. Parisi, and A. Fascista, "Detection and classification of multirotor drones in radar sensor networks: A review," *Sensors*, vol. 20, no. 15, 2020, ISSN: 1424-8220. DOI: 10.3390/s20154172. [Online]. Available: https://www.mdpi.com/1424-8220/20/15/4172.

[14] B. Taha and A. Shoufan, “Machine learning-based drone detection and classification: State-of-the-art in research,” *IEEE Access*, vol. 7, pp. 138 669–138 682, 2019. DOI: 10.1109/ACCESS.2019.2942944.

[15] A. Huang, P. Sévigny, B. Balaji, and S. Rajan, “Fundamental frequency estimation of herm lines of drones,” in *2020 IEEE International Radar Conference (RADAR)*, 2020, pp. 1013–1018. DOI: 10.1109/RADAR42522.2020.9114676.

[16] J. Markow and A. Balleri, “Examination of drone micro-doppler and jem/herm signatures,” in *2020 IEEE Radar Conference (RadarConf20)*, 2020, pp. 1–6. DOI: 10.1109/RadarConf2043947.2020.9266342.

[17] R. I. A. Harmanny, J. J. M. de Wit, and G. P. Cabic, “Radar micro-doppler feature extraction using the spectrogram and the cepstrogram,” in *2014 11th European Radar Conference*, 2014, pp. 165–168. DOI: 10.1109/EuRAD.2014.6991233.

[18] Y. Cai, O. Krasnov, and A. Yarovoy, “Radar recognition of multi-propeller drones using micro-doppler linear spectra,” in *2019 16th European Radar Conference (EuRAD)*, 2019, pp. 185–188.

[19] M. Ritchie, F. Fioranelli, H. Borrion, and H. Griffiths, “Multistatic micro-doppler radar feature extraction for classification of unloaded/loaded micro-drones,” *IET Radar, Sonar Navigation*, vol. 11, no. 1, pp. 116–124, 2017. DOI: 10.1049/iet-rsn.2016.0063.

[20] Y. Zhao, X. Zhang, and F. Fioranelli, “Initial results of radar-based classification of commercial drone carrying small payloads,” in *2019 International Radar Conference (RADAR)*, 2019, pp. 1–4. DOI: 10.1109/RADAR41533.2019.171305.

[21] B. Knoedler, R. Zemmari, and W. Koch, “On the detection of small uav using a gsm passive coherent location system,” in *2016 17th International Radar Symposium (IRS)*, 2016, pp. 1–4. DOI: 10.1109/IRS.2016.7497375.

[22] A. Chadwick, *IET Conference Proceedings*, -(1), Jan. 2017. [Online]. Available: https://digital-library.theiet.org/content/conferences/10.1049/cp.2017.0419.

[23] S. Rahman, D. A. Robertson, and M. A. Govoni, “Radar signatures of drones equipped with heavy payloads and dynamic payloads generating inertial forces,” *IEEE Access*, vol. 8, pp. 220 542–220 556, 2020. DOI: 10.1109/ACCESS.2020.3042798.

[24] M. A. Richards, J. A. Scheer, and W. A. Holm, *Principles of Modern Radar: Basic principles*, ser. Radar, Sonar and Navigation. Institution of Engineering and Technology, 2010. [Online]. Available: https://digital-library.theiet.org/content/books/ra/sbra021e.

[25] B. R. MAHAFZA, *Radar systems analysis and design using matlab*. CRC Press.

[26] Skolnik and M. Ivan., *Introduction to radar systems*, 1980. [Online]. Available: https://www.amazon.com/Introduction-Radar-Systems-Merrill-Skolnik/dp/0072881380.

[27] *Microwave frequency bands*. [Online]. Available: https://www.everythingrf.com/tech-resources/frequency-bands.

[28] *Parsax*. [Online]. Available: http://radar.ewi.tudelft.nl/Facilities/parsax.php.

[29] *Dji - official website*. [Online]. Available: https://www.dji.com/nl.

[30] V. C.Chen and H. Ling, *Time-Frequency Transform for Radar Imaging and Signal Analysis*. Artech House, 2002. [Online]. Available: www.artechhouse.com.

[31] B. Torvik, A. Knapskog, Ø. Lie-Svendsen, K. E. Olsen, and H. D. Griffiths, “Amplitude modulation on echoes from large birds,” in *2014 11th European Radar Conference*, 2014, pp. 177–180. DOI: 10.1109/EuRAD.2014.6991236.

[32] J. J. M. de Wit, R. I. A. Harmanny, and G. Prémel-Cabic, “Micro-doppler analysis of small uavs,” in *2012 9th European Radar Conference*, 2012, pp. 210–213.

[33] M. Ritchie, F. Fioranelli, and H. Borrion, “Micro uav crime prevention: Can we help princess leia?” In *Crime Prevention in the 21st Century: Insightful Approaches for Crime Prevention Initiatives*, B. LeClerc and E. U. Savona, Eds. Cham: Springer International Publishing, 2017, pp. 359–376, ISBN: 978-3-319-27793-6. DOI: 10.1007/978-3-319-27793-6_21. [Online]. Available: https://doi.org/10.1007/978-3-319-27793-6_21.

[34] F. Fioranelli, M. Ritchie, S. Z. Gürbüz, and H. Griffiths, “Feature diversity for optimized human micro-doppler classification using multistatic radar,” *IEEE Transactions on Aerospace and Electronic Systems*, vol. 53, no. 2, pp. 640–654, 2017. DOI: 10.1109/TAES.2017.2651678.

[35] J. J. M. de Wit, R. I. A. Harmanny, and P. Molchanov, “Radar micro-doppler feature extraction using the singular value decomposition,” in *2014 International Radar Conference*, 2014, pp. 1–6. DOI: 10.1109/RADAR.2014.7060268.

[36] F. Fioranelli, M. Ritchie, and H. Griffiths, “Performance analysis of centroid and svd features for personnel recognition using multistatic micro-doppler,” *IEEE Geoscience and Remote Sensing Letters*, vol. 13, no. 5, pp. 725–729, 2016. DOI: 10.1109/LGRS.2016.2539386.

[37] J. Lee and E. Pottier, *Polarimetric Radar Imaging: From Basics to Applications*. CRC Press, 2009. [Online]. Available: https://www.routledge.com/Polarimetric-Radar-Imaging-From-Basics-to-Applications/Lee-Pottier/p/book/9781420054972.

[38] *3.1. cross-validation: Evaluating estimator performance*. [Online]. Available: https://scikit-learn.org/stable/modules/cross_validation.html.

[39] M. U. Sheikh, F. Ghavimi, K. Ruttik, and R. Jantti, “Drone detection and classification using cellular network: A machine learning approach,” in *2019 IEEE 90th Vehicular Technology Conference (VTC2019-Fall)*, 2019, pp. 1–6. DOI: 10.1109/VTCFall.2019.8891229.

[40] S. Jeong, J. Bito, and M. M. Tentzeris, “Design of a novel wireless power system using machine learning techniques for drone applications,” in *2017 IEEE Wireless Power Transfer Conference (WPTC)*, 2017, pp. 1–4. DOI: 10.1109/WPT.2017.7953890.

[41] M. Z. Anwar, Z. Kaleem, and A. Jamalipour, “Machine learning inspired sound-based amateur drone detection for public safety applications,” *IEEE Transactions on Vehicular Technology*, vol. 68, no. 3, pp. 2526–2534, 2019. DOI: 10.1109/TVT.2019.2893615.

[42] D. S. Laboratory and Technology, *The dstl biscuit book*, Oct. 2020. [Online]. Available: https://www.gov.uk/government/publications/the-dstl-biscuit-book.

[43] H. Li, A. Shrestha, H. Heidari, J. Le Kernec, and F. Fioranelli, “Bi-lstm network for multimodal continuous human activity recognition and fall detection,” *IEEE Sensors Journal*, vol. 20, no. 3, pp. 1191–1201, 2020. DOI: 10.1109/JSEN.2019.2946095.

[44] D. Roggen, G. Tröster, and A. Bulling, “12 - signal processing technologies for activity-aware smart textiles,” in *Multidisciplinary Know-How for Smart-Textiles Developers*, ser. Woodhead Publishing Series in Textiles, T. Kirstein, Ed., Woodhead Publishing, pp. 329–365, ISBN: 978-0-85709-342-4. DOI: https://doi.org/10.1533/9780857093530.2.329. [Online]. Available: https://www.sciencedirect.com/science/article/pii/B9780857093424500122.

[45] S. Z. Gürbüz, B. Erol, and B. Tekeli, “Operational assessment and adaptive selection of micro-doppler features,” *IET Radar, Sonar and Navigation*, vol. 9, 1196–1204(8), 9 Dec. 2015, ISSN: 1751-8784. [Online]. Available: https://digital-library.theiet.org/content/journals/10.1049/iet-rsn.2015.0144.